

# Edge Fan Performance in Air-Cooled Condensers

by

**PJF Conradie**

*Thesis presented in partial fulfilment of the requirements for the degree Master of Science in Engineering at the University of Stellenbosch*



*Supervisor: **Mr SJ van der Spuy***

*Co-supervisor: **Prof TW von Backström***

Department of Mechanical and Mechatronic Engineering

March 2010

## DECLARATION

By submitting this thesis electronically, I declare that the entirety of the work contained therein is my own, original work, that I am the owner of the copyright thereof (unless to the extent explicitly otherwise stated) and that I have not previously in its entirety or in part submitted it for obtaining any qualification.

15 February 2010

.....

Signature

.....

Date

***The financial assistance of the South African National Energy Research Institute towards this research is hereby acknowledged. Opinions expressed and conclusions arrived at, are those of the author and are not necessarily to be attributed to SANERI.***

## **ABSTRACT**

Large air-cooled heat exchangers and condensers make use of fan arrays to provide cooling. The performance of the fan arrays are however negatively affected by distorted inlet conditions. Given the size of these fans, quantifying exactly what the detrimental effects are is practically impossible. This serves as motivation for developing a scaled multi-fan testing platform that is able to mimic the behaviour of a full-scale array but at a more measurable and manageable scale. This investigation was conducted in two parts. A Reynolds number investigation was conducted to determine what effect incorporating Reynolds number effects will have on the scaled fan performance.

Computational fluid dynamics (CFD) was used to determine where turbulent transition onset occurs on the full-scale fan blades and trip wires were then sized and positioned appropriately to recreate the same transition effect. From this initial investigation it was found that the trip wires have an all-round negative impact on fan performance but when compensated for by increasing the blade angle, the tripped fan static pressure rise performance is comparable with the non-tripped fan performance. This suggests that the Reynolds number effects may be ignored for this scaled fan testing investigation.

Scaled equivalents of the fans in cooling arrays were tested in a three row multi-fan array which, using symmetry, represents a typical bay in a full-scale installation. Various platform heights were simulated and the corresponding decrease in system performance was compared to a model formulated to predict how fan volumetric effectiveness decreases with platform height. The model deviated from the test data at very low platform heights. A replacement fan for the scaled equivalent fan was tested while installed as the edge fan of a multi-fan array, the fan worst affected by any inlet disturbance, and was found to perform similarly to the scaled equivalent fan for most platform heights but exceeded the scaled equivalent fan's performance for the lowest platform height and the most adverse conditions. This proves the effectiveness of the replacement fan as an edge fan.

## OPSOMMING

Groot lugverkoelde warmteruilers maak gebruik van waaier matrikse om verkoeling te voorsien. Die verrigting van die waaieropstelling word egter negatief beïnvloed deur versteurde inlaattoestande. Gegewe die grootte van hierdie waaiers is daar geen praktiese metode om die nadelige invloed van die versteurde inlaattoestande te kwantifiseer nie. Hierdie dien as motivering vir die ontwikkeling van 'n multi-waaier toetsplatform wat daartoe in staat is om die gedrag van die volskaal opstelling na te boots maar op 'n baie meer meetbare en hanteerbare skaal. Hierdie ondersoek was uitgevoer in twee dele. 'n Reynoldsgetal ondersoek was uitgevoer om te bepaal watter impak dit sal hê op die skaalwaaier verrigting indien die Reynolds getaleffekte ingesluit word in die toetswerk. Berekende vloedynamika (BVD) was gebruik om te bepaal waar turbulente oorgang voorkom op die volskaal waaierlemme en pooitjiedrade was geselekteer en geposisioneer hiervolgens om dieselfde oorgang te herskep. Vanuit hierdie aanvanklike ondersoek was dit gevind dat die pooitjiedrade 'n algehele afname in verrigting tot gevolg het, maar wanneer dit oorkom word deur die lemhoek op te stel, die gedrag en verrigting van die gepooitjiede waaier soortgelyk is aan die van die nie-gepooitjiede waaier. Hierdie gedrag stel voor dat die Reynoldsgetalle maar geïgnoreer kan word vir hierdie skaalwaaier toetswerk.

Gelykwaardige skaalwaaiers van die wat in bedryf is in volskaal opstellings was getoets in 'n drie ry multi-waaier opstelling wat, deur simmetrie, verteenwoordigend is van 'n tipiese straat in 'n volskaal opstelling. Verskeie platformhoogtes was gesimuleer en die ooreenstemmende afname in stelsel verrigting was vergelyk met 'n model wat geformuleer is juis om te voorspel hoe die volumetriese effektiwiteit afneem met platformhoogte. Die model wyk af van die toetsdata by baie lae platform hoogtes. 'n Vervangingswaaier vir die aanvanklike geskalleerde waaier was getoets as 'n randwaaier, die waaier wat die ergste benadeel word deur versteurde inlaattoetstande, in die multi-waaier opstelling. Die vervangingswaaier het soortgelyk aan die aanvanklike waaier verrig vir meeste platformhoogtes, maar oortref die aanvanklike waaier se werksverrigting by die laagste platformhoogte en mees ongunstige toestande. Hierdie bewys die vermoëns van die vervangingswaaier as 'n randwaaier.

## **ACKNOWLEDGEMENTS**

Firstly, Mr Johan van der Spuy and Prof Theo von Backström for the opportunity, their steady guidance and constant support. I can honestly say I have been privileged to have had you as my supervisors for the last two years.

To Mr Cobus Zietsman and Mr Ferdi Zietsman for being there to help tackle the unexpected and provide the insight that only comes with experience.

To Graham, Calvin, Anton, Juliun and Nathi – you are the gears and cogs that make Mechanical Department and the Mechanical Workshop tick.

To my office-mates, thank you for making the last two years a fun and growing experience, and providing the support and helping hands that make you my friends. The innumerable debates undertaken and worldly problems ‘solved’ during our office banter over the last two years are moments I will miss.

## TABLE OF CONTENTS

<b>DECLARATION</b> .....	<b>i</b>
<b>ABSTRACT</b> .....	<b>iii</b>
<b>OPSOMMING</b> .....	<b>iv</b>
<b>ACKNOWLEDGEMENTS</b> .....	<b>v</b>
<b>1 INTRODUCTION</b> .....	<b>1</b>
<b>2 LITERATURE STUDY</b> .....	<b>6</b>
<b>3 REYNOLDS NUMBER AND SURFACE ROUGHNESS INVESTIGATION</b> .....	<b>13</b>
3.1 INTRODUCTION AND OBJECTIVES.....	13
3.2 SETUP FOR NUMERICAL TRANSITION INVESTIGATION.....	14
3.3 NUMERICAL TRANSITION INVESTIGATION .....	19
3.4 NUMERICAL INDUCED TRANSITION EVALUATION .....	25
3.5 EXPERIMENTAL INDUCED TRANSITION EVALUATION .....	37
3.6 CONCLUSION.....	42
<b>4 EMPIRICAL FAN COMPARISON</b> .....	<b>46</b>
4.1 INTRODUCTION AND OBJECTIVES.....	46
4.2 EXPERIMENTAL SETUP.....	50
4.3 INDIVIDUAL SCALED FAN PERFORMANCE .....	57
4.4 FAN ARRAY PERFORMANCE.....	64
4.5 CONCLUSION.....	70
<b>5 CONCLUSION</b> .....	<b>75</b>
<b>6 REFERENCES</b> .....	<b>77</b>
<b>APPENDIX A: EQUIPMENT CALIBRATION</b> .....	<b>79</b>
A.1 CALIBRATION OF REFERENCE PROPELLER ANEMOMETER.....	79
A.1.1 Calibration Setup .....	80
A.1.2 Pressure Transducer Calibration .....	84
A.1.3 Test Data.....	86
A.1.4 Conclusion .....	87
A.2 CALIBRATION OF TUNNEL ANEMOMETERS.....	88
A.2.1 Calibration Setup .....	88
A.2.2 Pressure Transducer Calibration .....	90
A.2.3 Test Data.....	91
A.2.4 Conclusion .....	95
A.3 TORQUE TRANSDUCER CALIBRATION.....	96

A.3.1	Calibration Setup .....	96
A.3.2	Test Data.....	97
A.3.3	Conclusion .....	99
<b>APPENDIX B: FAN GEOMETRY AND PERFORMANCE DATA.....</b>		<b>100</b>
B.1	N FAN .....	100
B.1.1	Fan Geometry .....	100
B.1.2	Fan Performance .....	103
B.2	B2 FAN.....	105
B.2.1	Fan Geometry .....	105
B.2.2	Fan Performance .....	108
<b>APPENDIX C: SAMPLE CALCULATION FROM TEST DATA.....</b>		<b>110</b>



## LIST OF FIGURES

FIGURE 1.1 AIR-COOLED CONDENSER (ACC) AT THE LARGEST DRY-COOL POWER STATION IN THE WORLD .....	1
FIGURE 1.2 TYPICAL A-FRAME ACC .....	2
FIGURE 1.3 FAN ARRAY PLATFORM OF THE ACC .....	3
FIGURE 1.4 VIEW FROM BELOW ACC FAN ARRAY SHOWING ROWS OF AXIAL COOLING FANS .....	4
FIGURE 2.1 VELOCITY TRIANGLES FOR FLOW AROUND AN AEROFOIL .....	6
FIGURE 2.2 VISSER WITH HIS FAN ARRAY SETUP (VISSER, 1990) .....	7
FIGURE 3.1 GENERIC STARTING MESH FOR NUMERICAL REYNOLDS NUMBER INVESTIGATION .....	16
FIGURE 3.2 REFINED MESH FOR NUMERICAL REYNOLDS NUMBER INVESTIGATION .....	17
FIGURE 3.3 VORTICES AT TRAILING EDGE ON FULL-SCALE TIP SOLUTION .....	20
FIGURE 3.4 FINE AND ORIGINAL MESH $C_f$ COMPARISON FOR FULL-SCALE TIP SOLUTIONS .....	21
FIGURE 3.5 STATIC PRESSURE DISTRIBUTION FOR SCALED HUB SOLUTION .....	21
FIGURE 3.6 VELOCITY MAGNITUDE DISTRIBUTION FOR SCALED HUB SOLUTION .....	22
FIGURE 3.7 STATIC PRESSURE DISTRIBUTION FOR FULL-SCALE TIP SOLUTION .....	23
FIGURE 3.8 VELOCITY MAGNITUDE DISTRIBUTION FOR FULL-SCALE TIP SOLUTION.....	23
FIGURE 3.9 $C_f$ COMPARISON FOR HUB SOLUTIONS OF SCALED AND FULL-SCALE PROBLEMS .....	24
FIGURE 3.10 $C_f$ COMPARISON FOR TIP SOLUTIONS OF SCALED AND FULL-SCALE PROBLEMS .....	25
FIGURE 3.11 FLAT PLATE WITH TRIP WIRE (WHITE, 2006) .....	25
FIGURE 3.12 DECREASE IN TRANSITION POSITION AS $k/\Delta^*$ (WHITE, 2006) .....	26
FIGURE 3.13 TWO-DIMENSIONAL MESH OF HUB SIMULATION FEATURING 1.219 MM TRIP WIRES AT TRANSITION POSITION .....	27
FIGURE 3.14 $C_f$ OF SCALED HUB SOLUTION FOR INDUCED TRANSITION (AT TRIP WIRE 1.219 MM TRIP WIRE) .....	28
FIGURE 3.15 VELOCITY MAGNITUDE DISTRIBUTION OF SCALED HUB FEATURING TRIP WIRE (1.219 MM TRIP WIRE) .....	29
FIGURE 3.16 TWO-DIMENSIONAL MESH OF HUB SIMULATION FEATURING 0.315 MM TRIP WIRES AT LEADING EDGE .....	30
FIGURE 3.17 COMPARISON OF VELOCITY MAGNITUDE DISTRIBUTION BETWEEN FINE SOLUTION (TOP) AND 0.315 MM TRIP WIRE SOLUTION (BOTTOM) AT HUB .....	32
FIGURE 3.18 $C_f$ COMPARISON FOR HUB SOLUTION OF SCALED INDUCED TRANSITION (DOWNSTREAM OF TRIP WIRE, 0.315 MM TRIP WIRE) AND FULL-SCALE HUB SOLUTION .....	33
FIGURE 3.19 TWO-DIMENSIONAL MESH OF TIP SIMULATION FEATURING 0.315 MM TRIP WIRES AT DESIRED TRANSITION LOCATIONS	34
FIGURE 3.20 COMPARISON OF VELOCITY MAGNITUDE DISTRIBUTION BETWEEN FINE SOLUTION (TOP) AND 0.315 MM TRIP WIRE SOLUTION (BOTTOM) AT TIP .....	35
FIGURE 3.21 $C_f$ COMPARISON FOR TIP SOLUTIONS OF SCALED INDUCED TRANSITION (AT TRIP WIRE, 0.315 MM TRIP WIRE) AND FULL-SCALE PROBLEMS .....	36
FIGURE 3.22 $C_f$ COMPARISON FOR HUB SOLUTIONS OF SCALED FAN FOR 0.315 MM TRIP WIRE FOR NORMAL OPERATION AND FOR 15 M/S OPERATION .....	37
FIGURE 3.23 TRIP WIRE (0.3 MM FISHING LINE) 'PAINTED' TO BLADE SURFACE .....	38
FIGURE 3.24 EFFECT OF TWO-DIMENSIONAL ROUGHNESS ELEMENT (0.3 MM TRIP WIRE) ON FAN STATIC PRESSURE RISE (FAN 1, IDENTICAL BLADE ANGLE).....	39

FIGURE 3.25 EFFECT OF TWO-DIMENSIONAL ROUGHNESS ELEMENT (0.3 MM TRIP WIRE) ON FAN STATIC PRESSURE RISE (FAN 3, INCREASED BLADE ANGLE).....	41
FIGURE 3.26 EFFECT OF TWO-DIMENSIONAL ROUGHNESS ELEMENT (0.3 MM TRIP WIRE) ON FAN POWER (FAN 3, INCREASED BLADE ANGLE) .....	41
FIGURE 3.27 VISUALISATION OF DELAYED BOUNDARY LAYER TRANSITION.....	43
FIGURE 3.28 INFLUENCE OF TRIP WIRE ON FLOW PATH OVER FAN BLADE .....	45
FIGURE 4.1 SCALE N FAN INSTALLED IN TEST TUNNEL.....	47
FIGURE 4.2 SCALE B FAN INSTALLED IN EDGE TEST TUNNEL (FAN 3) .....	48
FIGURE 4.3 TYPICAL LARGE-SCALE FAN ARRAY ILLUSTRATING DIFFERENT EXPERIMENTAL REPRESENTATIONS .....	49
FIGURE 4.4 SYSTEM VOLUMETRIC EFFECTIVENESS FOR ACHES HAVING 1, 2, 4, 8 AND 12 FAN ROWS (SALTA & KRÖGER, 1995)....	50
FIGURE 4.5 SCHEMATIC OF EDGE AND INNER INDIVIDUAL TUNNELS (TOP → EDGE FAN, BOTTOM → INNER FANS).....	52
FIGURE 4.6 OVERLAPPING DISC THROTTLE .....	52
FIGURE 4.7 PERFORATED PLATE THROTTLE .....	53
FIGURE 4.8 TOP VIEW SCHEMATIC OF FAN ARRAY.....	54
FIGURE 4.9 FAN ARRAY IN N-N-N CONFIGURATION .....	54
FIGURE 4.10 FAN ARRAY IN N-N-B CONFIGURATION.....	55
FIGURE 4.11 N FAN BLADE ANGLE JIG.....	56
FIGURE 4.12 B FAN BLADE ANGLE JIG .....	56
FIGURE 4.13 SIMPLE SCHEMATIC OF N FAN (LEFT) AND B FAN (RIGHT) .....	57
FIGURE 4.14 N FAN STATIC PRESSURE RISE CURVE (FAN 1).....	59
FIGURE 4.15 N FAN STATIC PRESSURE RISE CURVE (FAN 2).....	60
FIGURE 4.16 N FAN STATIC PRESSURE RISE CURVE (FAN 3).....	60
FIGURE 4.17 N FAN POWER CURVE (FAN 3).....	61
FIGURE 4.18 N FAN STATIC EFFICIENCY CURVE (FAN 3) .....	61
FIGURE 4.19 B FAN STATIC PRESSURE RISE CURVE (FAN 3).....	62
FIGURE 4.20 B FAN POWER CURVE (FAN 3) .....	62
FIGURE 4.21 B FAN STATIC EFFICIENCY CURVE (FAN 3).....	63
FIGURE 4.22 PLUG CONFIGURATION IN PERFORATED PLATE FOR ARRAY TESTING .....	65
FIGURE 4.23 CORNER CHAMFER FOR 'LOWEST' PLATFORM HEIGHT SETTING .....	66
FIGURE 4.24 SYSTEM VOLUMETRIC EFFECTIVENESS FOR N-N-N CONFIGURATION.....	66
FIGURE 4.25 SYSTEM VOLUMETRIC EFFECTIVENESS FOR N-N-B CONFIGURATION .....	67
FIGURE 4.26 COMPARATIVE SYSTEM VOLUMETRIC EFFECTIVENESS FOR N-N-N AND N-N-B CONFIGURATION.....	68
FIGURE 4.27 COMPARATIVE INDIVIDUAL FAN VOLUMETRIC EFFECTIVENESS FOR N FAN AND B FAN AS EDGE FAN .....	69
FIGURE 4.28 COMPARATIVE FAN POWER CURVES FOR N FAN AND B FAN AS EDGE FANS .....	69
FIGURE A.1 PROPELLER ANEMOMETER IN CASING-BELLMOUTH ASSEMBLY .....	79
FIGURE A.2 SCHEMATIC OF TEST WINDTUNNEL (KRÖGER, 1998).....	82
FIGURE A.3 PRESSURE TRANSDUCER CALIBRATION SETUP .....	85
FIGURE A.4 MEASURED DATA POINT SETS WITH LINEAR CURVE FIT .....	87
FIGURE A.5 DUAL-FAN UNIT WITH FLOW CONTROL THROTTLE .....	89
FIGURE A.6 REFERENCE ANEMOMETER CLAMPED TO TUNNEL OUTLET .....	92

FIGURE A.7 TUNNEL ANEMOMETER CALIBRATION CURVES FOR TUNNEL 1.....	93
FIGURE A.8 TUNNEL ANEMOMETER CALIBRATION CURVES FOR TUNNEL 2.....	94
FIGURE A.9 TUNNEL ANEMOMETER CALIBRATION CURVES FOR TUNNEL 3.....	94
FIGURE A.10 POSITIONING OF TORQUE TRANSDUCER CALIBRATION JIG.....	98
FIGURE A.11 TORQUE TRANSDUCER CALIBRATION CURVE.....	99
FIGURE B.1 MEASURED CROSS-SECTION SCATTER OF 9415 MM N FAN.....	101
FIGURE B.2 MEASURED BLADE ANGLE AS FUNCTION OF RADIUS.....	102
FIGURE B.3 MEASURED BLADE THICKNESS AS FUNCTION OF RADIUS AND CHORD LENGTH.....	102
FIGURE B.4 N FAN STATIC PRESSURE RISE CURVE.....	103
FIGURE B.5 N FAN STATIC EFFICIENCY CURVE.....	104
FIGURE B.6 SECTION PROFILE FOR NASA GA(W)-2 AIRFOIL (MCGHEE ET AL., 1977).....	106
FIGURE B.7 BLADE ANGLE, $\alpha$ , AS A FUNCTION OF $R/R_{TIP}$ .....	107
FIGURE B.8 CHORD LENGTH AS FUNCTION OF $R/R_{TIP}$ .....	107
FIGURE B.9 B2 FAN STATIC PRESSURE RISE CURVE.....	108
FIGURE B.10 B2 FAN SHAFT POWER CURVE.....	109
FIGURE B.11 B2 FAN STATIC EFFICIENCY CURVE.....	109

## LIST OF TABLES

TABLE 3.1 INLET PARAMETERS FOR REYNOLDS NUMBER NUMERICAL INVESTIGATION .....	15
TABLE 3.2 ATMOSPHERIC CONDITIONS FOR NUMERICAL SIMULATIONS .....	18
TABLE 3.3 DRAG FORCE COMPARISON FOR GRID INDEPENDENCE CONFIRMATION .....	19
TABLE 3.4 TRANSITION WIRE POSITION FOR SCALED FAN .....	27
TABLE 4.1 EQUIPMENT AND INSTRUMENTATION .....	51
TABLE A.1 ANEMOMETER CALIBRATION CURVES .....	95

## NOMENCLATURE

Symbol	Units	Description
A	$m^2$	cross-section area
A, B, C		test run/data set
C	$\frac{m}{s}$	absolute velocity
$C_D$		drag coefficient
$C_f$		skin friction coefficient, $\frac{\tau}{0.5\rho U^2}$
$C_L$		lift coefficient
D	m	diameter
F	N	force
g	$\frac{m}{s^2}$	acceleration due to gravity
i	deg	Incidence angle
k	m	trip wire thickness
$\ell$	m	turbulence length
L	m	characteristic length
$\dot{m}$	$\frac{kg}{s}$	mass flow rate
n		number of elements/objects/units
N	$\frac{r}{min}$	rotational speed
p	Pa	static pressure
P	W	power, shaft power
r	m	radius
Re		Reynolds number
T	°C, K	temperature
T	Nm	torque
T	%	freestream turbulence
U	$\frac{m}{s}$	freestream velocity
V	$\frac{m}{s}$	average velocity, freestream velocity
$\dot{V}$	$\frac{m^3}{s}$	volume flow rate

W		Relative flow velocity vector
x	m	position from datum, position along surface
X		non-dimensionalized system parameter
Ø	m	diameter

<b>Greek Symbol</b>	<b>Units</b>	<b>Description</b>
α	deg	angle of attack
β	deg	relative flow velocity angle
δ	m	boundary layer thickness
δ*	m	displacement thickness
ξ		conventional loss coefficient
η	%	efficiency
μ	$\frac{\text{N}}{\text{m}^2\text{s}}$	dynamic viscosity
ν	$\frac{\text{m}}{\text{s}}$	kinematic viscosity
ω	$\frac{\text{rad}}{\text{s}}$	angular velocity
ρ	$\frac{\text{kg}}{\text{m}^3}$	density
τ	Pa	shear stress
Λ		friction loss coefficient for one diameter length of pipe

<b>Subscripts &amp; Superscripts</b>	<b>Description</b>
a	axial
ave	average
id	ideal
1, 2, 3	tunnel positions
2	blade exit velocity
x	in x-direction
x-y	airway length from plane x to plane y
tr,T	position of transition
k	position of trip element
F	fan
i	increment

## 1 INTRODUCTION

Large diameter axial fans are used in air-cooled heat exchanger (ACHE) or condenser (ACC) installations. Besides well-known applications involving the air-conditioning and automotive industry, large air-cooled heat exchangers and air-cooled condensers are also used as the heat discharging system in petrochemical and dry-cooled power stations where the availability of cooling water is limited or very expensive. Dry-cooled power stations offer a substantial benefit in water-saving over more conventional wet-cooled power stations where up to 2.5 l/kWh of water is lost due to evaporation (Kröger, 1998). South Africa is known for its use and expertise in the field of dry-cooling power stations and the world's largest dry-cooled power station (6 x 665 MWe) is currently located at Lepalale in the Limpopo province, South Africa. This particular power station operates 288, 9.1 m diameter vertically axis orientated axial fans, each driven by a 270 kW electric motor (Venter, 1990). The condenser array for the world's largest dry-cool power station can be seen in Figure 1.1.



**Figure 1.1** Air-cooled condenser (ACC) at the largest dry-cool power station in the world

Multiple axial flow fan installations, as described above, are subjected to adverse air inlet flow conditions due to the variable influence of wind direction and strength, the interaction between individual fans and the effects of nearby structures. Axial flow fans are designed and tested to conform to a flow field with a uniform axial flow distribution and the losses associated with adverse inlet flow conditions are not accounted for. No reputable studies have thus far considered the design and testing of fans for distorted inlet conditions. A schematic of a typical A-frame air-cooled condenser can be seen in Figure 1.2.

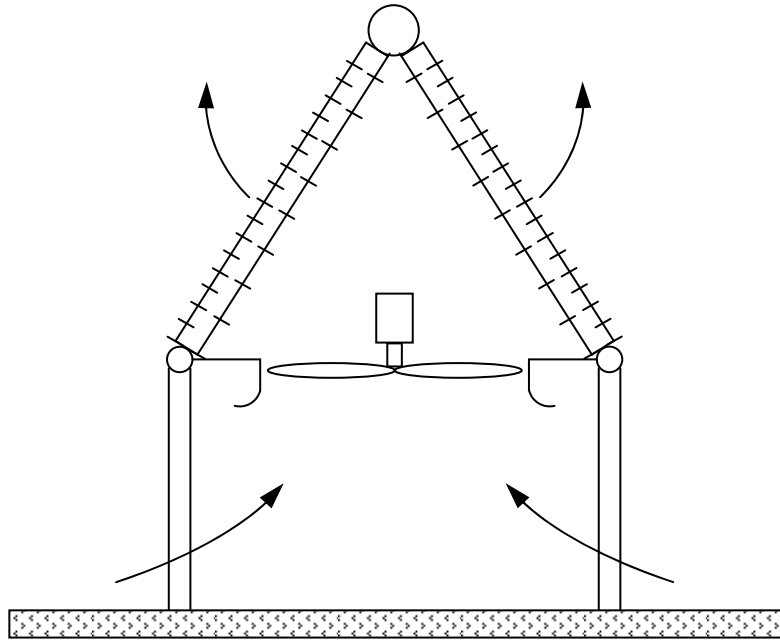


**Figure 1.2** Typical A-frame ACC

What this investigation aims to do is to provide the basis for a testing platform that will allow researchers and designers to evaluate existing and new fan designs with specific emphasis on performance in ACC's. The sheer size of the fans installed in ACC's does not allow engineers and technicians to quickly and accurately measure how the distorted inlet conditions these ACC's experience, affect the fan performance. The only performance measure available is the effectiveness of the ACC at condensing the steam (measured as a backpressure to the turbine) and although this certainly indicates that the system is not operating optimally, it does not provide the necessary information to determine exactly where and how the system is suffering. Fan stall and mechanical failure, both very obvious in full-scale ACC fan arrays, have indicated that the edge fans are most affected by these distorted inlet conditions. By



developing a scaled multi-fan testing platform, inlet disturbances can be recreated and accurately measured. The availability of such a testing platform will allow fans to be designed to operate better under these adverse conditions and hopefully later lead to improving the resistance of the ACC to distorted inlet conditions. The fan array platform of the world's largest air-cooled power station can be seen in Figure 1.3 and illustrates the sheer size of the ACC as well as one of the causes of distorted inlet conditions: nearby structures.



**Figure 1.3** Fan array platform of the ACC

A scaled testing platform, although easy to manage and measure, does provide some of its own challenges. By scaling fans down to a fraction of the original size, the Reynolds number is reduced. This means that the scaled fans do not operate under the same turbulence conditions as the full-scale fans. How to address the issue has been, and continues to be, a controversial topic. This investigation will evaluate the effect that recreating the full-scale turbulent boundary layer conditions on the scaled model fans will have on overall fan performance by using geometrically accurate scaled fans ( $N$  fans) and inducing boundary layer transition with the use of two-dimensional roughness elements. This evaluation is not only

good engineering practise, but will hopefully answer the question of how great an influence Reynolds numbers have on scaled fan (limited to the scale at which the evaluation will be done) performance.

As part of developing and verifying the testing platform, scaled system performance will be compared to existing prediction models that were formulated to predict how the system volumetric effectiveness (current volume flow versus ideal volume flow) is influenced by different fan array platform heights. By varying the platform height, the inlet area is decreased and the fans are not only slightly throttled, the velocity of the incoming flow is increased. This is one way simulate the effect of high wind speeds on a full-scale installation.



**Figure 1.4** View from below ACC fan array showing rows of axial cooling fans

A new fan design was proposed by Bruneau (1994) that should perform better under adverse inlet conditions but no verification testing has been conducted to date. Again, as part of evaluating the scaled testing platform, the fan proposed by Bruneau will be tested as the edge fan in a multi-fan array to determine the feasibility of this new design as a possible

replacement for the existing fans. Should the proposed new fan by Bruneau prove itself to be better under severe conditions, it might lead to more stable and resilient ACC performance. The view from below the ACC platform, as seen in Figure 1.4, shows the cooling fan array with the edge fans on the right-hand side.

Apart from increased ACC stability, the knowledge gained from developing this scaled multi-fan testing platform could lead to better fan and ACC performance, greater system reliability, reduced fan and drive (motor and gearbox) maintenance costs and better fan specifications for new ACC and ACHE installations.

## 2 LITERATURE STUDY

As per turbomachinery theory, the flow coming onto and flowing off an aerofoil (of a fan in this case) can be described by the relative relation between the rotational speed of the fan and the volume flow through the fan (assuming no inlet guide vanes). This relation is illustrated in Figure 2.1 with the use of velocity triangles. In Figure 2.1, the rotational velocity,  $U$ , is a function of the blade radius and angular velocity, also known as tangential velocity or blade speed, and is defined by  $r \cdot \omega$ . The axial flow is represented by  $C_a$ , and assuming a constant flow area from inlet to outlet and no radial flow through the rotor, this value remains unchanged. The resulting inlet velocity relative to the blade profile is given as  $W_1$  with the relative inlet flow angle (in the absence of an inlet guide vane, this angle is also the absolute flow angle) given as  $\beta_1$ . Likewise, the outlet relative flow velocity and angle is given as  $W_2$  and  $\beta_2$  respectively. Combining the relative outlet flow vector and the motion of the rotating blade, the absolute velocity vector of the flow leaving the blade is given by  $C_2$ . The blade (profile) setting angle,  $\gamma$ , is given as the angle between the plane of rotation and the profile chord line, but this definition may vary depending on profile/blade design or manufacturer. The incidence angle (as defined by Sayers, 1990),  $i$ , is the difference between the angle of the relative incoming flow and the blade setting angle. The angle of attack for fan blades is defined as the angle between the chord line and the average velocity vector of the incoming and outgoing flows,  $W_\infty$  (not shown). Large values for angle of attack will lead to blade stall.

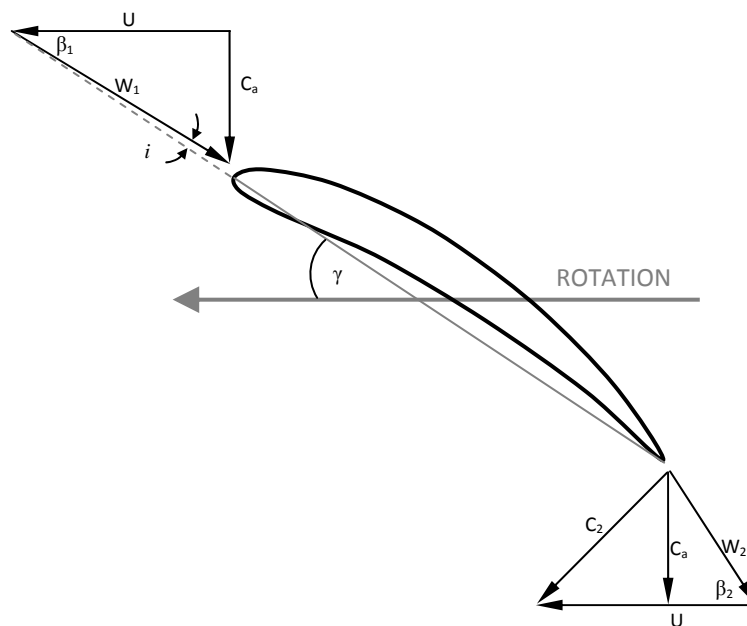
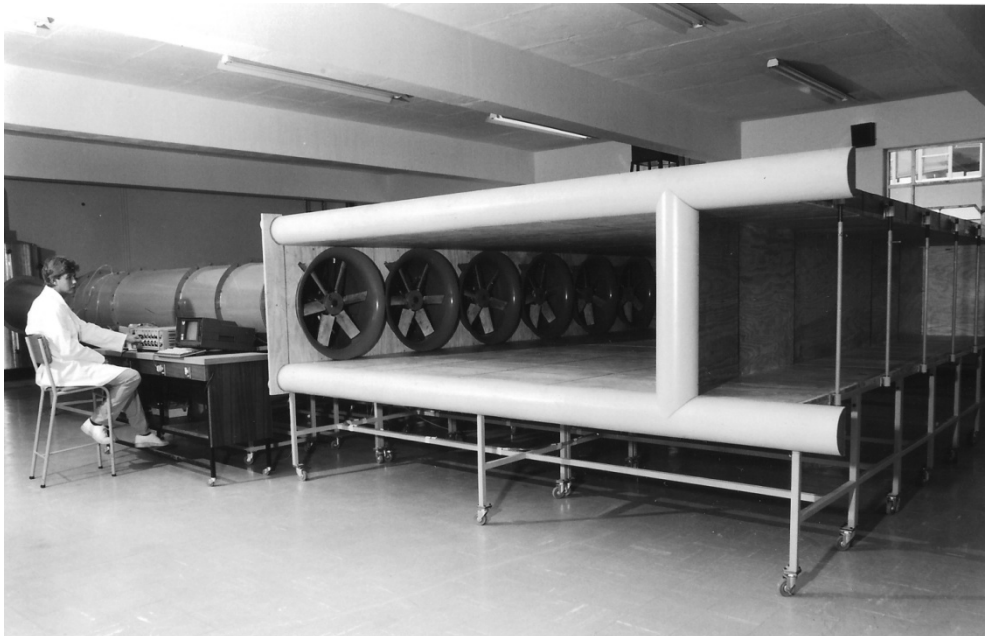


Figure 2.1 Velocity triangles for flow around an aerofoil

In 1990, Visser investigated the effects of distorted inlet flow patterns on axial flow fans in an array and illustrated the susceptibility of the edge fans to the effects of distorted inlet conditions. Visser experimented on scale models with geometric alterations like guide vanes and rounded inlets to try and improve the performance of the edge fans. His findings on the scale model translated well into real-world enhancements when minor improvements were tested on larger scale fans in fan assemblies. He also observed that the prevailing wind conditions can have a dire impact on the cooling tower performance. His scale model approach consisted of a single row of six 630 mm axial flow fans sealed about the bellmouth and drawing air through an enclosed inlet 'box'. This setup allowed Visser to recreate the flow conditions the edge fan would experience and by adjusting the position of the side of the 'box' he could also test at different 'elevations'. A similar scale model approach will be used for testing in this thesis.



**Figure 2.2** Visser with his fan array setup (Visser, 1990)

Venter (1990) investigated the governing mechanisms present when components that have distorting effects on the flow, are installed near an axial flow fan. Emphasis was placed on identifying different parameters that have flow enhancing or reducing effects. These parameters included geometrical aspects of the fan as well as the close proximity components. Venter compared his work to existing literature and, using non-dimensional scaling techniques, was also able to compare his scaled model data (1.542 m diameter fan) to data from a full size

fan (9.216 m diameter fan). His findings concluded that the most significant flow enhancing effects are obtained when the tip clearance of the fan is reduced and a solid disc is installed on the downstream side of the rotor. He was also able to conclude that the flow reduction effects can be minimized by either changing the shape or form of flow resisting components (walkways, supports, safety grids, heat exchangers, etc), or by moving the relative position of these components or by a combination of the two. For the specific design of fan, Venter identified that the two main causes for loss in efficiency are reverse flows around the hub and the fan's inability to cope with distorted inlet flows.

The work of Venter (1990) served as the main motivation for the study of Bruneau (1994) into the design of a single rotor axial flow fan specifically for cooling tower application. Bruneau not only took into consideration the potential gains Venter identified from decreasing the tip clearance, he also considered designs to minimize the loss in efficiency due to the regions of reversed flow at the hub. Since Bruneau was designing for cooling applications such as condenser units, which consist of parallel arrays of fans, one of his main concerns was the distorted inlet conditions a fan at or near the edge of a fan array might experience. These distortion effects are exaggerated by naturally occurring winds and nearby buildings. Time constraints prevented Bruneau from conducting tests while inducing distorted inlet flows, but during his design process he diligently included factors that might improve distortion tolerance. Bruneau used the well-known Clark-Y aerofoil profile as basis for his one design, and the high lift more modern NASA GA(W)-2 (McGhee et al., 1977) aerofoil as basis for his second design. Both of Bruneau's experimental designs, B1 and B2, showed good gains over the reference V-fan in general performance, and between 5% and 8% improvements in efficiency at the design point.

Salta & Kröger (1995) investigated the effects of inlet flow distortions on fan performance for fans located in air-cooled heat exchangers (ACHE) and developed a correlation that is capable of predicting the fan performance of single fans in the array based on their position and the array's operating conditions. Assuming that no flow crosses the bays and that the flow is symmetric about the middle fan, they used up to six 630 mm scaled fan rows to simulate up to 12 actual fan rows. The main focus of the investigation was to determine the performance impact distorted inlet flow will have on the edge fan (also referred to as periphery fan). The first part of the investigation evaluated the impact that increasing the number of fan rows has

on the edge fan. They saw that increasing the fan rows from four (two tested, four simulated) to 12 rows (six tested, 12 simulated) can decrease the edge fan's volumetric effectiveness by up to 58%, and also that the performance of the edge fan can be up to 56% lower relative to its adjacent fan. Through all this, the effect of ground height,  $H_i$ , was also varied. From this, Salta & Kröger formulated a general correlation that predicts the system volumetric effectiveness that takes into consideration not only the ground height but also the fan diameter and the number of fans. Very good agreement with the experimental data was achieved.

Part of this investigation is to determine whether the correlation by Salta & Kröger is still valid for other fan types than was used to collect their empirical data.

S.J. van der Spuy (1997) designed two different series of axial flow fans in cooperation with Howden Air Industries. The first series was a general purpose fan and the second was designed as part of a low-noise fan series. Although not purposely designed for such criteria, Van der Spuy's general purpose fan exhibited characteristics that are, as identified by Stinnes (1998), advantageous for cooling tower applications. Both his general purpose and low-noise fans showed improved performance over the respective reference fans. Although his research does not relate directly to fan arrays, cooling tower performance or distorted inlet conditions, the design methodology followed by Van der Spuy serves as guidance for any design work done during this thesis.

An investigation into the effect of cross-flow inlet conditions on fan performance was conducted by Stinnes (1998) and followed on the testing done by Bruneau. Experimenting in accordance with British testing standards, BS 848 (1980) and BS 1042 (1981 and 1984), Stinnes used pipe-sections to induce cross-flow inlet conditions on the fan with the cross-flow velocity-to-axial velocity ratio varying from 0.125 (7.1°) to 1 (45°). Stinnes' findings showed an 8% reduction in fan performance (fan static pressure and efficiency) when the cross-flow ratio was 1. From his work, it is possible to attribute a portion of the total fan performance reduction seen on large fan arrays to the cross-flow component of the air flowing into the fan. However, given his use of pipe-sections to induce cross-flow, all other inlet effects could not be investigated and quantified. It does however give due cause to suspect that the largest factor in reduced fan performance in large fan arrays may be attributed to effects in and around the inlet bellmouth since edge fans in these arrays can experience performance (fan static

pressure) drops of more than 30% (from design) in severe conditions. It is important to note that cross-flow inlet conditions and distorted inlet conditions are not related directly but both contribute to non-optimal performance of fans in large-scale fan arrays. The distinction between the two effects is further described in Hotchkiss et al. (2006).

Meyer and Kröger (2001) performed a numerical investigation into the flow field in the vicinity of an axial flow fan. They opted for an actuator disc model and obtained the actuator disc forces using blade element theory. The focus of the investigation was to develop and evaluate a numerical model to simulate the effect of an axial flow fan on the velocity field in the vicinity of the fan blades. They made use of the commercial computational fluid dynamics (CFD) code Flo<sup>++</sup>. The axial flow fan used for the investigation was the B fan (Bruneau, 1994)(Stinnes, 1998) and provided Meyer and Kröger with sufficient empirical data to compare their own evaluation with. All testing (for evaluation) was performed to BS848 standards on a Type A installation. Because their numerical model varied from the Type A test setup, verification tests were also done which compared the fan performance (all aspects) when the fan features a free or annular outlet. Their findings agreed with that of Stinnes (1998) in that the outlet configuration has essentially no impact on the performance of the fan. The final evaluation of the numerical results compared well (high flow rates differ by about 16% but the majority of the flow range is within 5% bounds) with the experimented data and proved the accuracy of the model and its ability to predict the axial flow fan performance characteristics over a large range of flow rates and blade settings.

Meyer and Kröger (2004) performed a numerical (CFD) investigation into the errors associated with the scaling of axial flow fan characteristics. They addressed the effects of Reynolds number and surface roughness on the accuracy of dimensionless scaling models and compared these analytical methods to numerical simulations using their earlier (2001) computational grid as a basis. The grid was subsequently improved through grid refinement in areas that will either experience large variable gradients or require a finer mesh for increased functionality (the actuator disc for example). The investigation was performed using the 1542 mm B Fan (Bruneau, 1994) at stagger angles of 61° and 51° (or 29° and 39° as measured in this thesis) and a rotational speed of 720 rpm, and then scaling it to 9000 mm and a rotational speed of 128.5 rpm. The rotational speed for the up scaled fan was based on the tip speed limit of 60 m/s which was imposed to minimize excessive sound power level generation in real world



application. They found that the fan static pressure and fan power consumption was underestimated by 3% and 4% respectively for the 51° scenario when the fan law scaling was compared to the numerical simulation, while the fan static efficiency was almost identical. The 61° scenario however showed very good correlation (~1%) for all aspects except at low flow rates where the fan law power consumption was about 5% less than the numerical solution. They concluded that the Reynolds number only affects the scaling if the angle of attack,  $\alpha$ , exceeds 2.5° along the majority of the blade radius. Increasing the surface roughness as described by McGhee et al (1977), Meyer and Kröger identified the effects of increased surface roughness on the performance of an axial flow fan for the 1542 mm numerical model and 61° stagger angle. The 'flatter' blade angle was selected to prevent the dominant effect that profile drag has at higher blade angles. They mimicked surface roughness by 'placing' transition strips at 0.08c along the upper and lower surfaces. From this they found that the fan static pressure was almost identical when comparing the 'smooth' (no transition strip model) and 'rough' numerical models, but they saw a 4% increase in power consumption and 4% decrease in fan static efficiency. The unaffected fan static pressure is due to the fan static pressure being a function of the fan profile (more specifically the lift generated by the profile).

Bredell (2005) performed a numerical (CFD) investigation into the performance of axial flow fans in air-cooled steam condensers (ACSC). He numerically modelled a section of a fan array with a commercial CFD code (Fluent) and varied aspects like the platform height and the degree of inlet flow distortion. He numerically compared the performance (all aspects) of two axial flow fans at identical operating conditions and found that the fan with a larger hub-tip ratio (0.4 vs. 0.153) showed superior all-round performance. He verified his numerical models with experimental data from Stinnes (1998) and found very good correlation. His numerical fan models were based on 'blade element theory', or better known as an 'actuator disc model'. Apart from fan comparisons, Bredell also simulated the effects of solid walkways along the edge of the ACSC platform and found that the edge fan's performance (all aspects) can be improved by up to 48% (for certain conditions) with the addition of a well-placed solid walkway.

In 2006, Menter et al. formulated a numerical model that is not only able to solve for laminar flow, but to predict if and where transition to turbulence occurs, and to then solve the turbulent flow region. Although similar analytical models are available, none of these models

are suitable for implementation into modern computational fluid dynamic codes as they all rely on global variables. The use of global variables means that the local cell solution is not possible since the adjacent cells would not contain the required information to solve the model equations. Menter et al. however devised a new transition model that requires only local variables to find a solution, making it perfect for implementation into CFD codes and the parallel environments that are associated with industrial CFD applications. Extensive confirmation testing was done by Menter et al. to develop and refine the model, in this case mainly two-dimensional, and in general, good correlation with experimental data was obtained. Among other aerodynamic effects, the model is capable of predicting laminar separation and reattachment and the subsequently induces transition to turbulence. Although not perfect, this correlation-based transition model is a significant advancement in transition modelling and CFD applications.

The transition model formulated by Menter et al. was further verified and tested by Langtry et al. (2006) for a number of three-dimensional turbomachinery and aerodynamic test cases. The onset and extent of transition in turbomachinery is of significant importance and thus served as a good platform on which to evaluate the three-dimensional performance of this new transition model. The comparison stretched several different scenarios of varying cascades, blade profiles and operating conditions to provide a very comprehensive basis for assessment. It was confirmed time and time again that the new transition model manages to capture behaviour that the traditionally used fully-turbulent models completely overlook. Despite this ability to solve detail in the flow transition region, the model still performs as a normal turbulent model as soon as fully turbulent flow is reached. The new transition model compared well (emphasis was placed on transition onset location, shear stress development and boundary layer reattachment) with the empirical data and serves as a revolutionary platform from which to develop and incorporate better and more comprehensive models.

### 3 REYNOLDS NUMBER AND SURFACE ROUGHNESS INVESTIGATION

This chapter focuses on the numerical and experimental investigation into the effects of dimensionless scaling laws not taking Reynolds and friction effects into account when scaling performance data.

#### 3.1 INTRODUCTION AND OBJECTIVES

Preliminary calculations suggest that the chord length based Reynolds numbers,  $Re_c$ , for the 630 mm diameter scaled fans (at the hub and tip areas of the fan) never reach the point of transition (typically  $7 \times 10^5$  to  $1 \times 10^6$ ) and are thus fully laminar. However, the hub profile of the full-scale fan (9216 mm diameter) operates in the region of transition while the full-scale tip profile is fully turbulent.

One of the objectives of this thesis is to provide the best possible platform for comparing scaled fans to their full scale equivalents. Meyer & Kröger (2004) found that the traditional dimensionless scaling laws do not provide the best basis for performance comparison as these scaling laws completely ignore the effects of Reynolds numbers and surface roughness. They found that when scaling from 1542 mm to 9216 mm diameter, the fan scaling laws overestimate the fan performance by about 4 % and underestimate power consumption at lower flow rates when a difference in Reynolds numbers are not considered. Including surface roughness into the numerical simulation seems to influence power consumption only, and subsequently fan static efficiency, by increasing fan power consumption by about 4 % and decreasing fan static efficiency by the same percentage. Although this seems trivial, in establishing the best possible basis for comparison, these effects need to be taken into consideration. To this end, a pre-testing investigation is to be done into whether or not these effects play an active role in testing (Meyer & Kröger's investigation was done using a combination of numerical methods and blade element data in an actuator disc model).

The first step is to establish a means to mimic the full-scale Reynolds number effects on a smaller scale with specific attention to transition of flow from laminar to turbulent. This will be done using a computational fluid dynamics (CFD) model that incorporates transition models

only recently incorporated into commercial CFD packages, and then implemented on a scale model and tested in a laboratory. The surface roughness effects will be taken into consideration as best possible.

The investigation will initially only be done for the N fan.

### **3.2 SETUP FOR NUMERICAL TRANSITION INVESTIGATION**

The N fan blade profile was simulated as scaled (630 mm) and full-sized (9216 mm) geometries. Instead of doing a three-dimensional (3D) simulation of a blade or a full fan, it was considered sufficient to do two two-dimensional (2D) simulations per problem. A simulation with the blade angle at zero degrees was done for the profiles at the tip and the end of the blade nearest the hub. This was done based on the assumption that the flow change between the tip and the hub is a linear relationship and thus easy to interpolate. It was also assumed that the tangential velocity that the cross-section sees is much greater than the axial velocity and therefore the inlet velocity for the hub and tip simulations of each problem was set equal to the rotational velocity at the specific radius.

The N fan has a constant cross-section profile and chord length. Thus, using Gambit 2.4.6, the same profile was used to generate a mesh for both the tip and hub simulations of the scaled problem. These meshes were then scaled up by the geometric factor of 9216/630 to provide initial meshes for the full-scale problem. Common practice for flow around a stationary object (the inlet velocity simulates the movement of the blade) is to ensure that the mesh extends sufficiently in front of, to the top and bottom of, and the rear of the object in order to capture any wake effects and to ensure that the boundaries do not influence the flow at the object. For this scenario, the mesh extends about five chord lengths in front of the object, about 15 chord lengths behind the object, and 20 blade thickness units to the top and the bottom. Since the simulations are 2D, the meshes were not expected to be very large (cell count) and thus extensive near-wall boundary layers were created for each simulation.

The boundaries for the simulations are all identical in their setup. The front of the mesh is defined as a velocity inlet, the top and bottom as symmetry planes and the rear of the mesh as

an outflow boundary. The velocity inlet was used to define the velocity of the incoming flow, the turbulence intensity, intermittency and the turbulence length.

According to the Fluent User's Guide, the turbulence length,  $\ell$ , may be calculated as

$$\ell = 0.07 \cdot L \quad (3.1)$$

where L is the characteristic length of the object, which in this case refers to the chord length.

The turbulence intensity is a function of the velocity fluctuations present in the flow. Values of 1 % and less are typically considered as low and values of 10% and greater are considered high levels of turbulence intensity. For this comparison, a value of 2 % was chosen as this is generally considered an acceptable value for free-stream laboratory conditions where modern low-turbulence wind tunnels are not available (Fluent User's Guide).

The intermittency equation is used by the Transition-SST turbulence model to trigger the transition process (Menter et al., 2006). For the inlet flow conditions, an intermittency value of one means the flow is fully developed and has an even turbulence distribution with a turbulence intensity as specified. For a detailed explanation of the intermittency value, refer to the Fluent Theory Guide.

For the scaled model, a rotational speed of 1300 rpm was chosen since at this speed, the volume flow would be within the calibrated range of the anemometers for later experimental confirmation (see Appendix A). The full-scale fans operate at a rotational speed of 125 rpm. Using the actual fan diameters and the rotational speeds, radii and chord lengths, the inlet flow velocities and turbulence lengths were calculated and are tabulated in Table 3.1.

**Table 3.1** Inlet parameters for Reynolds number numerical investigation

	<b>Inlet Velocity [m/s]</b>	<b>Turbulence Length [m]</b>
<b>Full-Scale Hub</b> ( $\varnothing$ 9145 mm)	15.014	0.051
<b>Full-Scale Tip</b>	59.854	
<b>Scaled Hub</b> ( $\varnothing$ 625.15 mm)	10.673	0.004
<b>Scaled Tip</b>	42.556	

Importing the meshes into Fluent 12<sup>®</sup>, an initial single level of refinement was done in a strip throughout the middle of the mesh as this is the area that would see most of the flow activity. An example of this ‘starting’ mesh is shown in Figure 3.1.

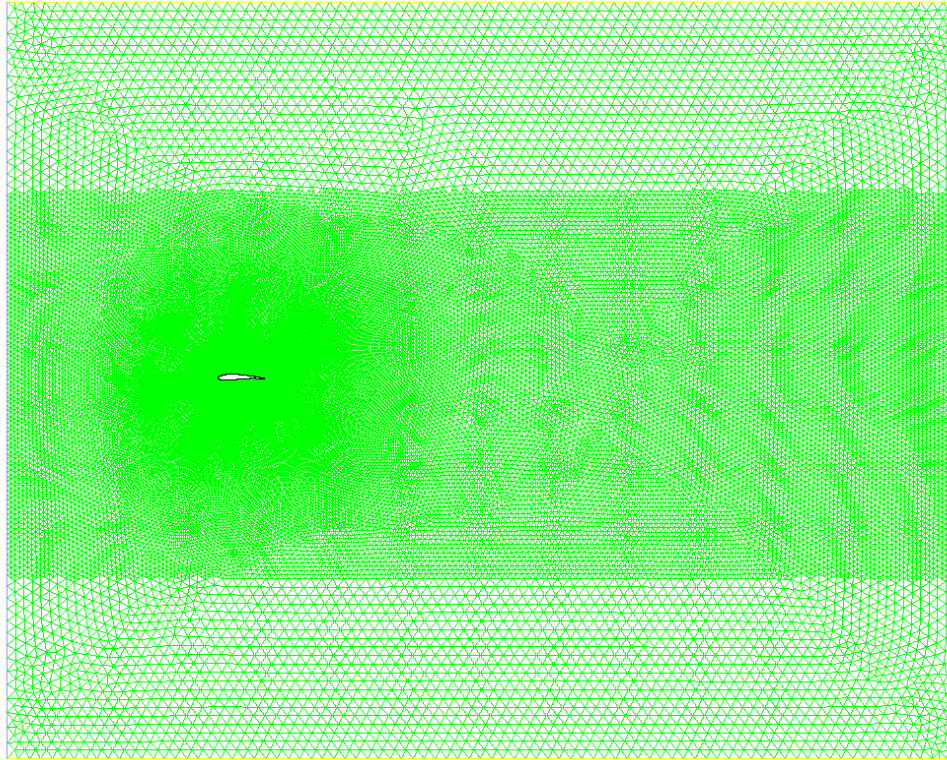


**Figure 3.1** Generic starting mesh for numerical Reynolds number investigation

Each simulation was allowed to complete and the mesh was further refined using each simulation's specific solution. The focus of each refinement process was to prevent excessive velocity gradients and to meet the Transition-SST turbulence model requirements of a  $y^+$  value of approximately one. The  $y^+$  value is an indication of the near wall cell height and is an important measure to determine whether the boundary layer mesh meets the requirements of the turbulence model. An incorrectly sized boundary layer mesh can result in instability and inaccurate results. A refined mesh is shown in Figure 3.2. Note the refined ‘tail’ behind the profile that allows the simulation to capture wake effects.

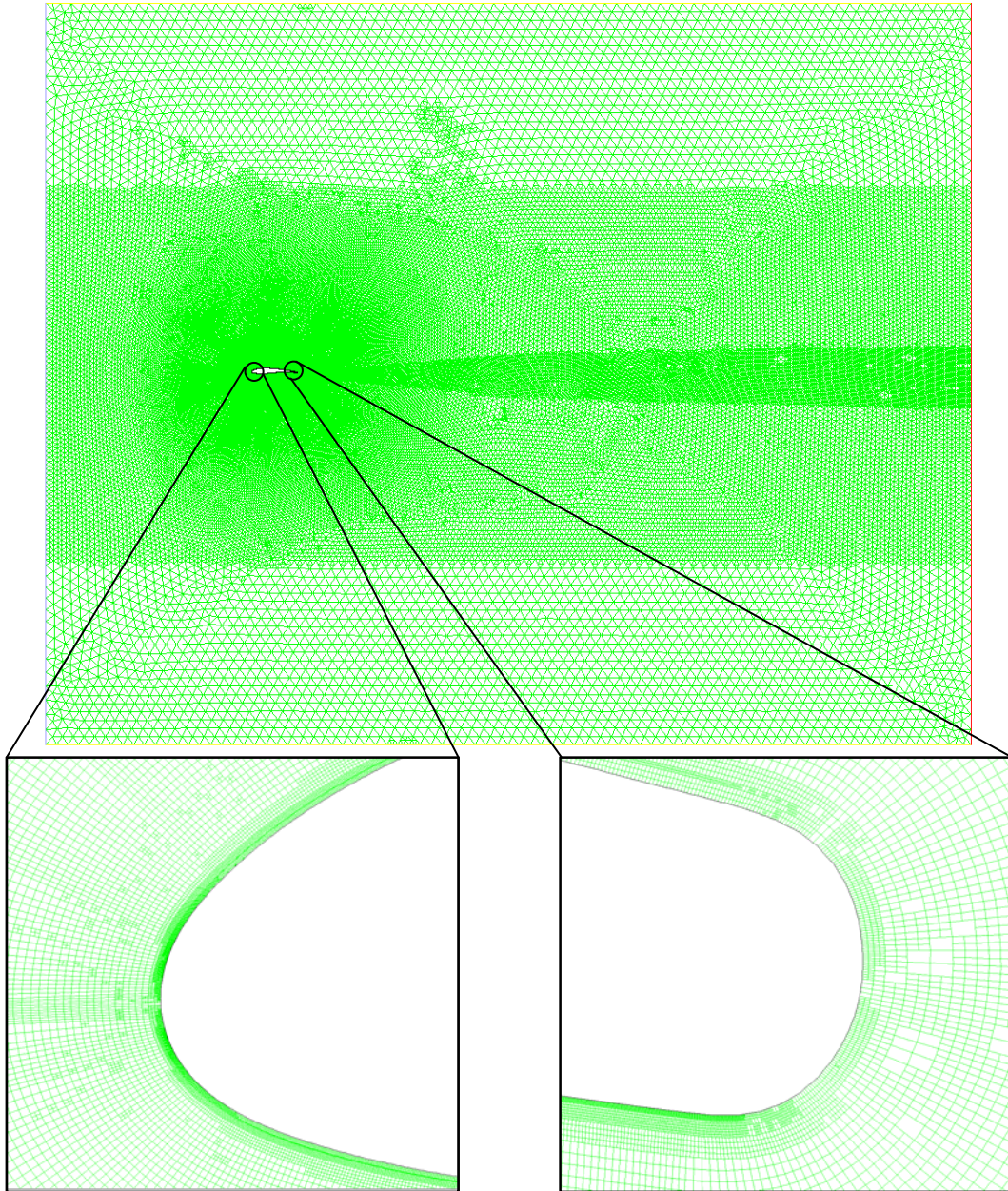


**Figure 3.2** Refined mesh for numerical Reynolds number investigation

For the creation of this mesh, it was important to obtain sufficiently small node spacing in areas of high curvature, like the nose and tail, to ensure an even curvature. This is because the meshing process performs linear interpolation between nodes and thus, a low resolution mesh would simply 'cut out' areas of higher complexity and curvature. Despite a very fine boundary layer, these nodes still form distinctive points in the mesh, albeit very minute in this case, and was considered sufficient to mimic the effect of surface roughness for the manufactured

scaled model N fans given the manufacturing process and finishing. Therefore, for the scaled simulations, no surface roughness parameters were specified.

Full-scale fans in large-scale fan arrays quickly gather oil and dirt and this results in a surface finish comparable to 180 grit sanding paper. According to a laboratory report (Nanovea, 2009), this results in a mean surface roughness height of approximately 20  $\mu\text{m}$ . A Roughness Constant of 0.5 is perfectly suited for sandpaper-like surfaces (Fluent User's Guide).

Since the aim of this thesis is to provide the most accurate basis for comparison between laboratory testing and actual installations, this CFD investigation also took into consideration the varying atmospheric conditions between Stellenbosch and that of the area where a typical installation might be found. The use of large-scale fan arrays are concentrated in the inland, northerly reaches of South Africa (Gauteng and Northern Province) where water is not suitable for industrial cooling purposes given its scarcity. A purely altitude based approximation was made regarding the atmospheric pressures in Stellenbosch and Johannesburg, and combined with average air temperatures as approximated in a Stellenbosch University laboratory and that of the air in the 'Highveld'. From this the average density for each location was calculated. The atmospheric conditions used for this numerical investigation are found in Table 3.2.

**Table 3.2** Atmospheric conditions for numerical simulations

	<b>Pressure [Pa]</b>	<b>Temperature [°C]</b>	<b>Density [kg/m<sup>3</sup>]</b>	<b>Viscosity [kg/ms]</b>
<b>Full-scale</b> (Johannesburg)	81994.3	20	0.958	1.835415e-05
<b>Scaled</b> (Stellenbosch)	99713.7	15	1.2057	1.79423e-05

All differencing schemes were set to second-order ('upwind' where available) and relaxation factors were left on default values. Very important is the use of the Green-Gauss Node Based spatial discretization which provides the best gradient discretization for unstructured meshes.



### 3.3 NUMERICAL TRANSITION INVESTIGATION

According to Menter et al. (2006), when simulating a blade profile, grid independent solutions were achieved when more than 200 nodes were used to define the profile, with  $y^+$  values of 1 and a normal grid expansion ratio of 1.1. All simulations in this investigation have at least 400 nodes that define the profile, a grid expansion ratio of 1, and all final solutions have  $y^+$  values very close to 1. Based on the work of Menter et al. it was therefore expected that grid independence was achieved, however, since so many other details regarding the simulations from Menter et al. are unknown, a quick grid independence test was done on the simulations for this investigation.

For the grid independence test, gradient-based mesh refinement was done based on pressure gradients. The refinement criterion was customized for each simulation in order to achieve a cell count increase of at least 10 %. Since the wall shear force varies from laminar to turbulent flow, a good indication of grid independence would be the drag force since any solution shift in terms of transition to turbulence would influence the wall shear stress and subsequently also the drag force ( $F_x$ ). A variation of less than 1 % between the two solutions could be considered sufficient to indicate grid independence. Table 3.3 tabulates the comparison in drag force between the new (fine) mesh and the original solution.

**Table 3.3** Drag force comparison for grid independence confirmation

	<i>Original</i>		<i>Fine</i>		$\Delta F_{x,total}$ [%]
	<b>Pressure [N]</b>	<b>Viscous [N]</b>	<b>Pressure [N]</b>	<b>Viscous [N]</b>	
<b>Full-scale (hub)</b>	0.41245778	0.59584547	0.41134481	0.59377589	-0.3156
<b>Full-scale (tip)</b>	6.5871052	9.5021284	6.7889754	9.2325649	-0.4207
<b>Scaled (hub)</b>	0.063091937	0.036265133	0.063086899	0.036272435	-0.0023
<b>Scaled (tip)</b>	0.41060193	0.48831656	0.40797599	0.48813788	-0.312

From the drag force comparison in Table 3.3, it is apparent that the solutions are indeed grid independent. It can also be accepted that the suggested guidelines to ensure grid independence (at least 200 profile nodes,  $y^+ \approx 1$  and boundary grid expansion ratio of 1.1) are indeed applicable to this scenario. However, closer investigation into the vector flow solution between the original and fine solutions for the full-scale simulations revealed that in the tip profile solution, the finer mesh manages to capture detail in the flow field, specifically the

vortices at the trailing edge as seen in Figure 3.3. This causes the transition point to move backwards along the blade compared to the original solution, as indicated by the skin friction coefficient comparison in Figure 3.4. Thus, despite a comparable drag force, it is obvious that different flow solutions can still produce the same total drag (or lift) effects. Similar comparisons of skin friction coefficient comparisons were done for all other solutions and were found to be identical, consequently, for all except the full-scale tip profile simulation, comparing the total drag force proved a good measure of grid independence. Additional refinement on the full-scale tip simulation was done until the point of transition stabilized. From this it can be concluded that the continued fluctuations of the vortices at the trailing edge causes the pressure induced drag to fluctuate too, and excludes the total drag force as a means of grid independence check for cases with highly turbulent wakes.

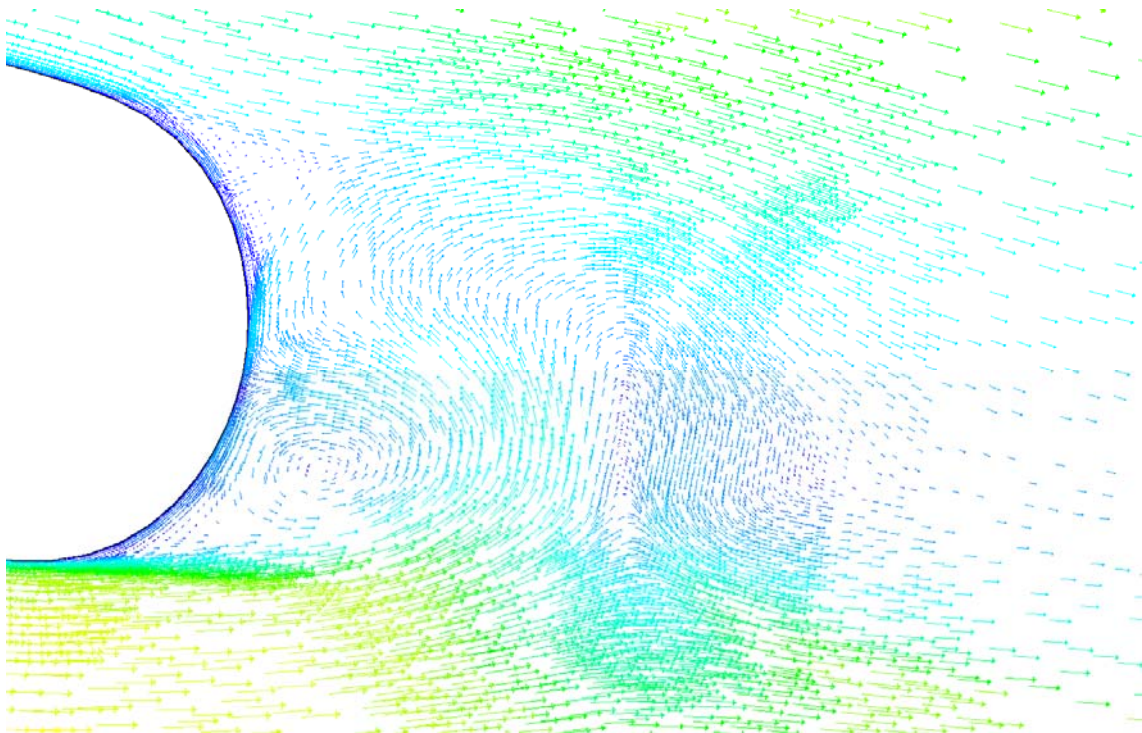


**Figure 3.3** Vortices at trailing edge on full-scale tip solution

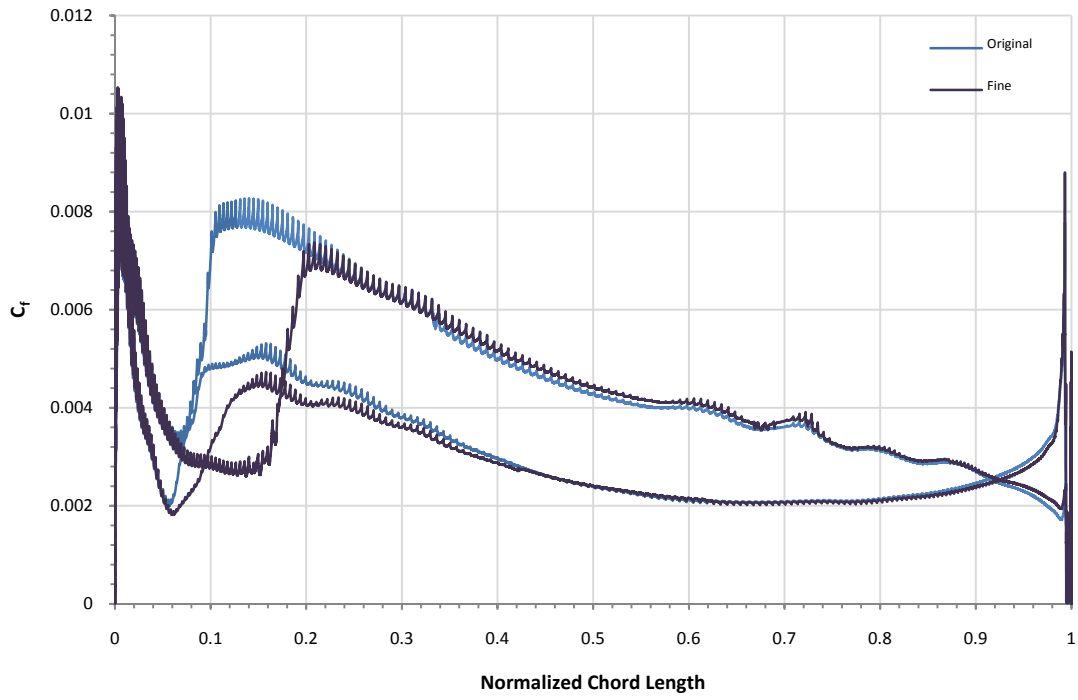


Figure 3.4 Fine and original mesh  $C_f$  comparison for full-scale tip solutions

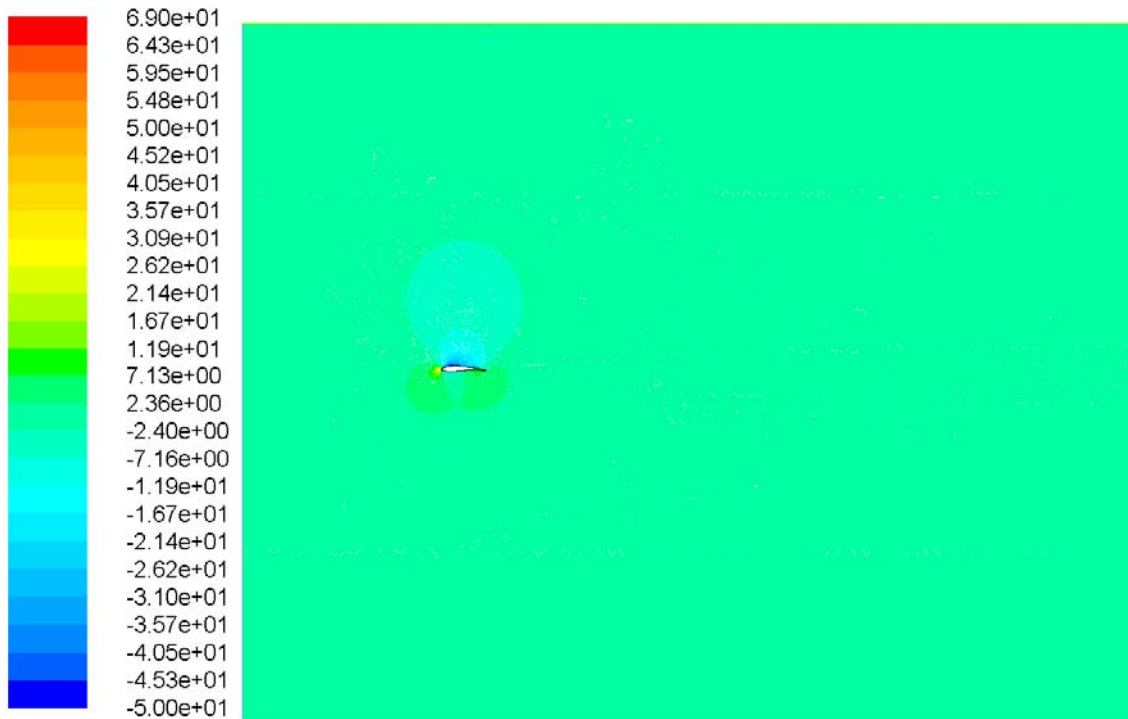
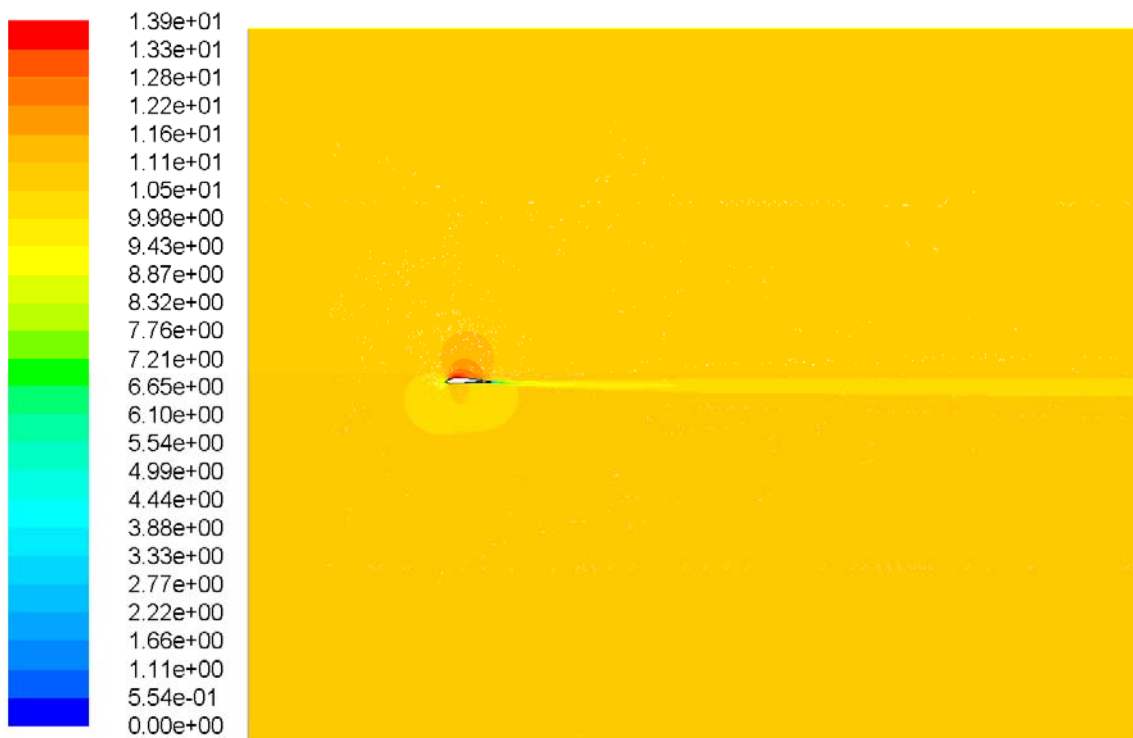


Figure 3.5 Static pressure distribution for scaled hub solution

Since the meshes are identical, save for scale and near-wall layer refinement, the general solutions are all comparable in contours plots (actual values are simulation specific). The static pressure and velocity distributions for the scaled hub simulation are shown in Figure 3.5 and Figure 3.6, and the static pressure and velocity distributions for the full-scale tip (fine grid) simulation are shown in Figure 3.7 and Figure 3.8.

One of the distinct differences is that the velocity wake from the scaled hub solution dissipates much slower than the wake from the full-scale tip solution. This could be attributed to the greater wake turbulence in the full-scale solution, which in turn causes the kinetic energy to dissipate quicker due to the larger and more frequent fluctuations.



**Figure 3.6** Velocity magnitude distribution for scaled hub solution

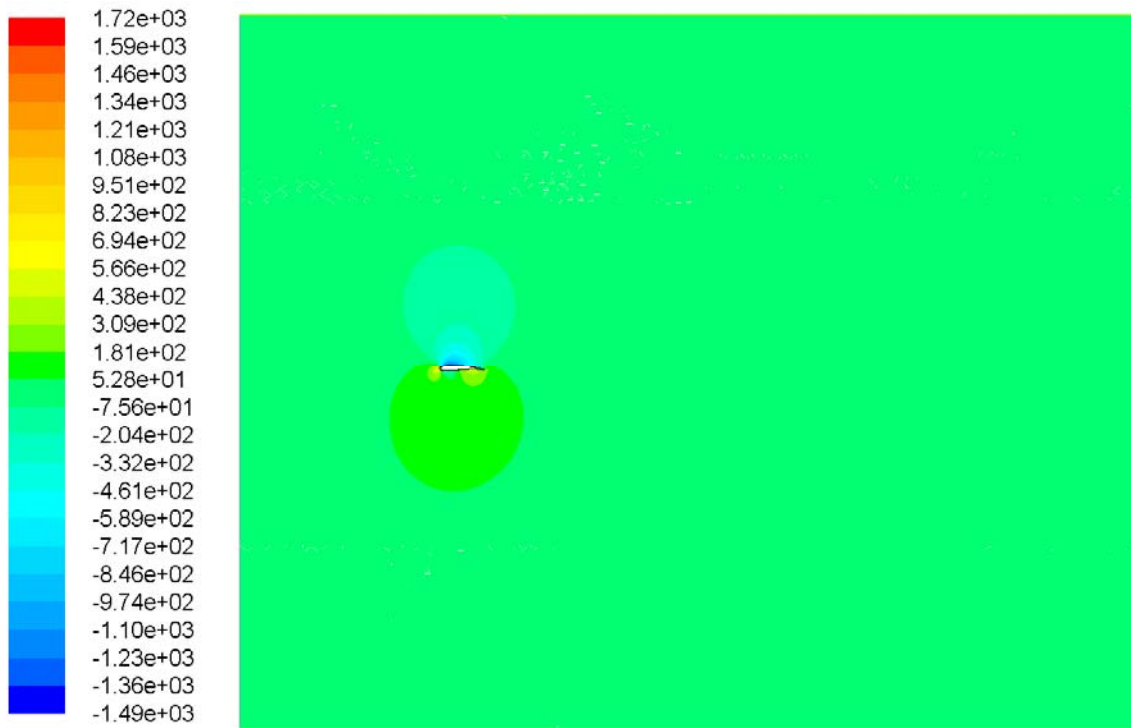


**Figure 3.7** Static pressure distribution for full-scale tip solution

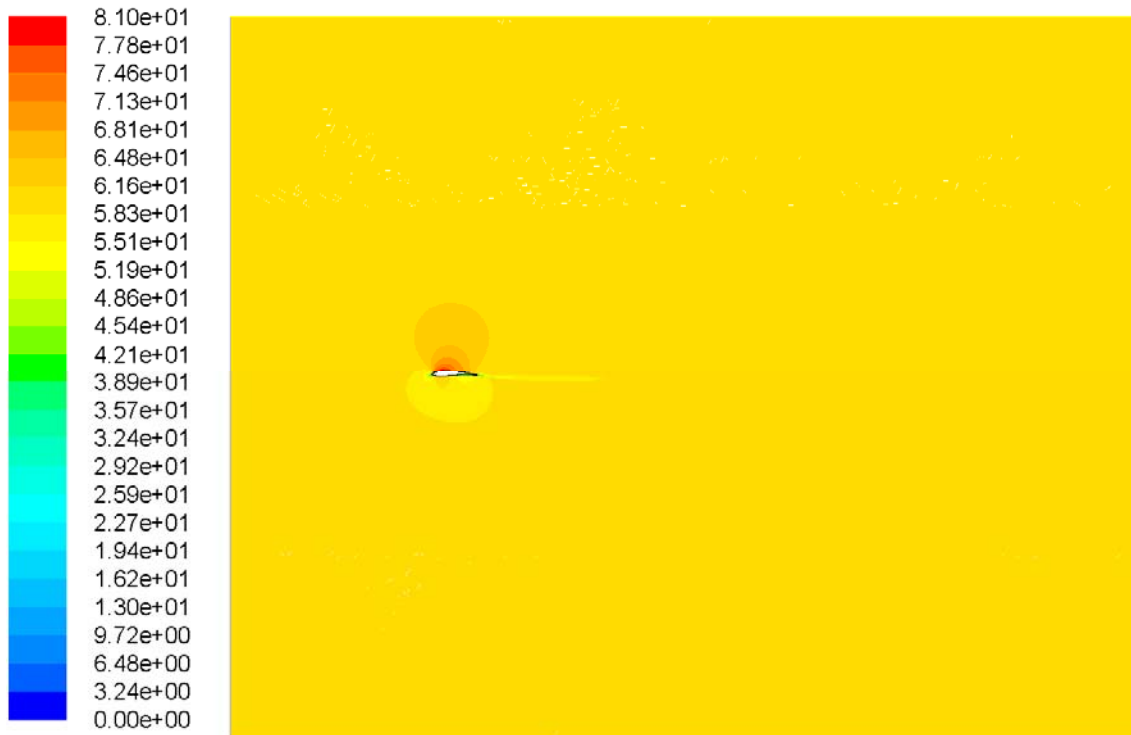


**Figure 3.8** Velocity magnitude distribution for full-scale tip solution

As pointed out earlier, the shear stress on the profile wall is a function of the type of flow along the wall. The sudden increase in shear stress is thus indicative of the onset of transition.

The skin friction factor,  $C_f$ , which is a function of shear stress, was used by Menter et al. (2006) as a basis for comparing and validating the new transition model, and will also be used in this investigation to compare transition onset positions for the full-scale and scaled problems. The  $C_f$  plots are shown as a function of x-distance (chord) and expressed as a value perpendicular to the profile (wall). For comparison between the scaled and full-scale skin friction factors, the chord lengths were normalized. The comparison for the hub profile of each problem's solutions is shown in Figure 3.9, and the tip profile solution comparison in Figure 3.10.

As seen for both the hub and tip comparisons, the initial calculations that the scaled model is fully laminar holds true. However, on the full-scale solutions, it is clearly visible where the flow transitions from laminar to turbulent by the sudden increase in skin friction coefficient (the upper curve is the upper profile surface). For the hub comparison, transition along both surfaces occurs at almost the same chord position while the tip comparison shows a slight transition delay on the upper surface. The delay in transition can possibly be attributed to the freestream flow pinching the boundary layer and preventing boundary layer development.

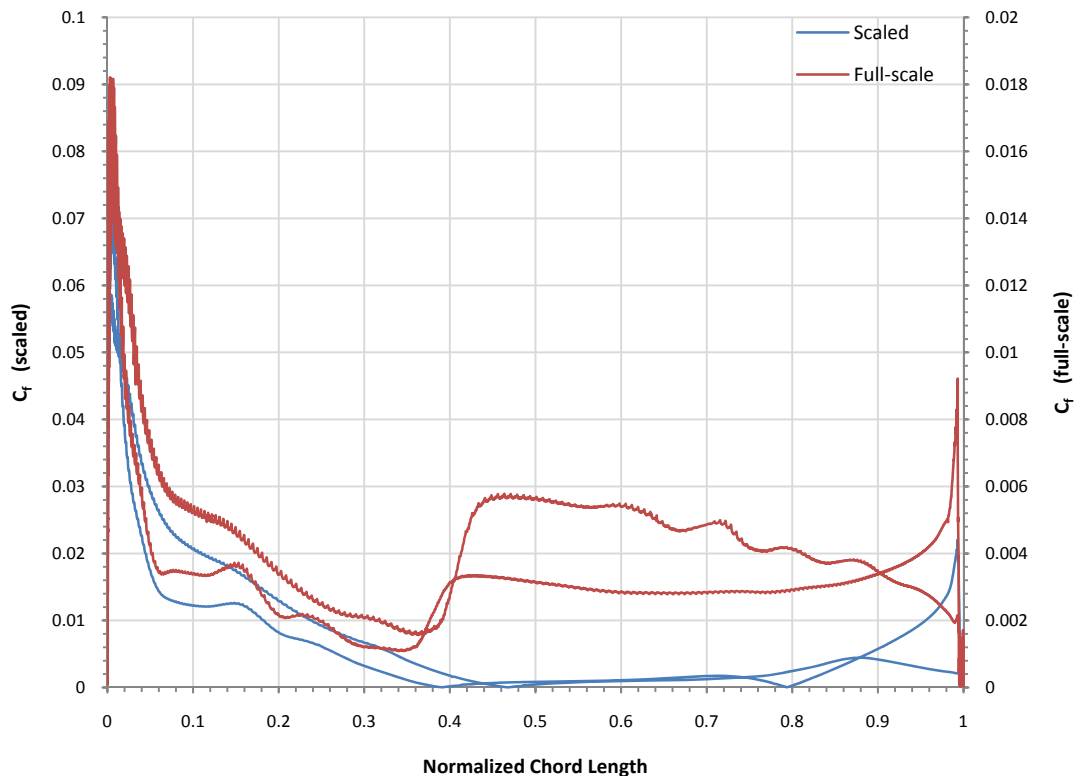


**Figure 3.9**  $C_f$  comparison for hub solutions of scaled and full-scale problems

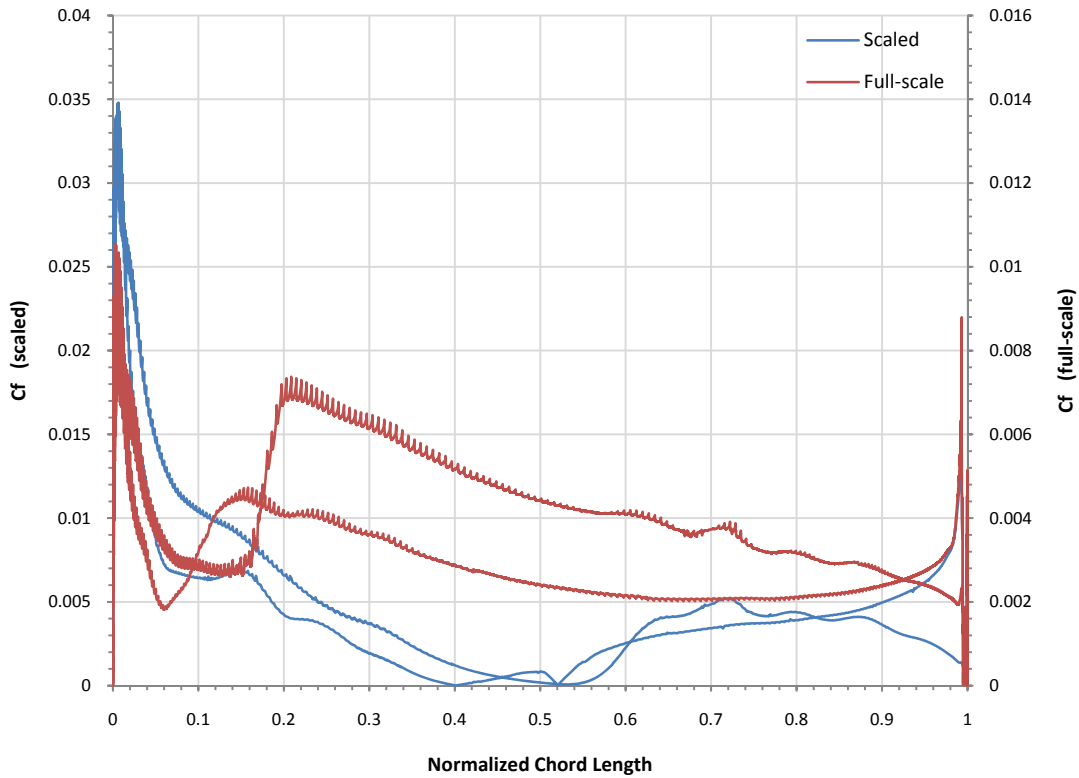


Figure 3.10  $C_f$  comparison for tip solutions of scaled and full-scale problems

### 3.4 NUMERICAL INDUCED TRANSITION EVALUATION

Having established where transition occurs for the full-scale problem, the challenge is to induce transition on the scaled problem at a similar relative chord position.

The use of two-dimensional roughness, like a wire or cylinder stretched across the flow, introduces wake disturbances that increase the level of the Tollmien-Schlichting waves growing downstream of the element (White, 2006). The wire height,  $k$ , needs to be larger than 0.3 of the local displacement thickness,  $\delta^*$ , at the position of the wire,  $x_k$ , in order to affect the point of transition,  $x_{tr}$  (White, 2006). Figure 3.11 illustrates the concept and parameters for inducing transition with the use of two-dimensional roughness elements.

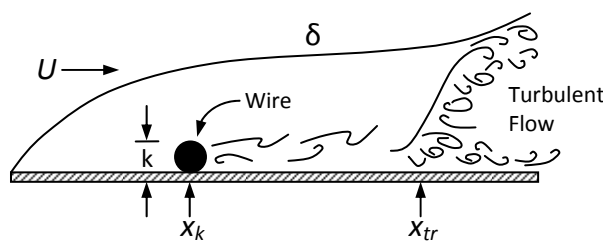
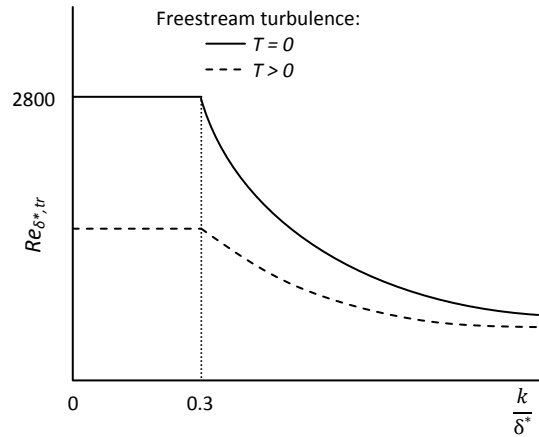


Figure 3.11 Flat plate with trip wire (White, 2006)

The transition displacement thickness Reynolds number,  $Re_{\delta^*,tr}$ , only starts to decrease after the  $k/\delta^*$  value increases above 0.3, and decreases in the shape of a hyperbolic curve as shown in Figure 3.12.



**Figure 3.12** Decrease in transition position as  $k/\delta^*$  (White, 2006)

According to Gibbings (1959) the criterion for a two-dimensional roughness element to trip flow into turbulence at the element (in this case a tripwire) is

$$\frac{Uk}{\nu} \approx 826 \quad (3.2)$$

From Figure 3.9 and Figure 3.10 it is possible to obtain the absolute chord position at which the boundary layer transition is required to occur at. By meeting the wire-thickness Reynolds number criteria as set by Gibbings, placing a tripwire at the required location should induce transition immediately after the wire.

In order to obtain the correct wire thickness to induce transition, Equation 3.2 can be rewritten as

$$k \approx \frac{826\nu}{U} \quad (3.3)$$

Substituting the properties from Table 3.2 and freestream velocities from Table 3.1 into Equation 3.3, the trip wire size for transition at the hub was found to be  $k \approx 1.152$  mm and wire size for transition at the tip was found to be  $k \approx 0.3$  mm. Since variable thickness wires are not feasible, a uniform wire thickness had to be selected based on the minimum requirements to ensure transition at both the hub and tip. The closest standard gauge wire thickness is a SWG18 or 1.219 mm.

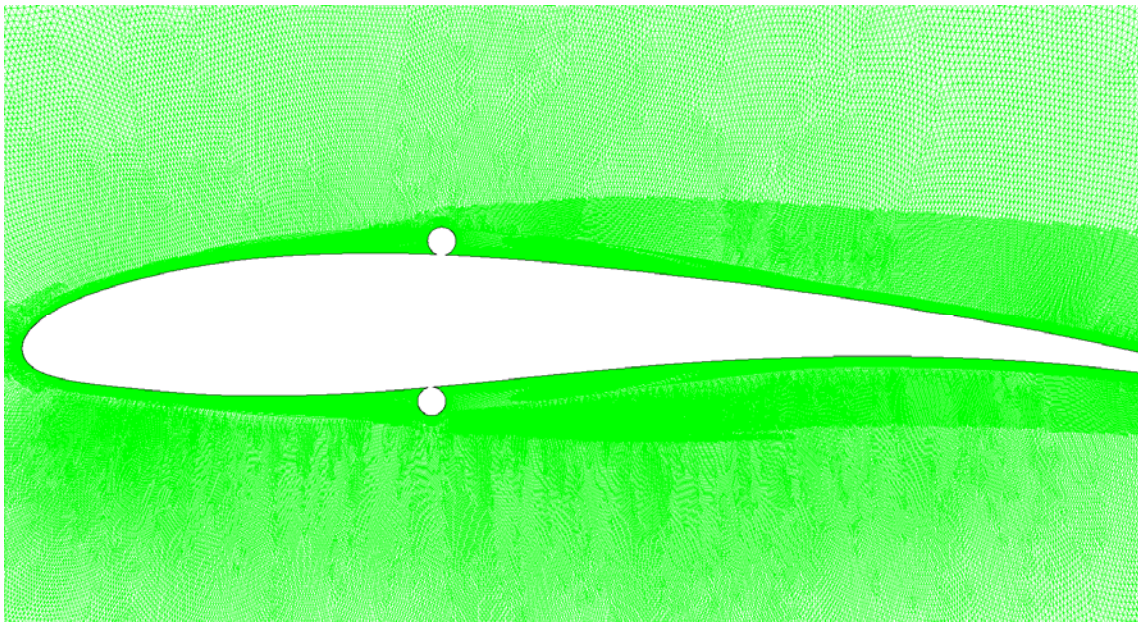


Table 3.4 specifies where these tripwires need to be placed. Note that the wire position varies for the upper and lower surfaces of the profile.

**Table 3.4** Transition wire position for scaled fan

	<b>% chord length</b>	<b>x position (CFD local coordinate)</b>
<b>Hub (upper)</b>	36.4	-0.00920835
<b>Hub (lower)</b>	35.6	-0.00964276
<b>Tip (upper)</b>	15	-0.0198457
<b>Tip (lower)</b>	6	0.0243138

The effectiveness of the specified trip wire at the hub was evaluated using the same two-dimensional CFD simulation that was used in Section 3.2. The trip wires are shown in Figure 3.13.



**Figure 3.13** Two-dimensional mesh of hub simulation featuring 1.219 mm trip wires at transition position

This solution identified two major problems with using the 1.219 mm trip wire to initiate transition at the wire. The first was that despite the trip-wire Reynolds number falling in the range  $0 \leq Re_{x_k} \leq 1.53 \cdot 10^6$  as specified by Gibbings, no transition was induced. In Figure 3.14 it can be seen how the trip wire causes a significant spike in the local shear stress at the wire positions and a small increase in the skin friction value for a small section after the trip wire, however boundary layer reattachment can be seen at about the 60 % chord length mark. This

suggests that instead of introducing wake disturbances, the wire is actually large enough to influence the aerodynamics of the profile and cause laminar separation at the wire. This is confirmed from the velocity magnitude plot in Figure 3.15 where it can be clearly seen that the trip wire causes a low-velocity recirculation zone behind it which, based on the velocity contours, creates the impression of a thicker blade profile. Considering the frontal area, the height of the profile increases from approximately 6 mm to slightly more than 8 mm, which represents a 33 % increase. It was concluded that tripping the flow at the wire position at the hub is not possible for such a low Reynolds number. The trip wire diameter is too large and will have a direct influence on the aerodynamic performance of the profile without inducing the desired Reynolds number effects.

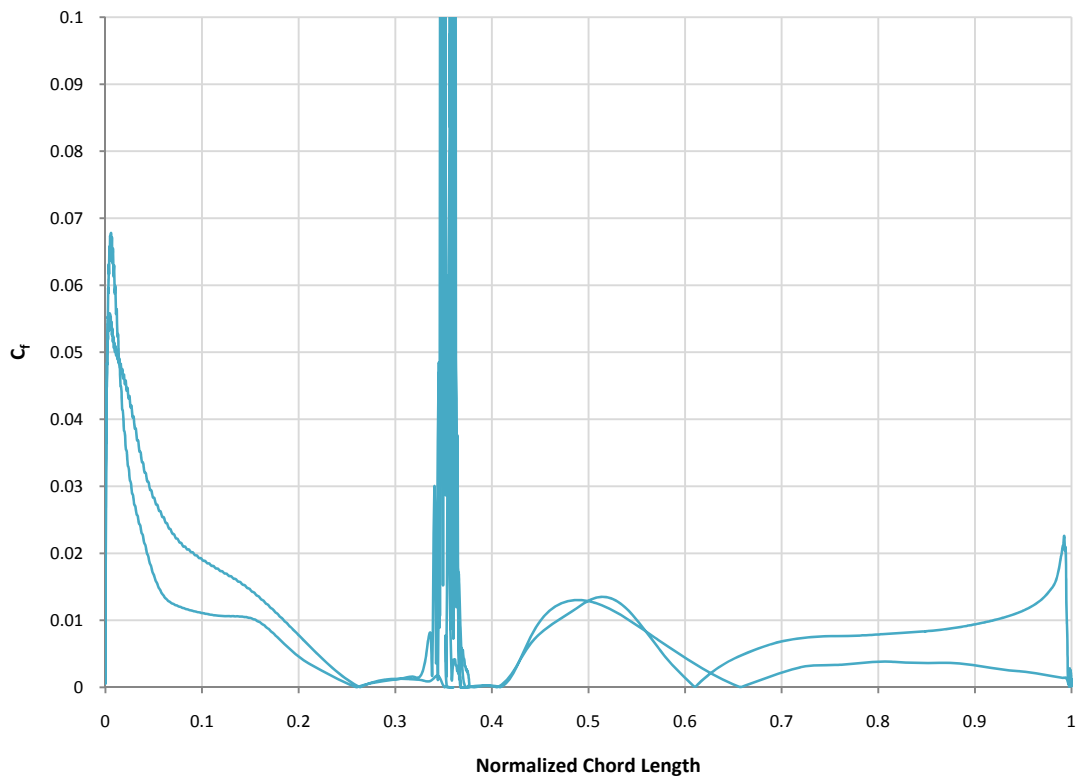


**Figure 3.14**  $C_f$  of scaled hub solution for induced transition (at trip wire 1.219 mm trip wire)

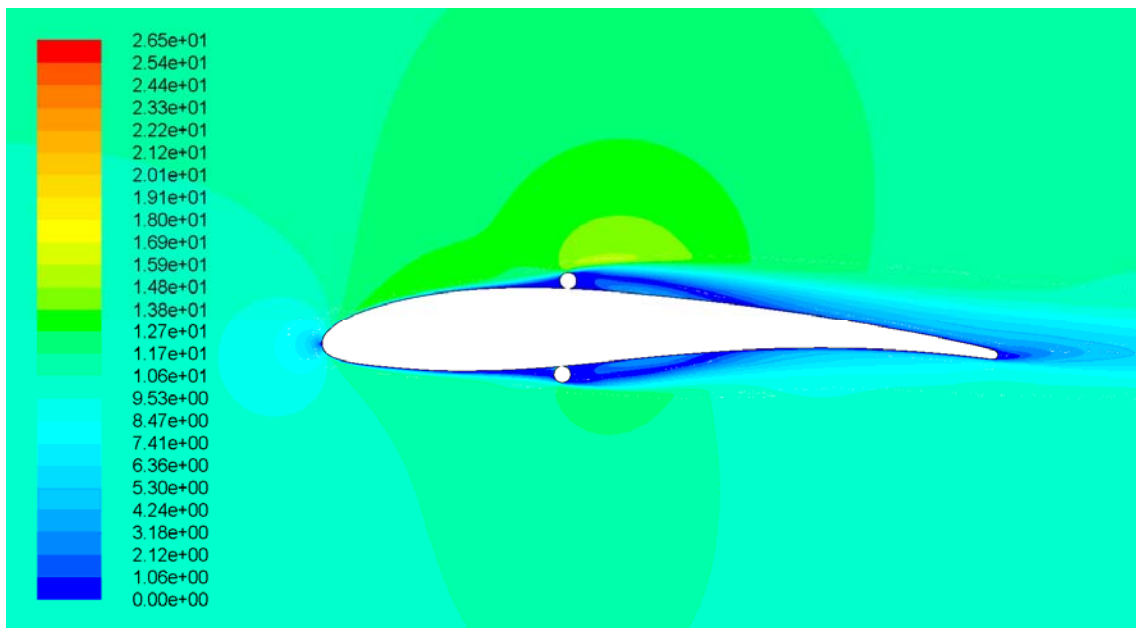


**Figure 3.15** Velocity magnitude distribution of scaled hub featuring trip wire (1.219 mm trip wire)

However, since the tip profile freestream velocity is significantly greater than the hub profile velocity, and the wire thickness obtained from the ‘trip criterion’ is also much thinner, one possibility is to use ‘transition at the wire’ theory for the tip, and ‘transition downstream of the wire’ theory for the hub, and assume that interpolation between the tip and hub is sufficiently accurate to represent the Reynolds number effect. The closest standard wire gauge for the tip criterion is SWG30 which is a thickness of 0.315 mm. This means that the frontal area of the profile will only increase by roughly 10 % as opposed to the 33 % when using 1.2 mm. The increased Reynolds number due to the higher freestream velocity will also increase the likelihood that the wire will induce the necessary wake disturbances to cause transition. The placement of the wire for the tip simulation will remain as given in Table 3.4, but new positions at the hub had to be determined.

Gibbings (1959) compared three flat-plate boundary-layer transition models for determining key values to achieve and predict transition downstream of a wire. He then formulated his own more accurate but also more complicated model. The model that was next best to Gibbings’ own was the model by Tani & Sato (1956) which slightly over-predicted the transition behaviour compared to experimental results, but is very simple and easy to implement. Since the transition position ( $x_7$ ) and wire thickness are known, Equation 3.4 was simply used to solve the position of the wire ( $x_k$ ) (Tani & Sato, 1956).

$$\frac{1}{R_k} = \frac{1}{840} \left( \frac{x_T}{x_k} \right)^{\frac{1}{2}} \quad (3.4)$$

where  $x_T$  and  $x_k$  are both measured as a distance along the profile from the nose (upper and lower curves) in order to be comparable with the flat-plate theory. For a transition position of 19.1 mm for the upper surface and 18.2 mm for the lower surface, the wire positions were found to be 1.38 mm and 1.316 mm respectively. A numerical confirmation of this new trip wire scenario was done in order to evaluate the trip wire effectiveness.

The new mesh for the hub simulation in Figure 3.16 clearly shows the much smaller trip wires located at the nose of the profile. It also reveals that the use of the thinner trip wires will not affect the frontal area as with the SWG18 trip wires since the SWG30 trip wires are located at the leading edge of the profile and do not increase the frontal area of the profile. From Figure 3.17 it can be seen that the velocity magnitude distribution does not create the thicker near-wall layer as seen with the use of the SWG18 wires. The thinner trip wires still produce a low-pressure zone immediately after the wires, but it is significantly smaller than the low-pressure zone caused by the SWG18 wires. Figure 3.17 also provides a comparison between the original (fine mesh) solution and the 0.315 mm trip wire solution and clearly shows that the trip wire has a minutely small influence on the flow field, which validates that the trip wire itself will not influence the profile performance.

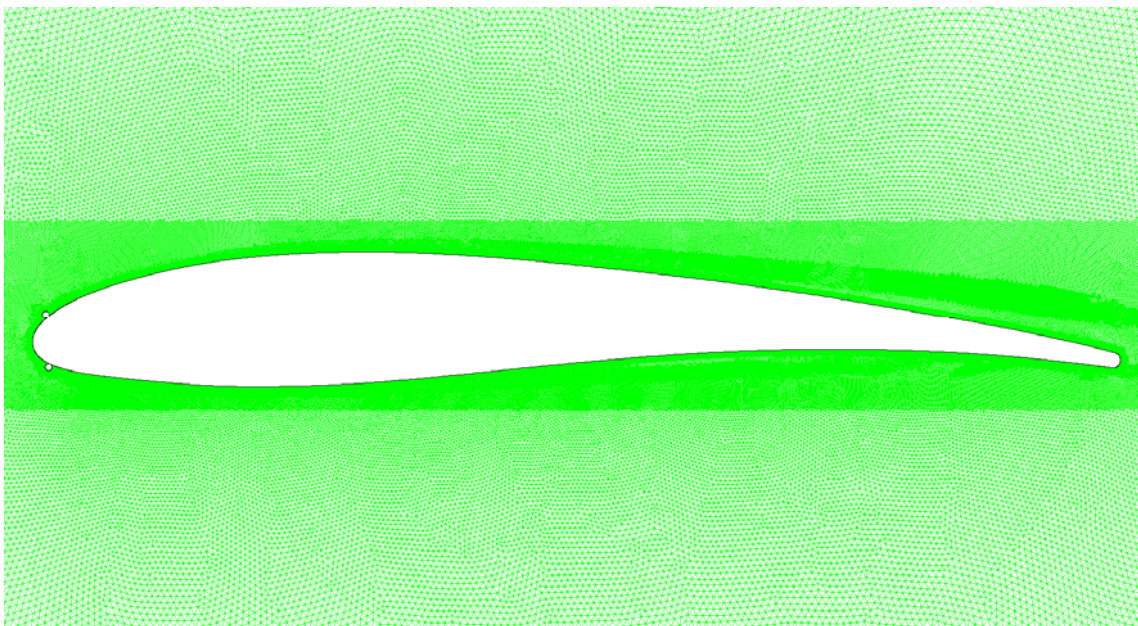


**Figure 3.16** Two-dimensional mesh of hub simulation featuring 0.315 mm trip wires at leading edge

As before, the skin friction coefficient is a good indication of whether transition to turbulence was achieved. A comparison between the skin friction coefficients from the trip wire solution and the full-scale solution is shown in Figure 3.18. According to the CFD results at least, this trip wire does not induce the desired downstream transition at the hub of the scaled N fan. Immediately after the wire, there is a sudden increase in shear stress which can be attributed to the small recirculation zone caused by the wire, however, the flow past the wire appears to reattach to the profile, which is marked by the sudden decrease in the shear stress. From this point on, the skin friction coefficient follows the same behaviour as the solution without the trip wire (see Figure 3.9 for non-tripped solution). This suggests that the range set by Gibbings (1959) was either very optimistic or that the non-flat surface of the profile does not allow the development of the boundary layer as it would on a flat plate, and that a chord based Reynolds number of  $\sim 55\,000$  is still not enough to allow the trip wire to cause the necessary wake disturbances to induce transition.

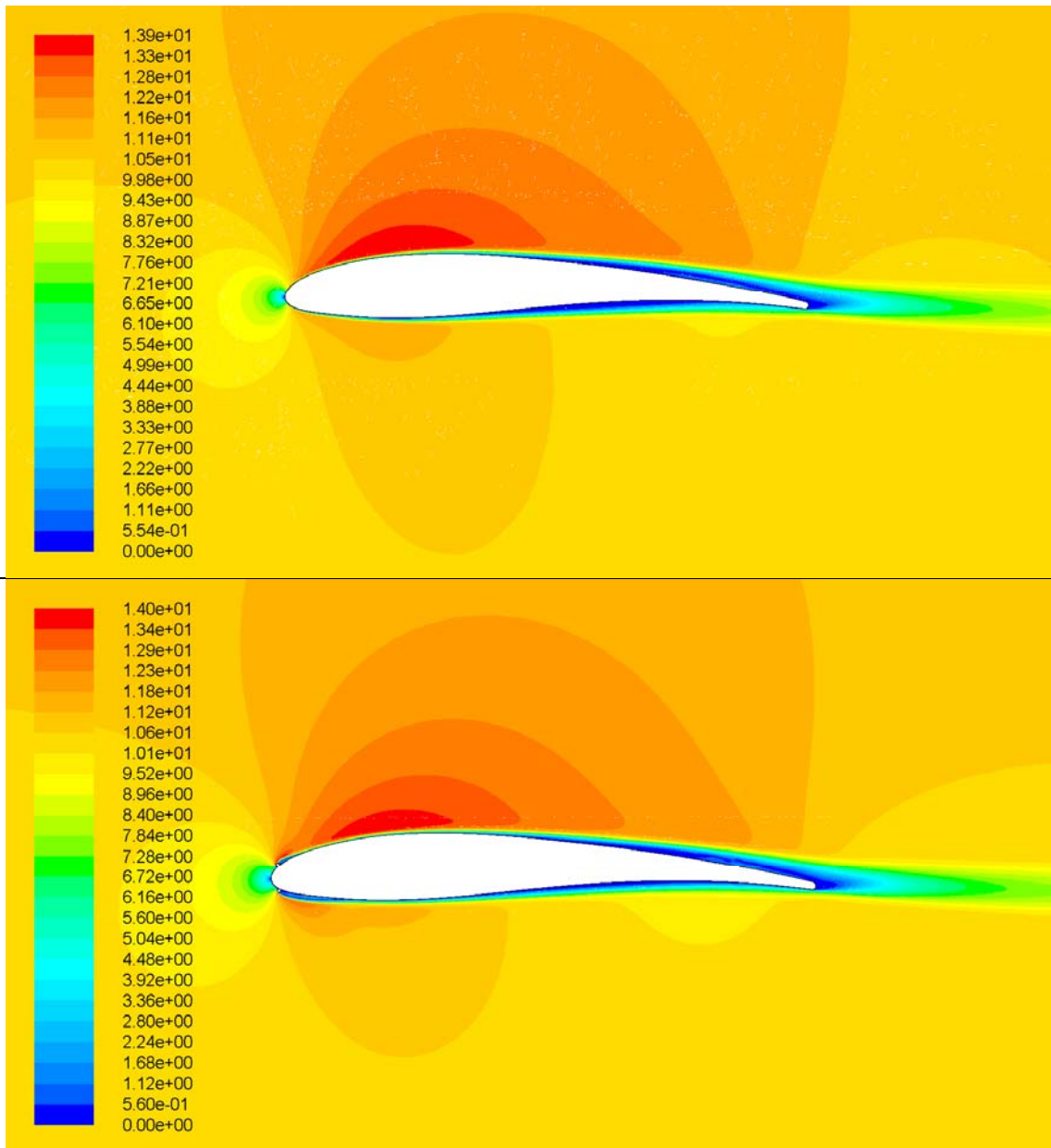


**Figure 3.17** Comparison of velocity magnitude distribution between fine solution (top) and 0.315 mm trip wire solution (bottom) at hub

Following the same procedure as for the hub evaluation, the performance of a trip wire at the tip was determined numerically. As mentioned previously, the use of the SWG30 wire at the tip follows 'transition at the wire' theory and thus the desired effect is to see an increase in the shear stress from the wire position onwards. The placement of a 0.315 mm trip wire at the locations specified in Table 3.4 can be seen in Figure 3.19. Again, the positioning of the trip wires does not increase the frontal area of the profile significantly, which should allow the trip wire to have no direct effect on the global flow field. However, a secondary influence on the

global field (drag and lift) is expected due to the induced transition to turbulent flow across the profile.

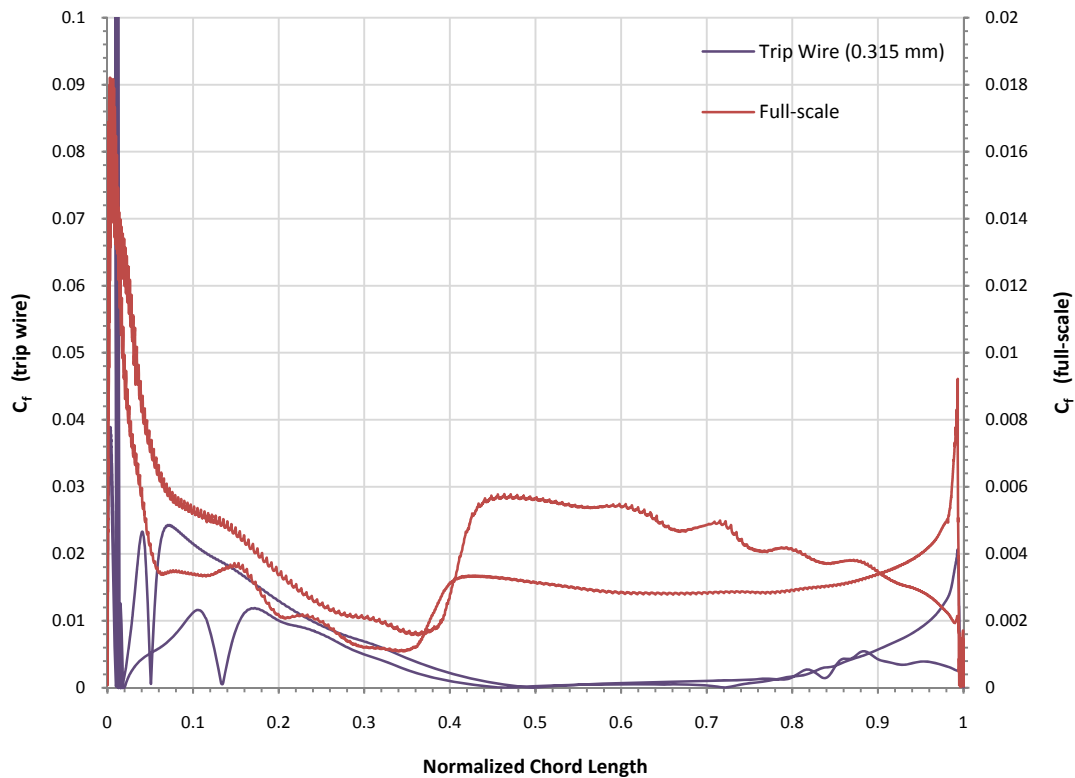


**Figure 3.18**  $C_f$  comparison for hub solution of scaled induced transition (downstream of trip wire, 0.315 mm trip wire) and full-scale hub solution

The velocity distribution can be seen in Figure 3.20 and shows flow acceleration over the trip wires. A low-pressure recirculation zone immediately behind the trip wires can also be seen (small blue region). Comparing the trip wire solution to the original (fine mesh) tip solution shows some resemblance between the two contour plots. Despite the trip wire on the upper surface being positioned at the area of greatest velocity and thus having the greatest potential to affect the flow, the magnitude of the contours of the original and trip wire solutions are still in the same range, thus confirming that the trip wires do not have any drastic effect on the flow.

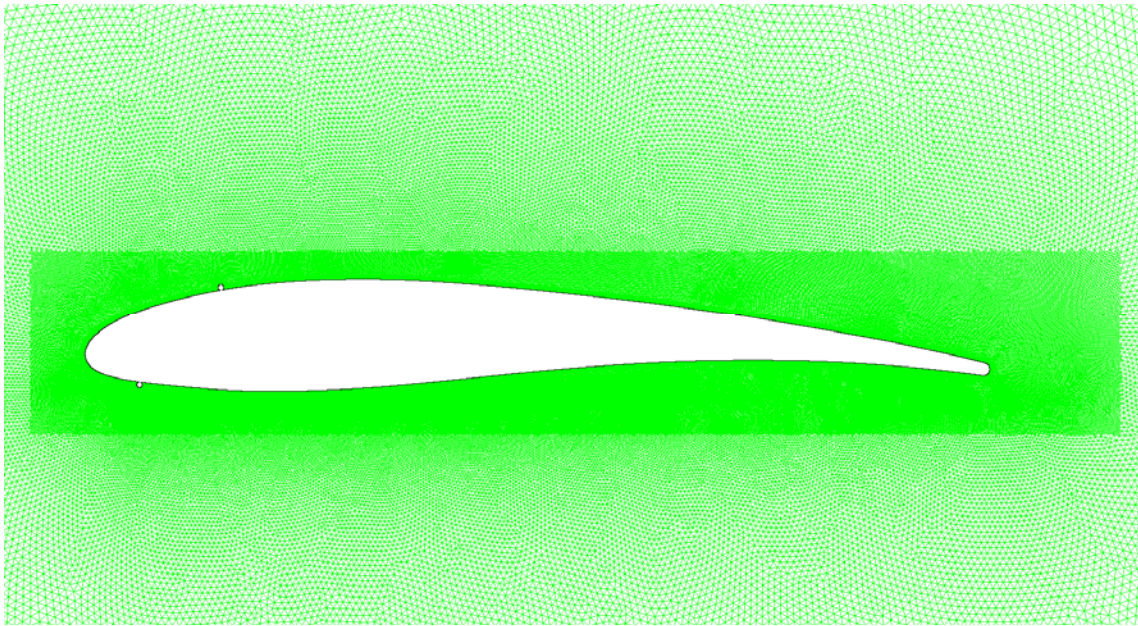


**Figure 3.19** Two-dimensional mesh of tip simulation featuring 0.315 mm trip wires at desired transition locations

Comparing the skin friction coefficients between trip wire solution and the full-scale tip solution delivers promising results. In Figure 3.21 the comparison is made between the skin friction factors of the full-scale numerical solution and the scaled solution featuring the trip wire. The positions of the trip wires are signified by the spikes in skin friction coefficient (skin friction factor values reach about 0.02 at the wires). As with the hub simulations, immediately after the trip wires a small low-pressure recirculation zone is created due to the flow passing over the trip wires. The recirculating flow causes a local increase in the shear stress which in turn leads to increased skin friction coefficients. The flow appears to reattach to the profile which is marked by the decrease in skin friction coefficient, however, the increased Reynolds number and trip wire disturbances appears to be sufficient to induce transition and immediately after reattachment, the skin friction increases sharply. This behaviour is not present in the original scaled solution and actually follows the full-scale plot closely (shape) for the latter half of the plot.



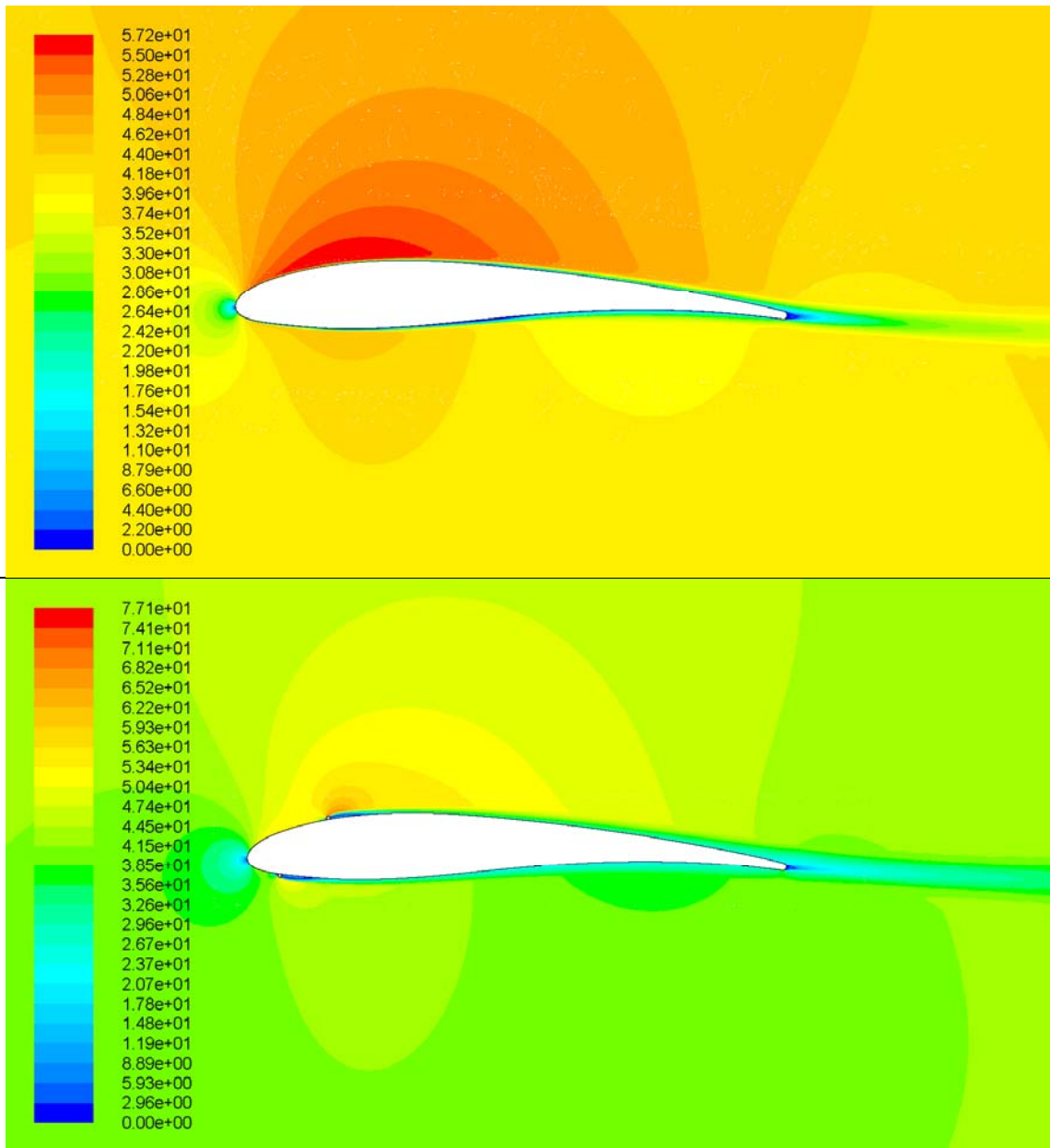


**Figure 3.20** Comparison of velocity magnitude distribution between fine solution (top) and 0.315 mm trip wire solution (bottom) at tip

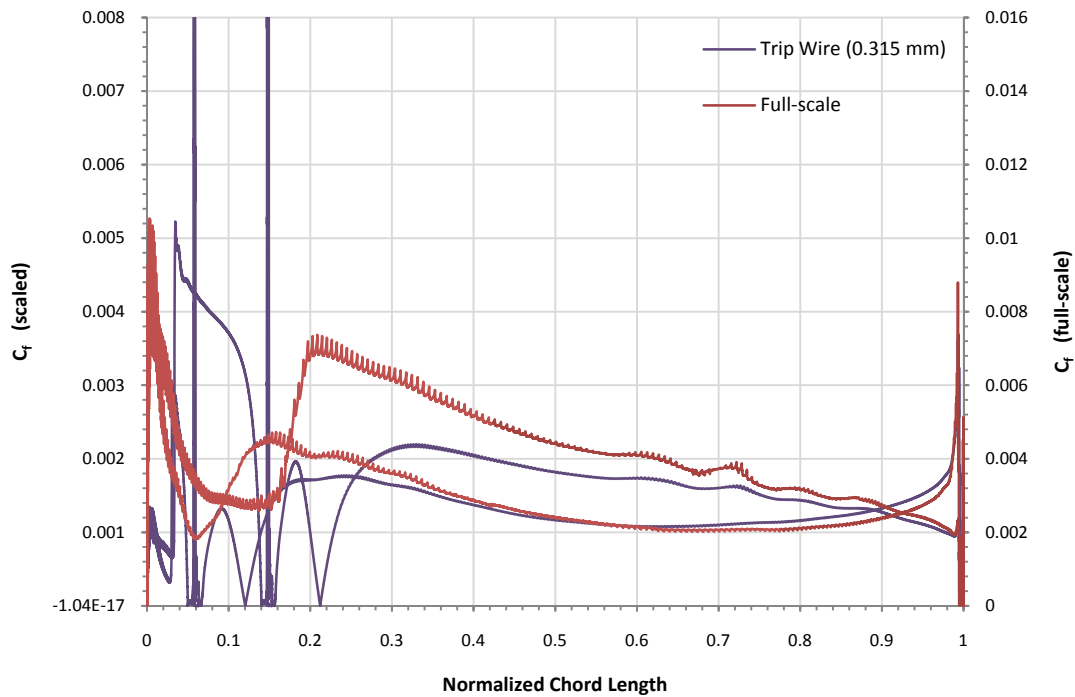


**Figure 3.21**  $C_f$  comparison for tip solutions of scaled induced transition (at trip wire, 0.315 mm trip wire) and full-scale problems

From this it is possible to deduce that, according to a CFD solution of flow over a blade profile featuring a trip wire, the correlation set forth by Gibbings (1959) for flat-plate flow transition, is a fairly good approximation for determining the size and/or position of a trip wire to induce transition almost immediately after the element. However, the Reynolds number range suggested by Gibbings needs to be re-evaluated for application of flat-plate transition models to blade profiles. To this end, the hub simulation was rerun while incrementally increasing the freestream velocity in order to determine the wire thickness based Reynolds number where the correlation by Tani & Sato (1956) started showing the first signs of boundary layer transition. In Figure 3.22 the skin friction coefficient for the simulation of the hub featuring a trip wire at normal operating conditions (10.673 m/s) is compared to the solution obtained by increasing the freestream velocity to 15 m/s. The first thing to notice is that the reattachment of the flow to the profile occurs slightly earlier for the increased freestream velocity. Also obvious is the constantly higher skin friction coefficient for the flow along the lower half of the profile, but perhaps more significant is the erratic behaviour of the skin friction coefficient for the last third of the upper half of the profile. This behaviour is characteristic of flow in the region of transition between laminar and fully turbulent flow. Although transition does not occur at the

desired location (at approximately 40 % of the chord length), the effectiveness of the trip wire does appear to have increased with the increase in Reynolds number.

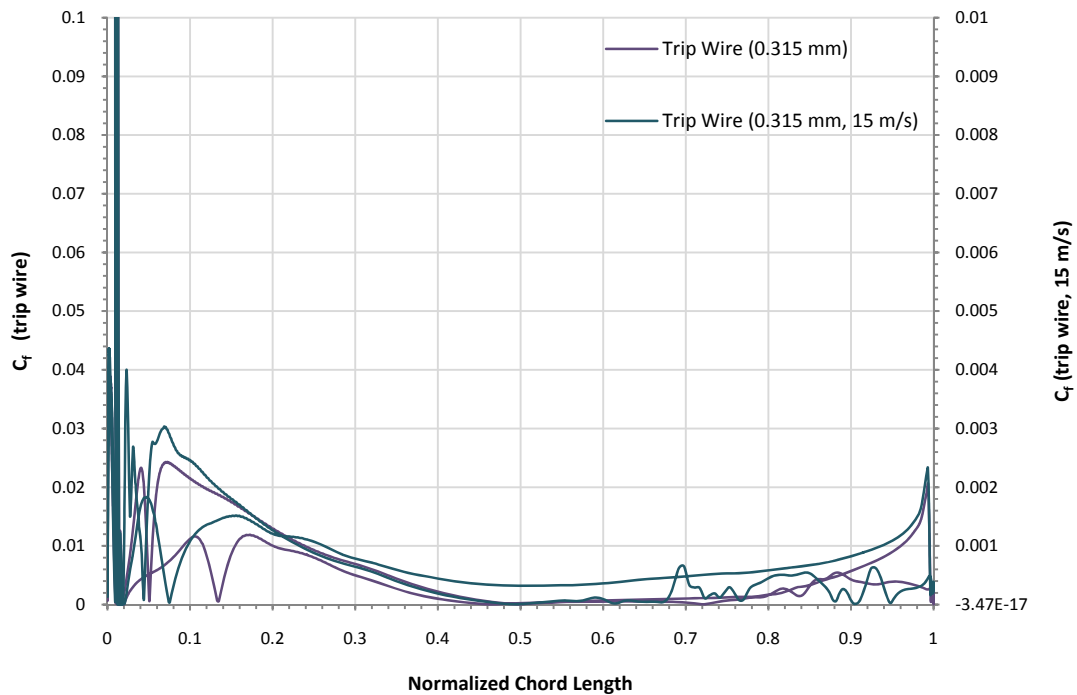


**Figure 3.22**  $C_f$  comparison for hub solutions of scaled fan for 0.315 mm trip wire for normal operation and for 15 m/s operation

### 3.5 EXPERIMENTAL INDUCED TRANSITION EVALUATION

The numerical evaluation did reveal some insight into how flat plate transition theory behaves on curved surfaces with specific reference to blade profiles. Despite the advances made with the Transition-SST model, the CFD code is not able to solve the boundary layer in all its complicated and unpredictable behaviour explicitly. It is therefore considered good practise to perform an experimental evaluation of the performance of the two-dimensional trip element. In this investigation though, the full three-dimensional fan with all its blades featuring trip wires was not numerically modelled and there is no direct comparison between the results obtained from the experiment and the numerical evaluation. Accordingly, for the experimental trip wire evaluation it is assumed that the correlations by Gibbings (1959) and

Tani & Sato (1956) will hold true and that the numerical evaluation was aimed at correctly positioning the appropriately sized trip wires.

A detailed description and schematic of the experimental setup for single tunnel testing can be found in Section 4.2.

The testing methodology for determining the efficacy of the trip wire is relatively simple. Using the setup and procedure described in Section 4.3, a performance curve for the N fan was obtained without the implementation of the trip wire. The blade angle was set to obtain the design point for the B fan, with the design point representing the scaled down equivalent of the operating point of the full-scale 9216 mm fans. This curve was measured twice in order to ensure repeatability and identify potential anomalies.



**Figure 3.23** Trip wire (0.3 mm fishing line) 'painted' to blade surface

The trip wires were then stuck to the fan blades, leaving the blade angle unchanged. The SWG30 wire could not be obtained, and was substituted with 0.3 mm fishing line. The 0.015 mm difference in thickness was deemed negligible. The fishing line was 'painted' to the blade surface using clear nail varnish. The nail varnish dries to a smooth finish that should make up for the 0.015 mm difference in thickness. It also allows easy removal of the line but is still

strong enough to prevent it coming loose, and the residue can be easily removed from the blade surface using acetone and a cloth. Figure 3.23 shows the trip wire on the bottom surface of the blade. Also note that the trip wire position is interpolated linearly between the tip and hub profiles.

Once the trip wire was applied to the blade surface, a second set of tests were conducted in an identical fashion to the 'reference' tests. Again, two performance curves were obtained to gauge repeatability and potential anomalies. It was expected that the fan static pressure rise performance curves would follow closely on the reference no-trip curves, but that the turbulent boundary layer will delay flow separation and thus delay the onset of stall (see Section 4.3 for more detailed explanation). The comparative fan static pressure rise curves can be seen in Figure 3.24 (NT denotes 'non-tripped', and T denotes 'tripped'). It is assumed that the trip wires are effective in inducing turbulent boundary layers on both the upper and lower surfaces of the blades.

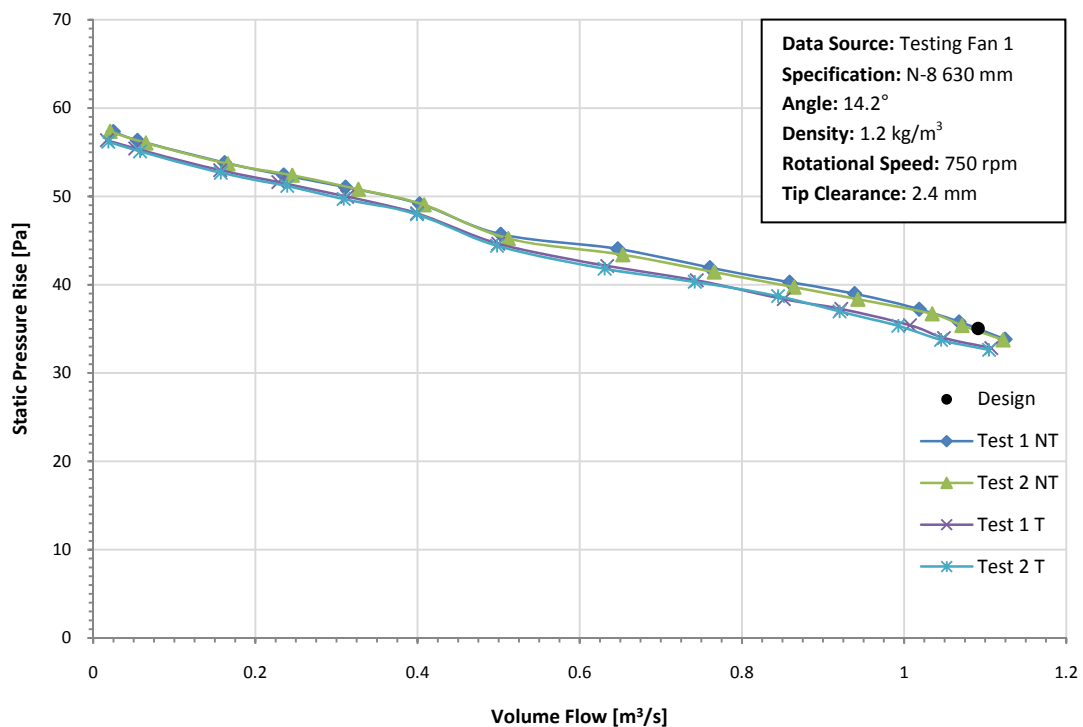


**Figure 3.24** Effect of two-dimensional roughness element (0.3 mm trip wire) on fan static pressure rise (fan 1, identical blade angle)

Immediately obvious is the decrease in fan static pressure performance. The decrease in performance, although greater than expected, can be attributed to the turbulent boundary

layer. The chaotic behaviour of turbulent flow causes the blade profile to perform slightly worse, resulting in a lower lift coefficient,  $C_L$ , and increased drag coefficient,  $C_D$ , and subsequently, lower fan static pressure performance (Colman et al., 2008). The stall region on the non-tripped performance curves is identified by the plateau at approximately  $0.6 \text{ m}^3/\text{s}$ . In this stall region the relative flow angle is too great separation occurs on the blade surface, leading to a decrease in performance. As expected, the turbulent, tripped performance curve does not exhibit this same behaviour and instead it is observed that static pressure performance curve only shows a minute levelling off at about  $0.4 \text{ m}^3/\text{s}$ . It is however not overly clear whether the effect of stall is decreased or whether the onset of stall is completely mitigated, but the performance difference before stall appears to remain constant at 5 % and after stall this deficit decreases to 2 %.

In order to better evaluate the need for trip wire testing on scaled fan arrays, an additional trip wire experiment was performed. In this case, the N fan paired to Tunnel 3 was fitted with trip wires using the same process described previously. However, for this experiment the blade angle was increased in order to obtain the desired design point. The trip wires did not allow the use of the N fan blade angle jig to set the blade angles and thus there is no accurate knowledge of what the exact final blade angle was or whether all the blades were set to the same blade angle. It is however reasonable to assume that the mean blade angle is greater than  $15^\circ$  and that the difference in blade angles is less than  $1^\circ$ . The comparative fan static pressure rise performance curves can be seen in Figure 3.25 along with the fan power curve in Figure 3.26. The static pressure performance curve of the tripped boundary layer bears some resemblance to the behaviour of fan 1 in Figure 3.24 in that it performs comparably with the non-tripped fans up to the point of stall (for decreasing flow rates) and then performs identically at lower volume flow rates. A slight difference in the gradient for  $0.6 \text{ m}^3/\text{s}$  and greater flow rates suggest that the induced turbulent boundary layer does have some behavioural impact on the performance but even at the point of greatest difference ( $\sim 0.7 \text{ m}^3/\text{s}$ ), this behaviour results in only a 2 % difference. The power curve in Figure 3.26 does not yield anything surprising. The increased surface shear stress caused by the trip wire and the induced turbulent boundary layer leads to an increase in skin friction drag and subsequently a directly proportional increase in the shaft power.

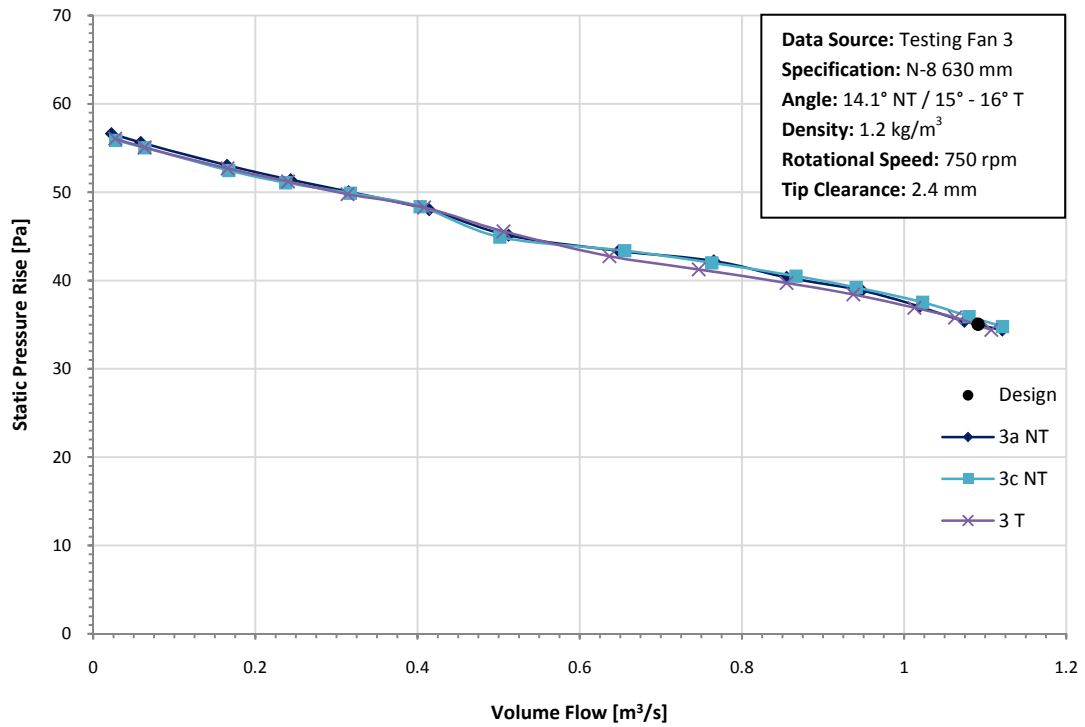


Figure 3.25 Effect of two-dimensional roughness element (0.3 mm trip wire) on fan static pressure rise (fan 3, increased blade angle)

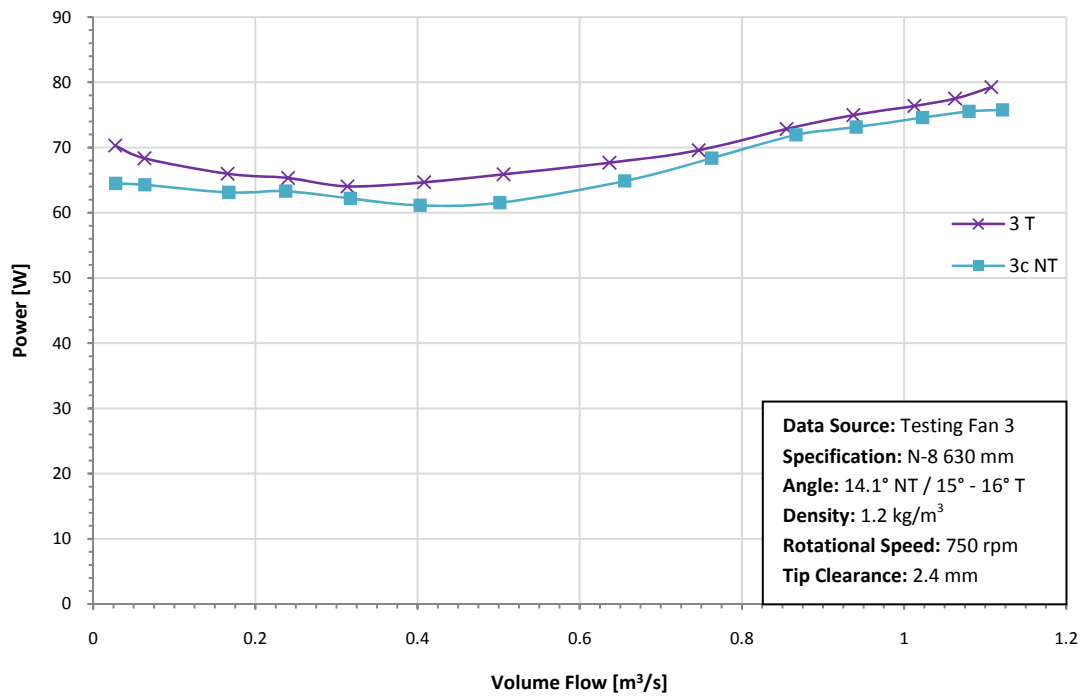


Figure 3.26 Effect of two-dimensional roughness element (0.3 mm trip wire) on fan power (fan 3, increased blade angle)

### 3.6 CONCLUSION

Without the development of the Transition-SST turbulence model in Fluent 12 this Reynolds number investigation would not have been possible. The use of the transition model allowed solving for positions of natural transition onset on the full-scale fan blade profiles and thus provided the information critical to this Reynolds number investigation. Since the Transition-SST model was verified using turbomachinery (Langtry et al., 2006), it is also perfectly suited to this type of problem. It is important to note that the CFD solutions obtained were used as guides for positioning of the trip wires and does not represent the flow around a fan blade of this profile. A far more extensive – most likely a 3D model – will need to be conducted in order to obtain the exact flow solution.

For the full-scale blade profile, it was found that the turbulent transition on the upper and lower surfaces for the hub simulation occurs at almost identical positions at about 36 % of the chord length. According to calculations,  $Re_l$  for the hub is in the transition range but with the inclusion of surface roughness and freestream turbulence in the simulation, the boundary layer transition occurs earlier than predicted. The higher velocity of the incoming flow for the tip simulation leads to boundary layer transition very early on the blade surface. However, despite operating at greater flow velocities across the upper surface of the blade profile for the tip simulation, transition occurs later than it does for the lower surface. The flow accelerates up to the apex of the upper surface, leading to a thinner boundary layer and delaying boundary layer development, as visualised in Figure 3.27. It is very important to note that this phenomenon only revealed itself after mesh refinement along the profile and the tail (immediate wake). An important lesson to take from this is that sufficient wake mesh refinement is critical to obtaining a grid independent solution.



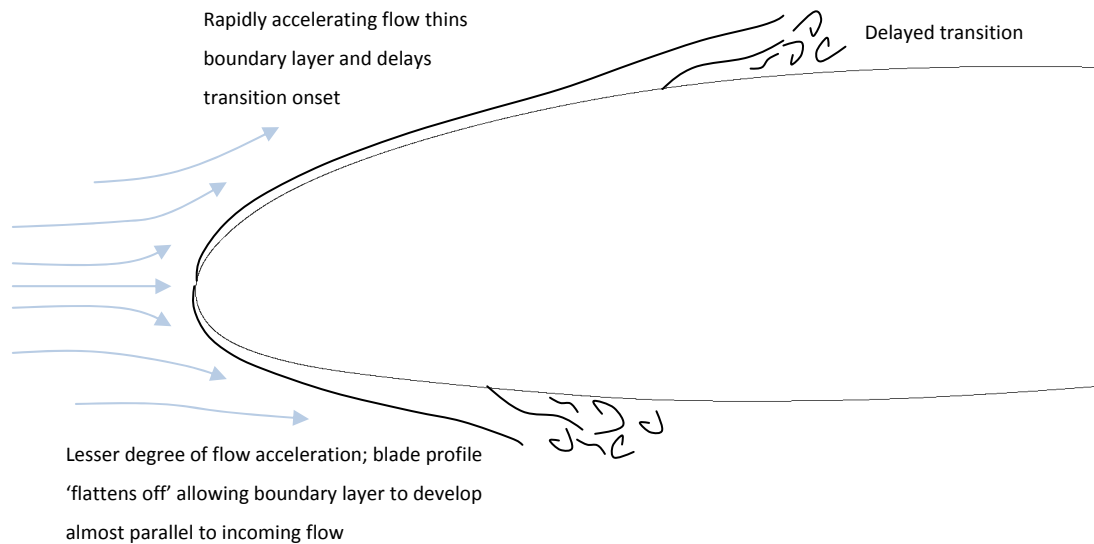


**Figure 3.27** Visualisation of delayed boundary layer transition

In order to induce boundary layer transition on the scaled fan blades, two-dimensional roughness elements were selected based on the simplicity and ease with which these elements can be implemented. Although not as effective as three-dimensional roughness elements at high Reynolds numbers, they are well suited to lower Reynolds numbers applications (Gibbings, 1959). The specification of the size and the position of the trip wires were done using a 'hybrid' of the 'transition at the wire' formulation by Gibbings, and a 'transition downstream of the wire' model by Tani & Sato. The motivation for the use of these two models relied partially on the assumption that the flow condition over the blade can be interpolated linearly between the hub and the tip, and partially on their effectiveness at predicting transition in flat plate testing (Gibbings, 1959). The initial iteration of specifying transition wire thickness was aimed at inducing transition at the wires for both the hub and the tip, but the size of the required trip wire to induce this transition at the hub was too thick and would have had a significant effect on the aerodynamics of the blade. It is thus worth noting that for lower chord based Reynolds numbers (less than 100 000) transition-at-the-wire is not a feasible option for this type of problem as the required trip wire diameter is just too large.

Verifying the placement and size of the trip wires using the same Transition-SST turbulence model revealed mixed results. The model managed to predict the induced transition effect of the trip wire on the boundary layer for the tip simulation, but revealed that the trip wire is

completely ineffective when placed near the leading edge at the hub of the blade. Although the Transition-SST model has been verified using turbomachinery, none of the verification cases included boundary layer disruption (Langtry et al., 2006). The lack of transition at the hub could thus possibly be explained by the inability of the Transition-SST near-wall simplifications to capture the full disruption effects of the trip wire. Another possible explanation might be that the placement of the trip wire at the leading edge (less than 1.4 mm from the leading edge) combined with the thin, still developing displacement layer and the low Reynolds number is merely not enough to allow boundary layer transition to occur. As mentioned previously, the accelerating flow over and under the blade profile has been seen to delay boundary layer development and could just as easily dampen any disruptions the trip wires may induce. It is suggested that the possibility of a better suited trip wire position Reynolds number range be investigated to allow flat plate trip wire theory to be more effectively applied to curved surfaces (with emphasis on blade profiles).

For all numerical evaluations, it was observed that the stability increased, rate of convergence increased and residual values decreased when the  $y^+$  values were reduced to less than 1.5 and the maximum velocity magnitude gradient was reduced to less than 5 m/s. Although the Transition-SST model prescribes a  $y^+$  range of 1 – 5, it is advised to get this value as close to 1 as possible. The use of the skin friction coefficient,  $C_f$ , as used during the verification and evaluation of the Transition-SST model, proved to be a good and reliable indicator of boundary layer transition onset.

The testing methodology for the experimental evaluation of the trip wires is exactly the same as that of the individual performance curves and is explained in more detail in Section 4.3. The first trip wire evaluation was performed using the N fan paired with Tunnel 1 and compared the fan static pressure performance with and without the trip wires present. Without detailed boundary layer evaluation using methods like ‘oil film visualisation’ there is no certainty as to whether boundary layer transition occurs as desired. However, based on the results, it is safe to assume that the trip wires are effective in inducing transition at some point along the blade surfaces. Even if transition is not induced at the hub, it was considered to have a minimal impact on the accuracy of the comparison since very little work is done by the fan in the area near the hub. The margin of comparison ranged from 2 % to 5 % and is therefore comparable with the 4 % decrease in all round performance that Meyer & Kröger (2001) predicted

numerically when the Reynolds number effects are included. It was also noted that the plateau that is depictive of stall was not present, or to much a lesser degree, with the trip wires installed. This can be attributed to the turbulent boundary layer reducing and/or delaying flow separation. However, since the flow does not necessarily follow the 2D behaviour as assumed for the numerical evaluation, it is possible for the trip wires to impede the natural 3D flow across the blades (see Figure 3.28). Without a detailed investigation into the boundary layer there is however not enough information to make a conclusion.

The second trip wire experiment was performed using the N fan paired to Tunnel 3. The aim of this experiment was to determine how the fan performance curves compare when the blade angle was increased to obtain the same design point when the trip wires were installed. Again, the plateau that represents stall is not as discernable as on the fan static pressure performance curve of the non-tripped fan. Despite the small deviation in gradients for higher flow rates, the fans compare favourably. Thus, according to these two trip wire experiments at least, the Reynolds number effects do not influence the response of the fan in any significant way and may be ignored providing the blade angles are set up to obtain the correct fan static pressure performance.

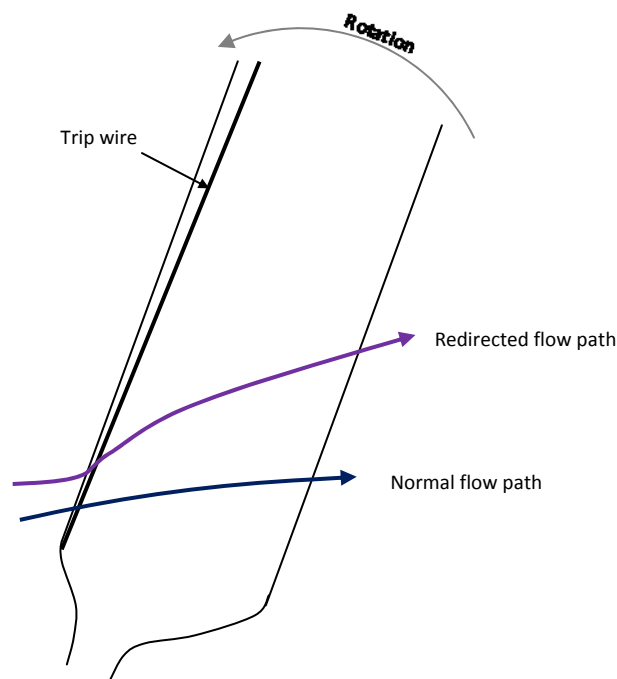


**Figure 3.28** Influence of trip wire on flow path over fan blade

## **4 EMPIRICAL FAN COMPARISON**

This chapter focuses on the testing done using 630 mm diameter fans of varying designs in order to determine the relative performance under distorted inflow conditions and how this compares to previous empirical results.

### **4.1 INTRODUCTION AND OBJECTIVES**

First and foremost, the objective of the testing was to perform all experimentation and data collection in an accurate and reliable manner. To this end, testing procedures and measurement processes from previous investigations in this field – Visser (1990) and van der Spuy (1997) – were investigated and used as basis to formulate a testing procedure for this investigation. The prevailing difference from previous investigations is the advances made in technology pertaining to the measurement of flow and pressures as well as the means in which this data is captured.

Before any testing could be done, it was necessary to determine the appropriate reference fan. The acquisition of additional funding allowed the manufacturing of scaled versions of the fans used in typical large-scale fan arrays in South Africa (from this point forward referred to as the N fan) and thus provide this investigation with the best possible reference fan (see Appendix B for performance data on the full scale N-Fan). The fans were manufactured using an injection moulding process with moulds created from a rapid prototyped master fan blade. The blades for all three fans (24 in total) were manufactured by Skeg Product Development in Milnerton. A simple, clamp-style scale-accurate hub ( $\varnothing 95$  mm) was machined in-house from 6082 Aluminium in the Mechanical Department workshop. The scale N fan can be seen in Figure 4.1 installed in one of the test tunnels. These fans allow this investigation to meet the objectives for this investigation as a whole, which is to provide the best possible performance comparison between a scaled representation of a large-scale fan-array, and the real-world performance of such an array. In addition, this investigation aims to develop a platform with which new or modified axial flow fan designs for large-scale fan arrays can be tested on a more manageable and measureable scale of which the performance is comparable to the performance that can be expected from these designs in full scale operation.

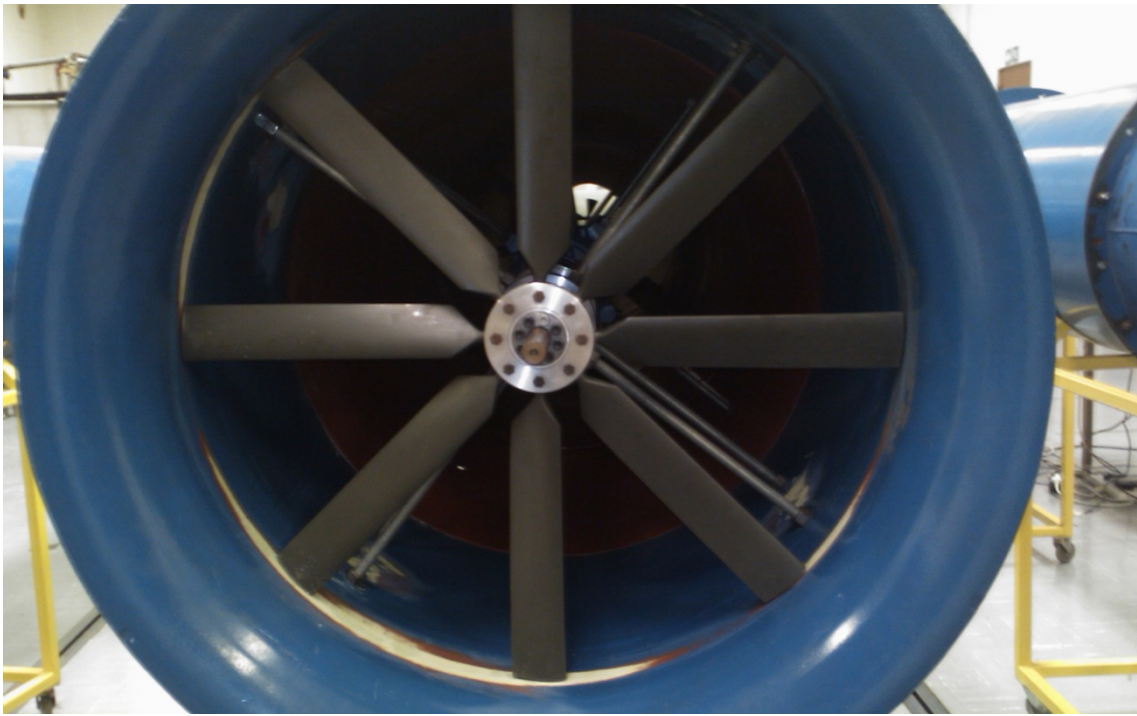


**Figure 4.1** Scale N fan installed in test tunnel

The B fan was designed by Bruneau (1994) as a bolt-in replacement for the N fan with specific emphasis on use as an edge fan. Bruneau performed his verification testing using a 1.542 mm fan (see Appendix B for performance data) and thus for this investigation a scaled fan had to be manufactured. The scale model was created using the same profile data used by Bruneau. However, Bruneau had trouble sealing the roots of his fan since the blades had square roots and the hub of the fan was cylindrical. This was taken into account when designing the scaled blades and hub and was solved by projecting the root of the blade onto a cylinder, allowing it to follow the hub contour. The hub was designed to have a spherical circumference which allows the blade to seal on the hub irrespective of blade angle. Ideally the blade root would also be designed as a spherical fit to create a perfect seal on the hub, but this would have been very hard to manufacture. The blades for the B fan were machined on a 5-axis CNC milling machine from 6082 Aluminium. The hub was machined in-house by the Mechanical Department workshop. The setting hole and groove for attaching the blade and setting the blade angle was machined using a 3-axis milling with a 4<sup>th</sup> axis table which allows rotary movement of a job. The B fan can be seen in Figure 4.2 installed in the edge test tunnel.

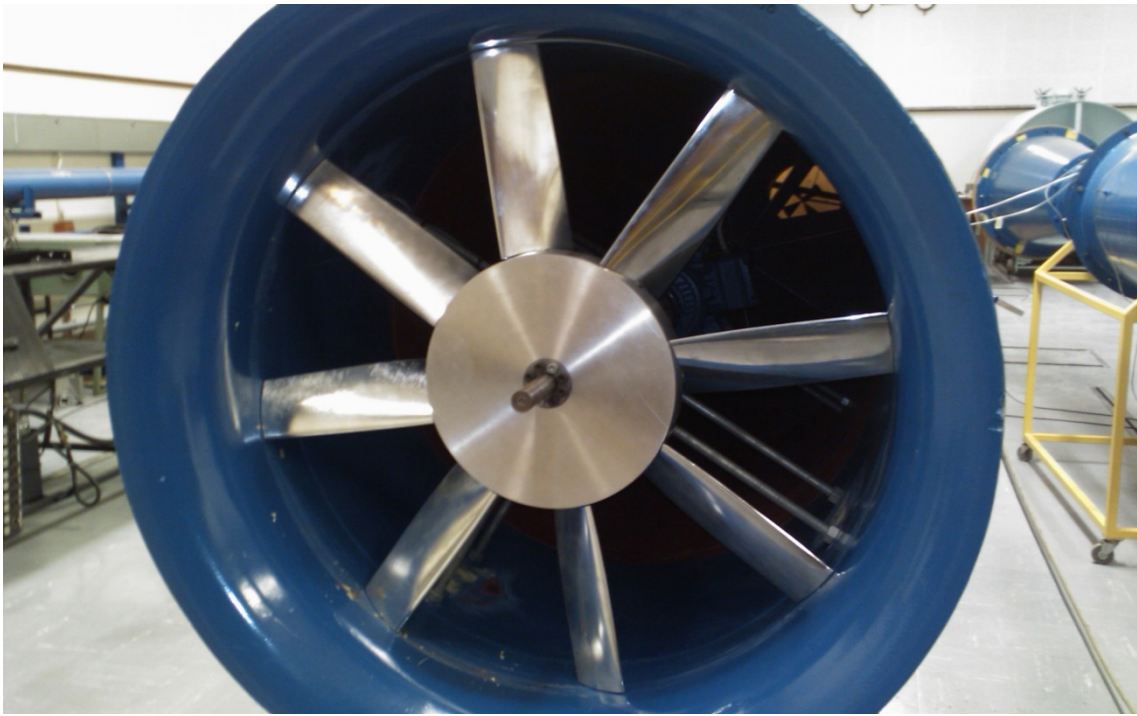


**Figure 4.2** Scale B fan installed in edge test tunnel (fan 3)

The work by Visser (1990) formed the basis for all the scaled fan array work. For his research he set up a fan array using six 630 mm fans positioned side by side in order to create a single 'bay' as found in some full-scale installation. Visser (1990) and Salta & Kröger (1995) experimental work was based on the assumption that the flow does not cross this bay as each bay operates as an entity in a collective. Figure 4.3 illustrates a typical 6-row full-scale cooling fan array and indicates how a bay is defined (red dashed lines). The bay highlighted in blue (6 fan rows) illustrates how Visser and Salta & Kröger's setups related to full-scale installation. However, when ignoring the effects of obstructions in close proximity to the array (buildings for example), the flow entering the bay is effectively symmetric about a plane in the middle of bay (between fan 3 and 4 in this case). This means that a six row array might be represented by a three row scaled setup for example. Accordingly, by closing off the one inlet to his scaled bay, Visser effectively recreated a 12 row bay. Since the typical fan installation in South Africa features only six rows, this investigation chose to focus on recreating a six row fan bay using only three scaled fans (marked in green on Figure 4.3).

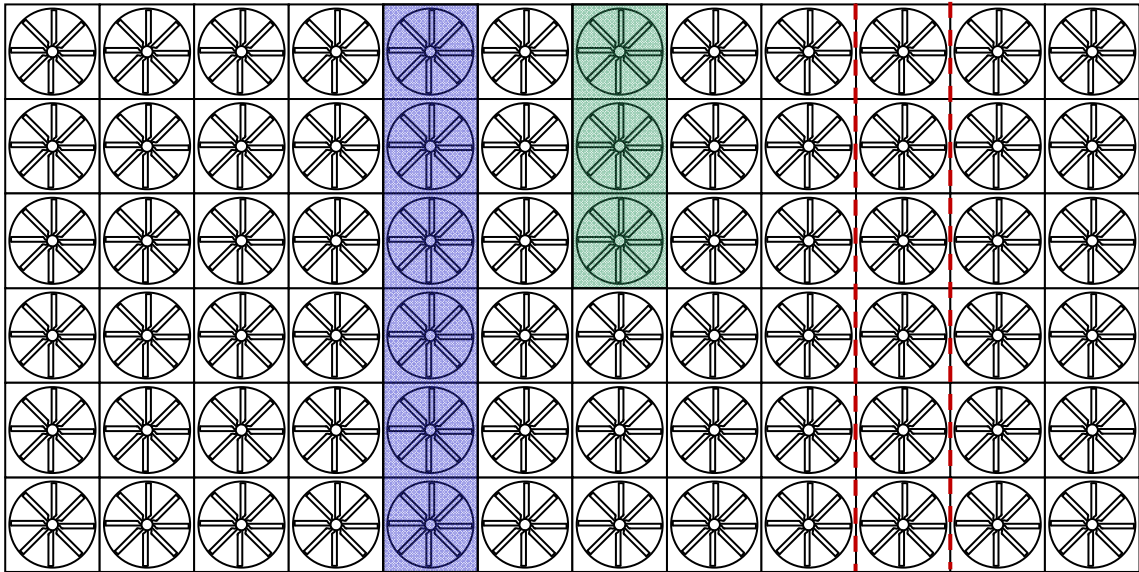


Figure 4.3 Typical large-scale fan array illustrating different experimental representations

Using a similar setup to Visser, Salta & Kröger not only looked at the effects of increased or decreased fan rows, but also formulated a correlation for how these fans will perform (volumetric effectiveness) based on the height of the fan platform above the ground. Salta & Kröger (1995) derived a model that predicts the effect of platform height on system volumetric effectiveness. This model will be put to test using different types of fans. Salta's model is visualized in Figure 4.4 and the correlations that define the model are given in Equation 4.1 and Equation 4.2.

For a single fan:

$$\frac{V}{V_{id}} = 0.985 - e^{(-X)} \quad (4.1)$$

with  $X = 4.882H_i / d_f$

For multiple fans:

$$\frac{V}{V_{id}} = 0.985 - e^{(-X)} \quad (4.2)$$

with  $X = \frac{(1 + 45/n_f)H_i}{6.35d_f}$  and  $n_f$  the number of simulated fans

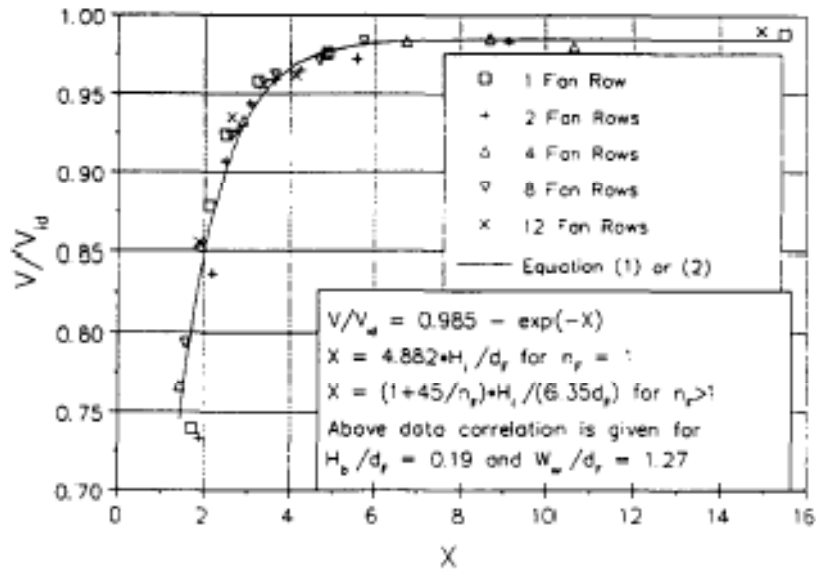


Figure 4.4 System volumetric effectiveness for ACHEs having 1, 2, 4, 8 and 12 fan rows (Salta & Kröger, 1995)

The correlations express the system performance as a ‘volumetric effectiveness’ which compares the current system performance to the ideal system performance, i.e. when all fans operate at the design point. The ideal system performance,  $V_{id}$ , is obtained by multiplying the design performance for an individual fan by the number of simulated fans (three tested fans simulate the behaviour of six fans with the use of symmetry planes).

In conclusion, the objectives for the experimental work in this chapter is to firstly obtain reference performance curves (fan static performance) for the model N fans and B fan to ensure that the design parameters (as defined by Bruneau (1994) for his design of the B fan) are met, to secondly evaluate the B fan as a replacement fan specifically as the edge fan in an array, and to lastly confirm whether the model devised by Salta holds for alternative fan types than was used to obtain the original model.

## 4.2 EXPERIMENTAL SETUP

The experimental setup is similar to the setup used by Visser (1990) except that instead of six fans, this setup uses three fans. Since this investigation is intended as a non-specific investigation, the effects of nearby buildings and obstructions that are often experienced in these types of fan arrays will not be replicated on the scale experimental setup. Figure 4.3



shows a typical large-scale fan array and illustrates the differences in scaled replicas between Visser’s investigation and this investigation. Visser had six BS848 Type B tunnels at his disposal, however, since the flow is effectively symmetric about the middle (fan 1 and fan 6 see identical inlet disturbances), this investigation used only three tunnels and defined all the walls as symmetry planes.

The tunnels themselves are modified versions of what Visser and Salta used for their investigations and were all constructed according to BS848 standards. Key improvements to the tunnels include up-rated motors, moving the motors further down the tunnel in order to accommodate a torque transducer in the edge fan tunnel (other tunnel motors were also moved to keep tunnels identical), quick-swap fan fixtures, anemometers to measure flow (Visser used the venturi of the tunnel while Salta installed the anemometers currently in use), new pressure transducers and new throttles for obtaining performance curves and desired operational points. The full list of equipment and instrumentation can be found in Table 4.1. The colour coding in Table 4.1 indicate instruments or equipment that function as a unit, for example, the power supplies are used to power the pressure transducers, likewise, the motors are controlled by the drive controller.

**Table 4.1** Equipment and Instrumentation

<b>Component</b>	<b>Description</b>	<b>Quantity</b>
Motor	WEG 3Ø pad mounted 750 W	3
Drive Control	Mitsubishi E700 5.5 kW	1
Power Supply	Rhomberg Electronics Slimline SC-900 230 VAC / 24 VDC ,0.3 A	2
Pressure Transducer	AutoTran Incorporated 860-X-A-18-2-P 0 – 1000 Pa / 1 – 10 V	10
Data Acquisition Unit	National Instruments NI USB-6218	1
Anemometer	WeatherTronics Propeller Anemometer Model #0207	3
Torque Transducer	Hottinger Baldwin Messtechnik GmbH T22/100Nm #80709520	1

\*colours indicate instruments or equipment that functions as a unit

As mentioned previously, the tunnels themselves are almost identical to the tunnels used by Visser and Salta. A detailed schematic of the modified individual tunnels can be seen in Figure 4.5.

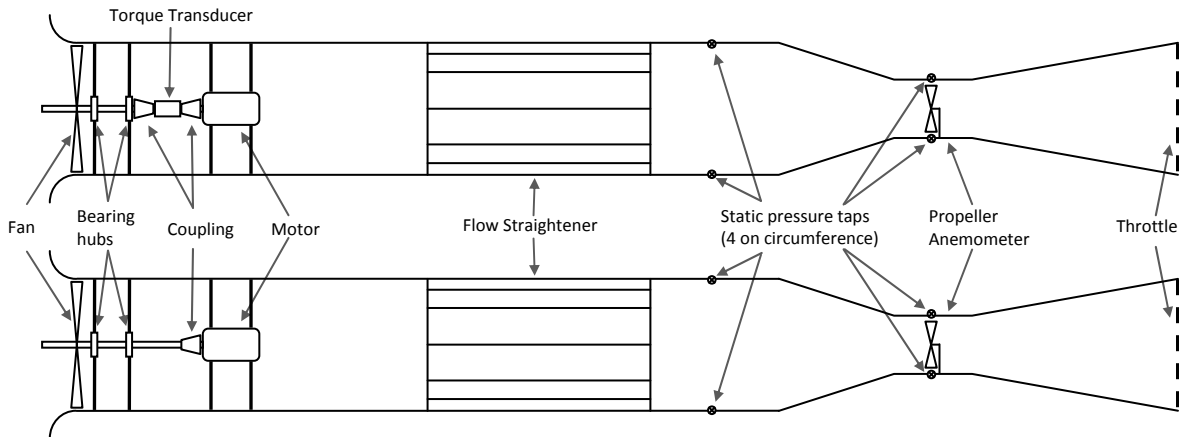


**Figure 4.5** Schematic of edge and inner individual tunnels (top → edge fan, bottom → inner fans)

Two different types of throttles were used depending on the type of testing done. For determining the performance curve of the fan, an overlapping disc throttle was designed and manufactured. The throttle, as seen in Figure 4.6, is very quick to set and allows for good repeatability. Only one disc throttle is available though and thus, when testing the performance of the array, a perforated plate is used to obtain the desired operational performance of the individual fans.



**Figure 4.6** Overlapping disc throttle

By closing or opening the holes in the plate, it is possible to shift the operational point up or down the performance curve. The perforated plate, as seen in Figure 4.7, also allows for a more evenly distributed obstruction which better resembles the flow resistance in a full-scale installation.

The purpose of the individual fan tests is to determine the correct blade angle at which the design point can be obtained. This also serves as the reference by which to evaluate the volumetric effectiveness of the individual fans and the system as a whole. For the array tests, the individual test tunnels are assembled into a communal inlet that represents the fan bay and the symmetry plane. A movable 'ground' allows the testing of different 'platform heights'. This movable ground height is critical to recreating the work of Salta. A schematic of the assembled array can be seen in Figure 4.8.

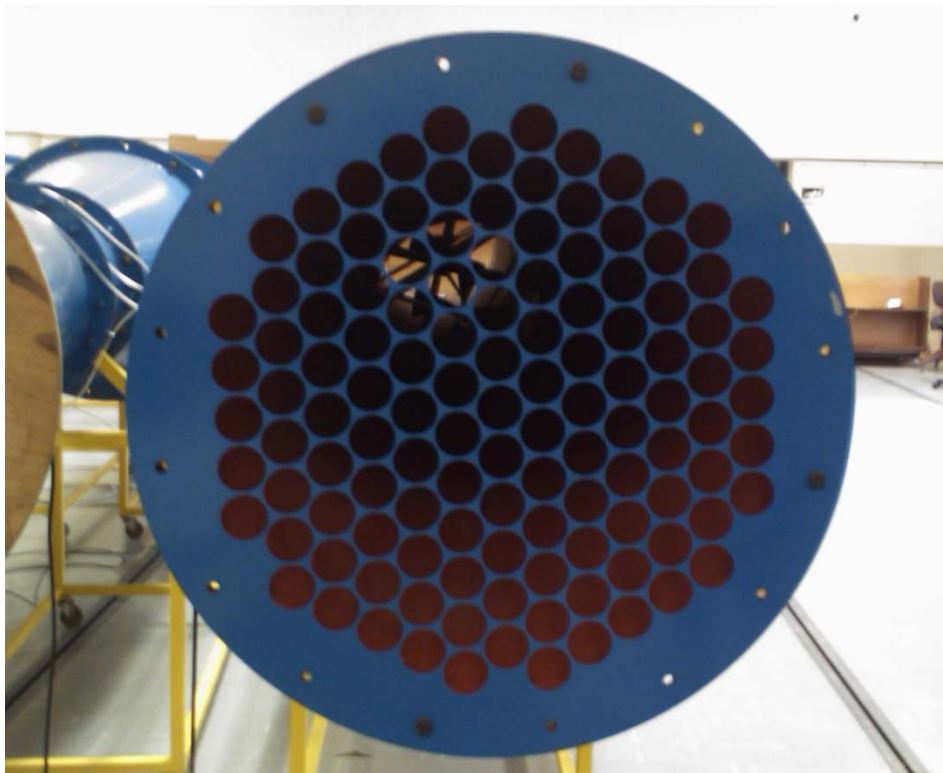


**Figure 4.7** Perforated plate throttle

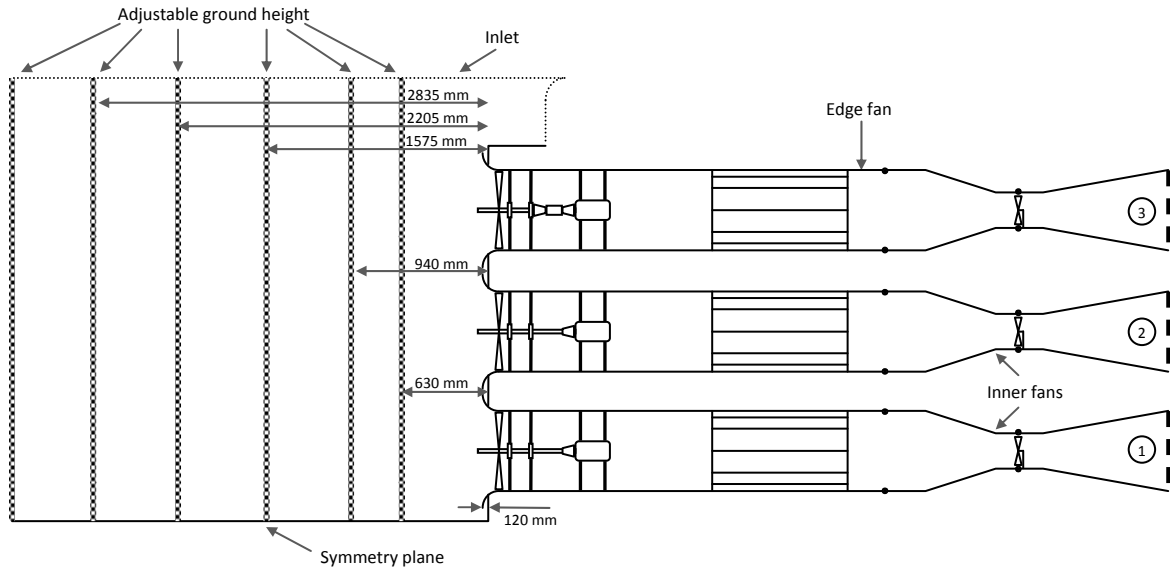


**Figure 4.8** Top view schematic of fan array

The array fan tests are devised to recreate the experiment by Salta & Kröger (1995) but using the N fans and to establish whether the Salta & Kröger correlation for multi-fan arrays, as given in Equation 4.2, holds for different fan types. After having completed the evaluation using N fans in all three tunnels (N-N-N configuration), the experiment will be repeated with the newly manufactured B fan as the edge fan (N-N-B configuration). These two configurations can be seen in Figure 4.9 and Figure 4.10.



**Figure 4.9** Fan array in N-N-N configuration

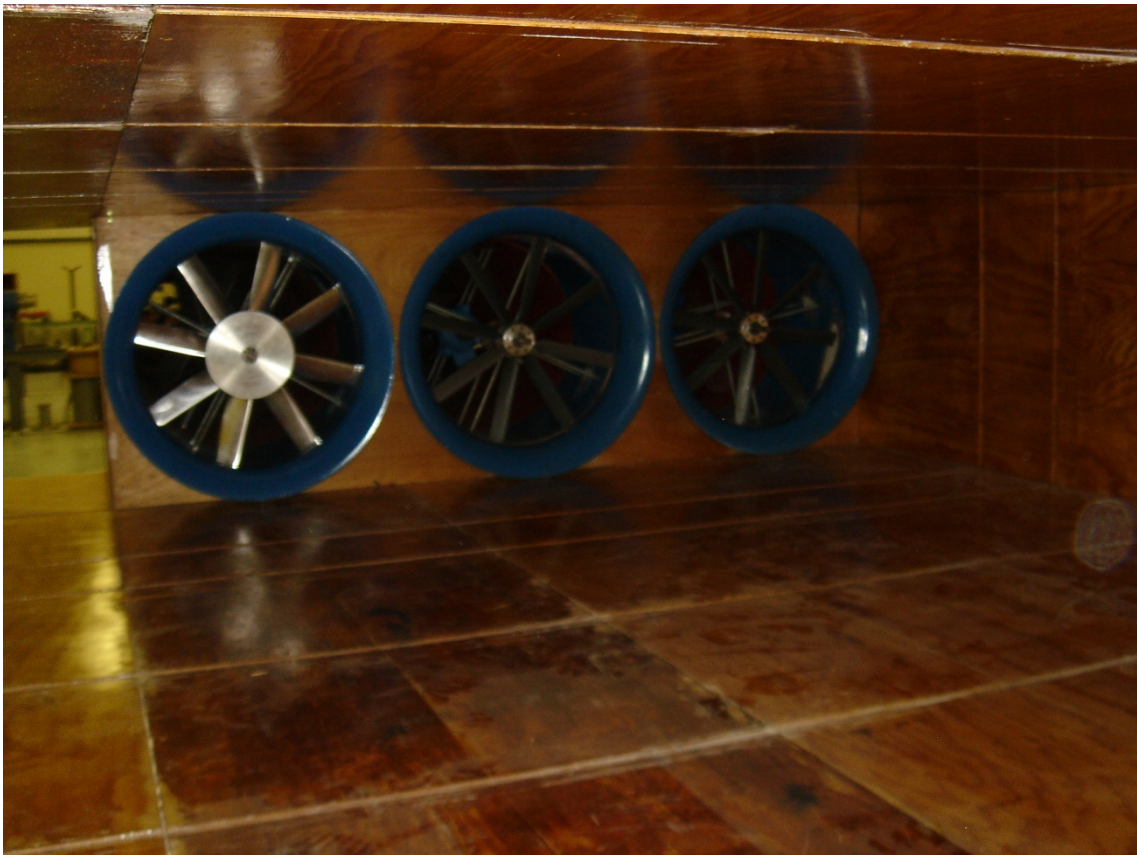


**Figure 4.10** Fan array in N-N-B configuration

For the N-N-B configuration the Salta & Kruger correlation is not expected to hold since the array now features a mixed fan configuration. The final objective of the fan array testing is to compare the N-N-N performance to the N-N-B performance and determine whether the B fan is indeed better suited to perform as an edge fan.

Given the specific way in which the N fan blade and B fan blade angles are defined, a simple blade angle jig was designed for both types of fans. The jigs were designed from the original CAD drawings and were laser cut from stainless steel. Both jigs feature a flat surface which is parallel to the defined datum by which either fan's blade angles are measured. A digital protractor can be placed on top of this flat surface to measure the blade angle with  $0.1^\circ$  accuracy. The N fan blade angle jig can be seen in Figure 4.11 (note that the jig is placed at the top of the blade) and the B fan blade angle jig can be seen in Figure 4.12 (note that the jig is placed at the root of the blade/hub of the fan).

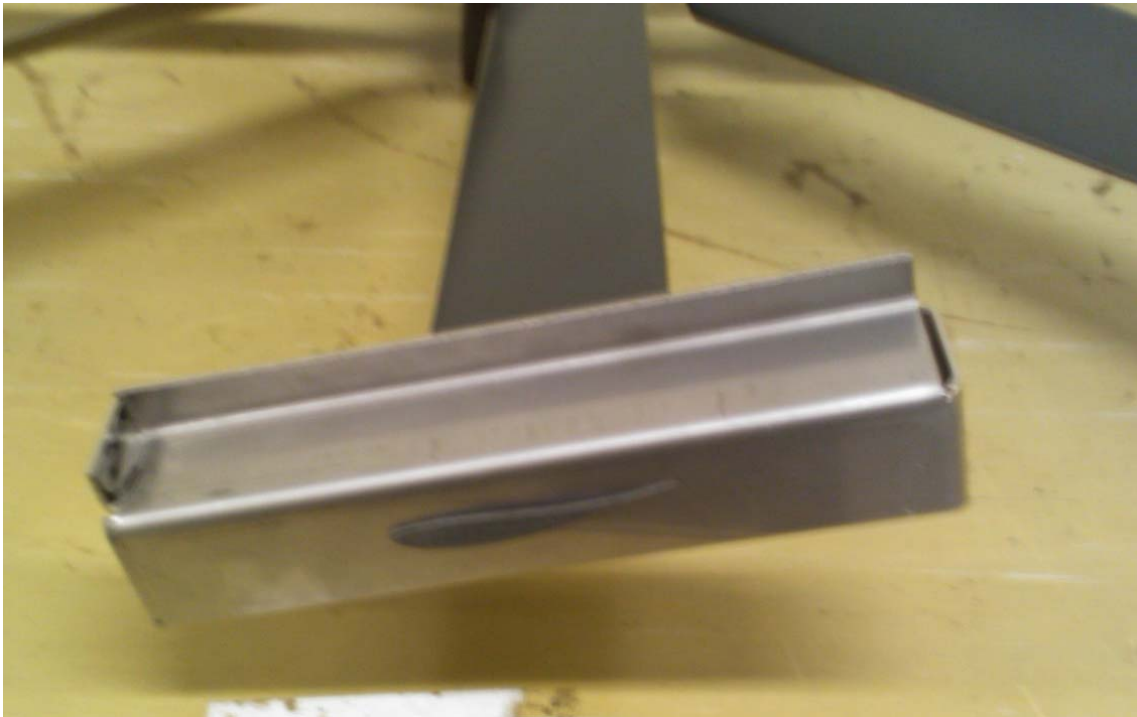


**Figure 4.11** N fan blade angle jig

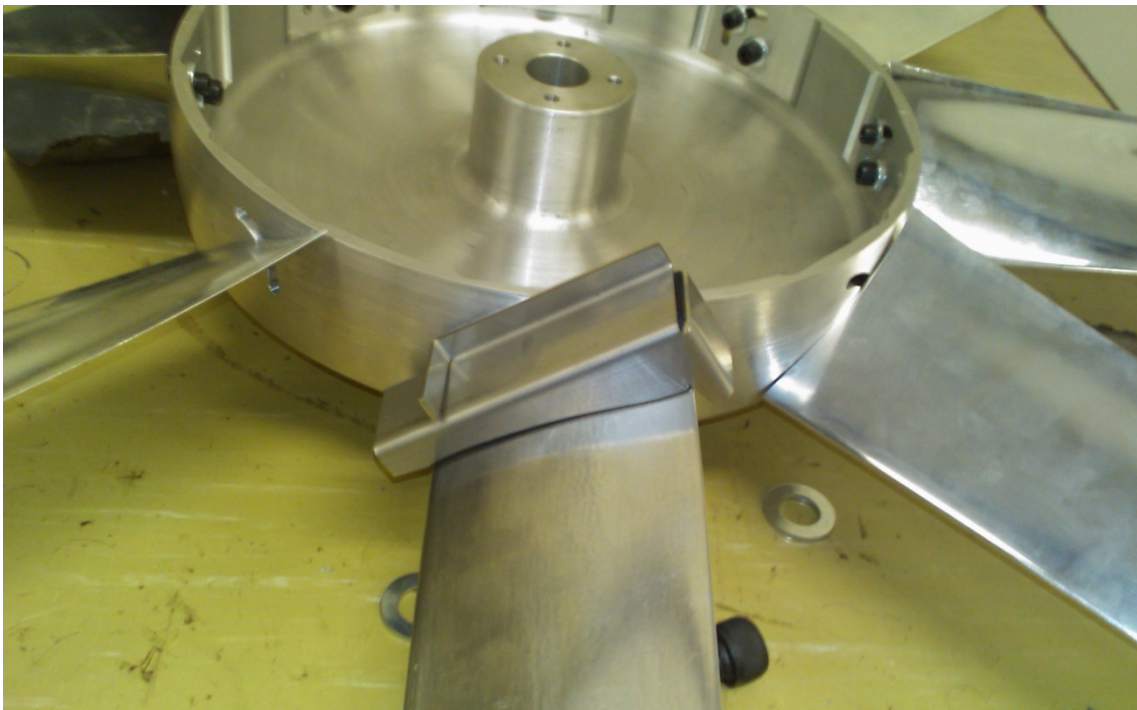


**Figure 4.12** B fan blade angle jig

Apart from different blade angle definitions, the fans themselves are very different. In Figure 4.13 the differences in fan design are apparent. Firstly, the B fan was designed with a 0.4 hub-to-tip ratio, as opposed to the 0.15 of the N fan. Despite having shorter fan blades, it is expected that the B fan will perform better partially due to the greater hub-to-tip ratio as the larger hub and the sealed blade roots will help to prevent the detrimental effects of flow recirculation around the hub area. The N fan features narrower blades than the B fan, resulting in lower solidity, where the fan solidity is a measure of the frontal flow area of the fan that is occupied. Note that the N fan and B fan have different outer diameters, resulting in different tip clearances. The fan diameters were scaled directly from either the full-scale fan (in the case of the N fan) or from the prototype design (in the case of the B fan).

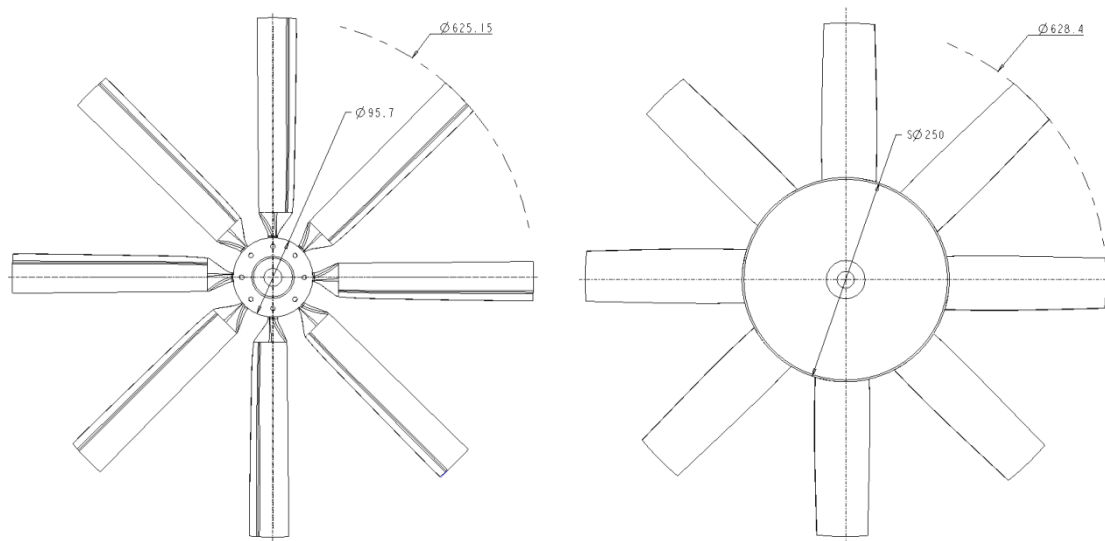


**Figure 4.13** Simple schematic of N fan (left) and B fan (right)

### 4.3 INDIVIDUAL SCALED FAN PERFORMANCE

The testing methodology for individual fan performance testing was devised to provide accuracy, repeatability and good resolution on the performance curves.

Before any readings were taken, the selected fan was run for at least 10 minutes to allow the motors, anemometers and bearings to reach steady state operating temperatures. In order to remain within the calibrated limits of the equipment, 1300 rpm was selected as the speed at which all testing will be done. At this speed, the volume flow rate will not exceed the

calibrated limits of the propeller anemometers, as well as the operating limits of the pressure transducers. After the warm-up period, the fan speed was set to as close to 1300 rpm as possible by varying the frequency on the Mitsubishi E700 drive controller. The speed was checked before each new reading using a hand-held tachometer and corrected as needed to ensure all readings were taken at identical fan speeds. The readings were taken for decreasing flow rates which means that the overlapping throttle was incrementally closed. Through trial-and-error the throttle increments were selected to obtain a good resolution across the entire range of the performance curves. Upon completion of a curve, the fan was shut down and all equipment was left until standstill before the two 'zero' readings were taken. All of the measurement equipment is electronic and is thus prone to creep with time and temperature. Despite this deviation of the zero value of the equipment, the response of the device remained identical to the calibration curves. The purpose of the zero readings for each data set is thus to compensate for any electronic creep that might have occurred since calibration. In the case of the torque transducer installed in the edge fan tunnel, an additional reading was taken without the fan installed but with the motor running at 1300 rpm. This 'no-load' value allows the torque transducer to indicate how much resistance is the result of mechanical friction. This no-load value is critical in obtaining an accurate shaft power reading for the edge fan. Again, most of the performance curve tests were conducted twice to ensure repeatability. As mentioned before, all the equipment used is electronic in nature and apart from creep, is prone to interference too. Since the laboratory has 400 V 3-phase power running along every wall, interference was a concern. It was thus considered good practise to repeat any data points that were identified as anomalies.

The correct blade angles were obtained through trial-and-error runs of the performance curve. Since the design point (static pressure rise of 35.054 Pa at 1.092 m<sup>3</sup>/s volume flow rate for 750 rpm and 1.2 kg/m<sup>3</sup> air density) is between the first and second data points, only these two readings were repeated for each new blade angle until the data indicated that the fan curve was acceptably close (less than 5 %) from the design point.

The fan static rise performance curves for each fan can be seen in Figure 4.14, Figure 4.15, Figure 4.16, and Figure 4.19. The inclusion of the torque transducer in the edge fan tunnel allowed measuring the shaft torque and made it possible to calculate the shaft power and fan static efficiency for the edge N fan and B fan. The shaft power curve and fan static efficiency



curve for the edge N fan (fan 3) can be seen in Figure 4.17 and Figure 4.18. Similarly, the shaft power curve and fan static efficiency curve for the B fan can be seen in Figure 4.20 and Figure 4.21.

Note that all performance curves were standardised to  $1.2 \text{ kg/m}^3$  air density and 750 rpm in order to provide continuity with the testing done by Visser and Salta & Kröger.

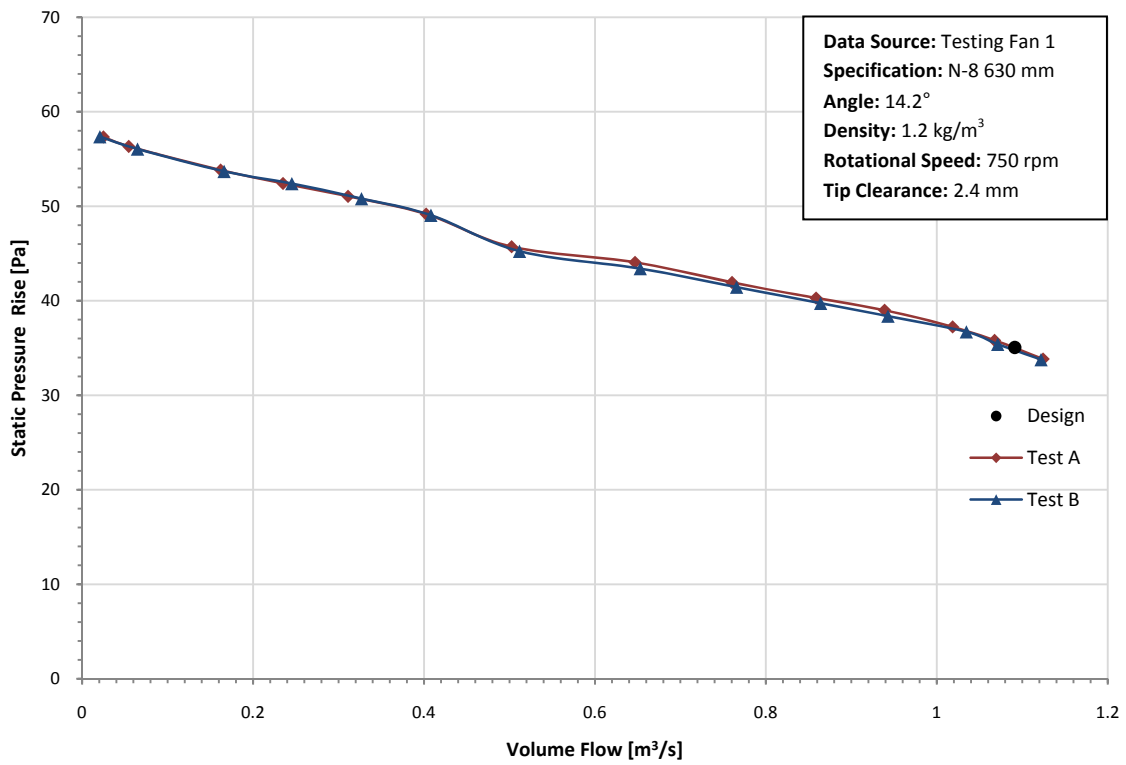


Figure 4.14 N fan static pressure rise curve (fan 1)

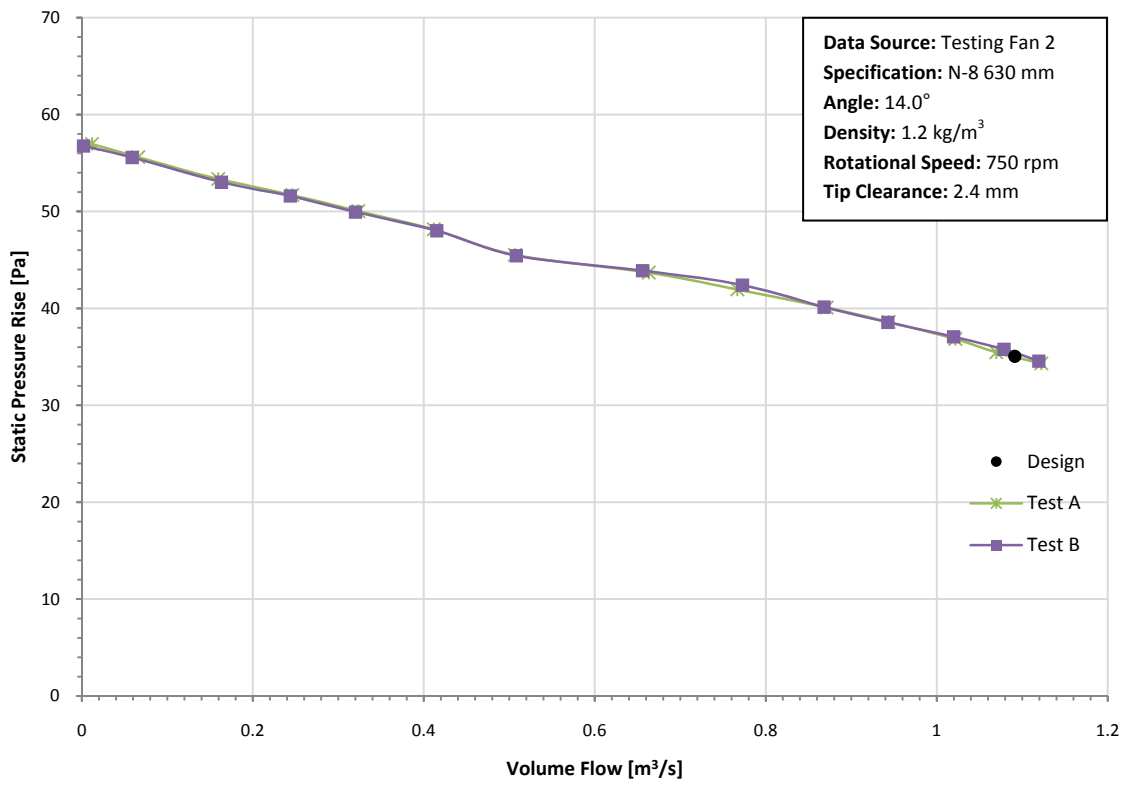


Figure 4.15 N fan static pressure rise curve (fan 2)

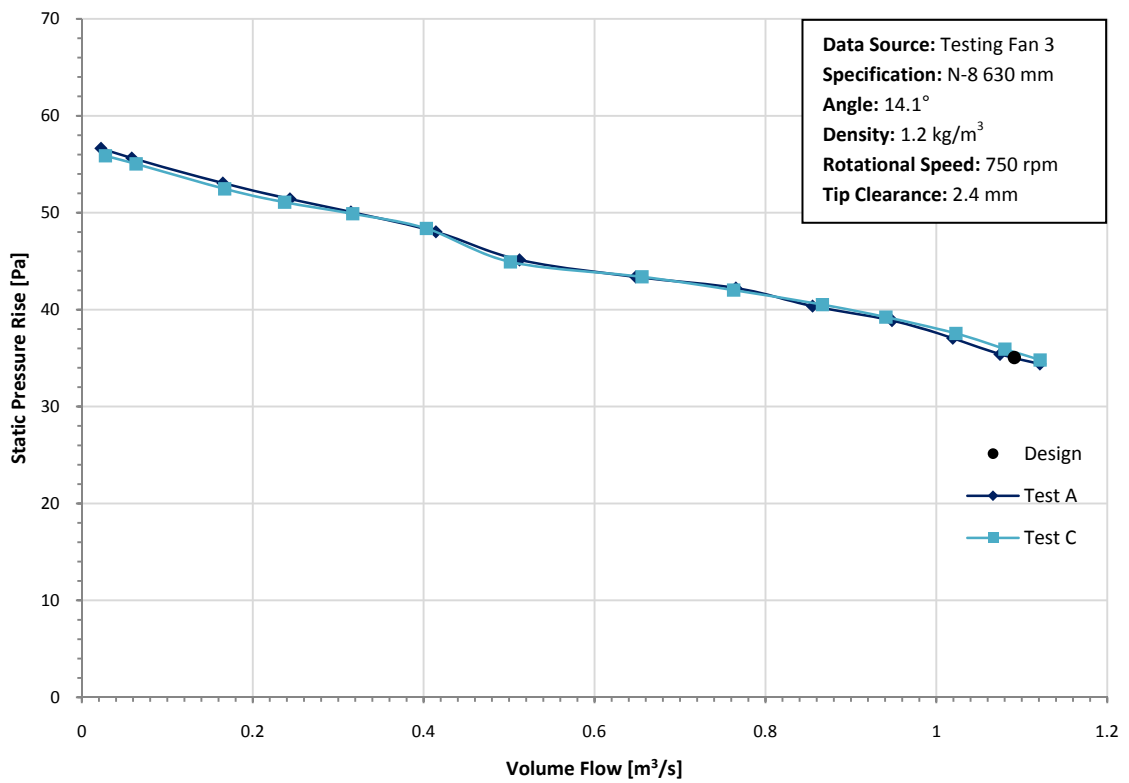


Figure 4.16 N fan static pressure rise curve (fan 3)

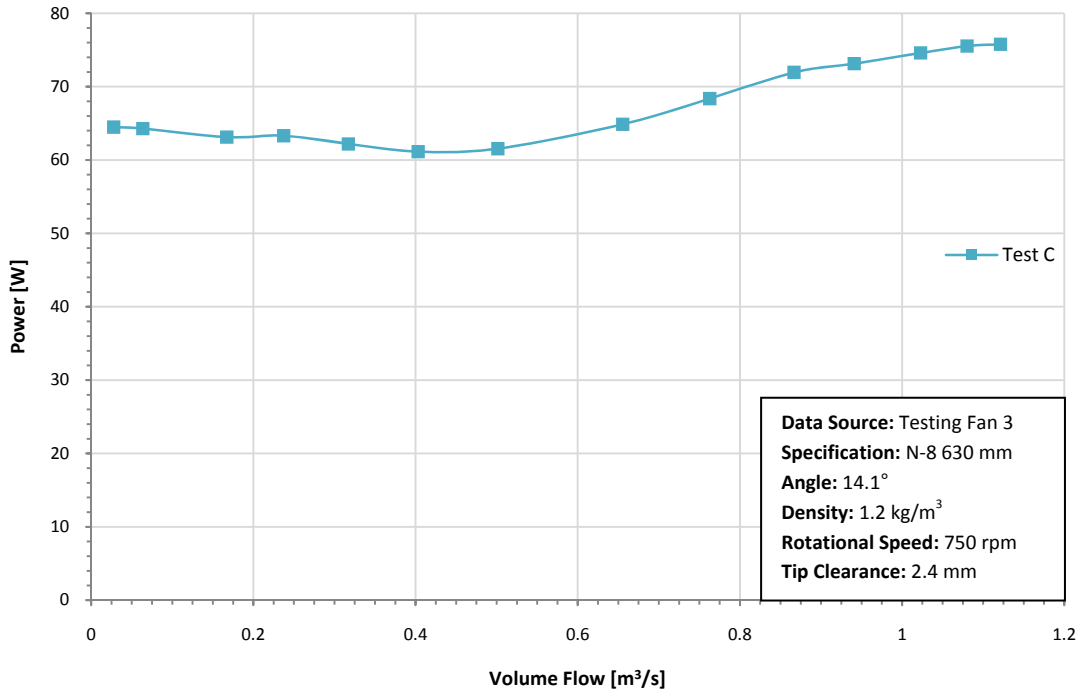


Figure 4.17 N fan power curve (fan 3)

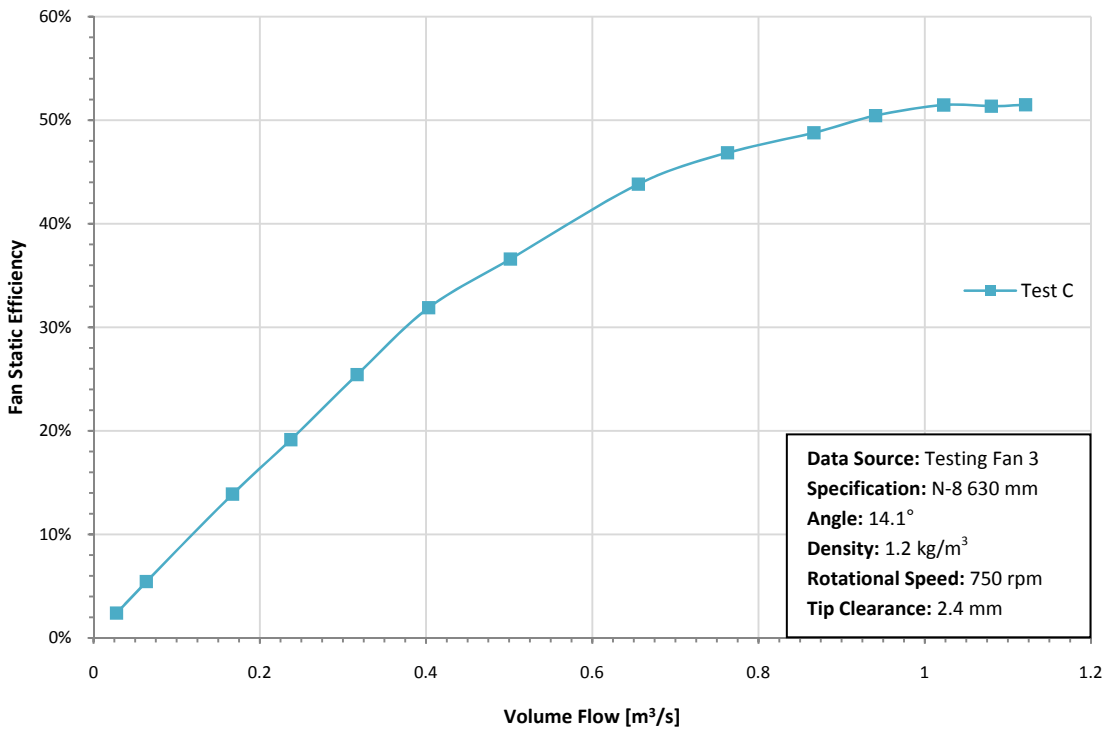


Figure 4.18 N fan static efficiency curve (fan 3)

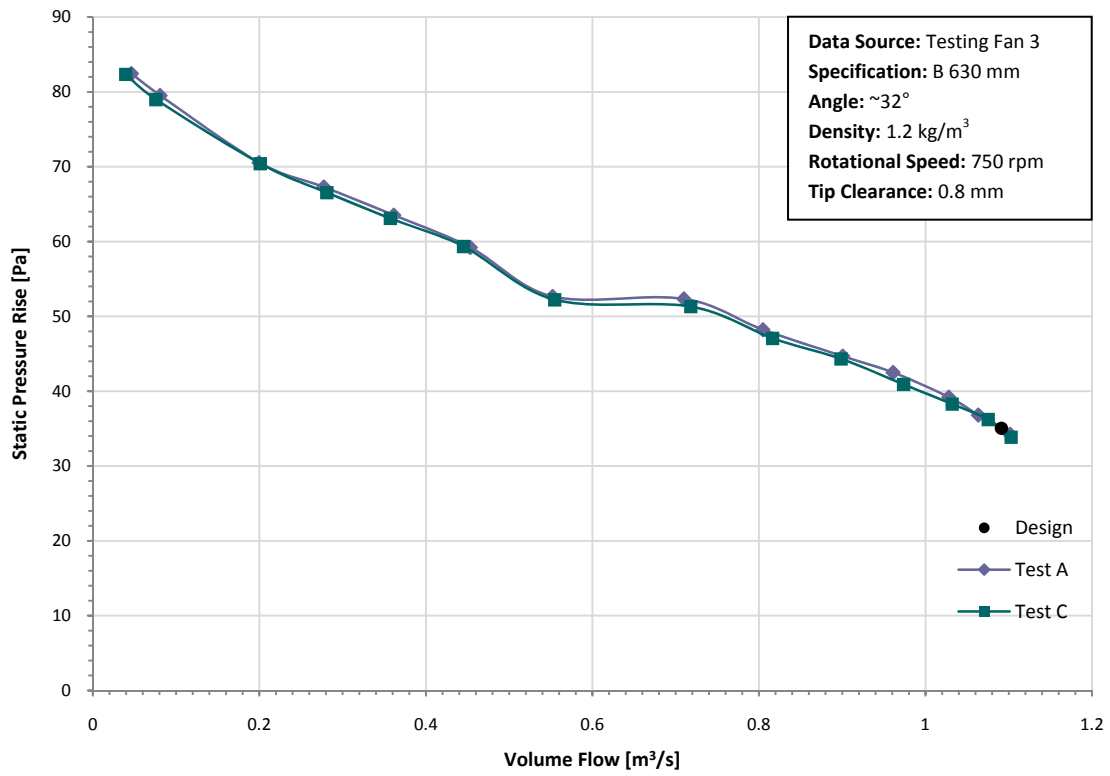


Figure 4.19 B fan static pressure rise curve (fan 3)

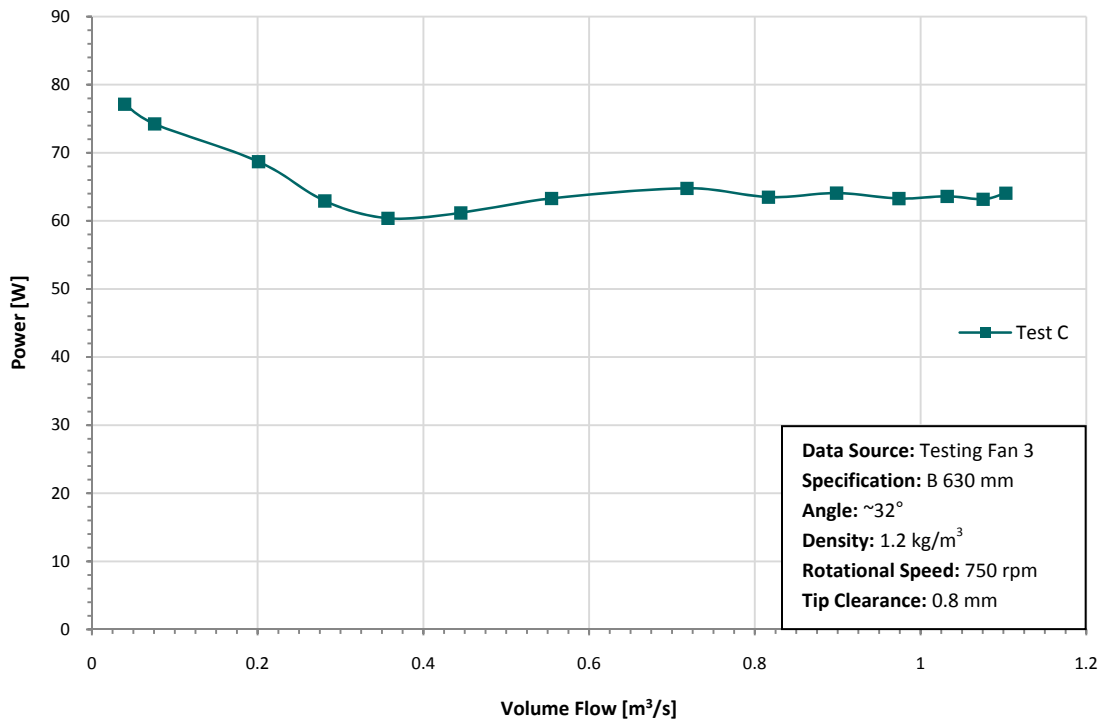
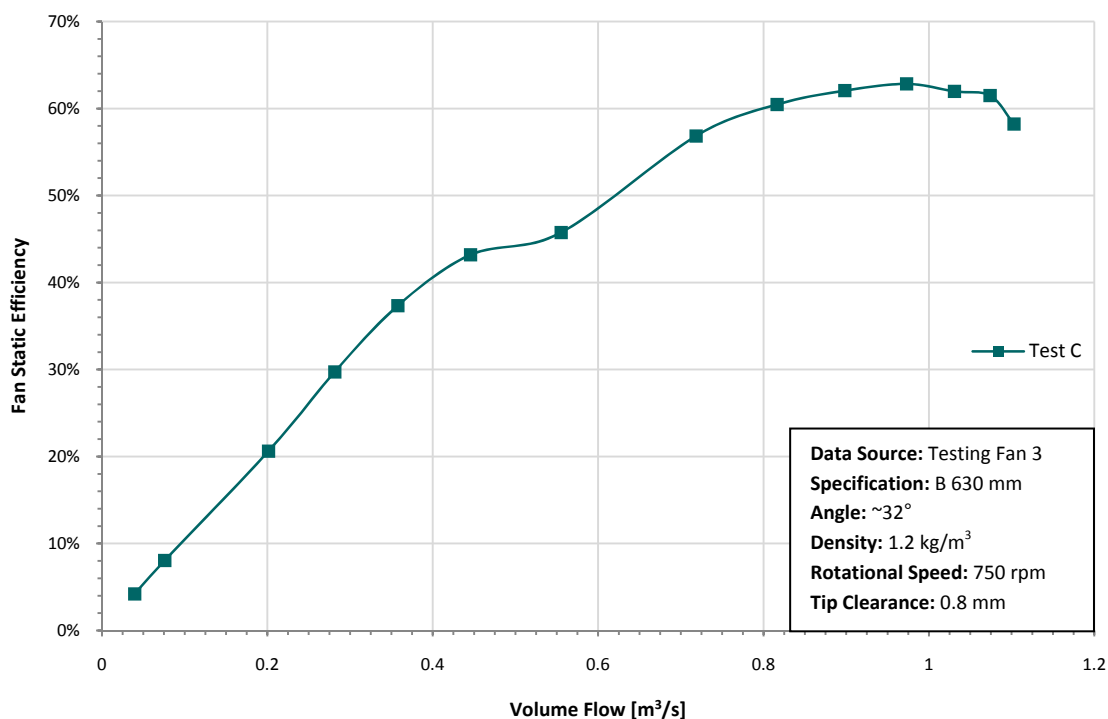


Figure 4.20 B fan power curve (fan 3)



**Figure 4.21** B fan static efficiency curve (fan 3)

The obtained fan static rise performance curves (Test A, B and C) are close to each other and suggest good repeatability. Inter fan comparison (fan 1, 2 and 3) shows that all the N fans perform almost identically. The distinctive plateau that signifies stall is identically positioned (for volume flow) on all three N fans (Figure 4.14, 4.15 and 4.16).

For the N fan, the power curve (Figure 4.17) shows some interesting behaviour as the shaft power appears to increase as the volume flow is decreased past the point of stall, contrary to the expected decrease in power due to the decrease in volume flow. Despite this, the fan static efficiency curve (Figure 4.18) is smooth and reaches the maximum efficiency of 51.5 % at the design point. This suggests that the fan was well specified for its application.

The B fan exhibits a much steeper fan static pressure rise curve gradient (Figure 4.19) and as a result achieves a more than 20 Pa (almost 20%) greater pressure rise at low volume flow rates than the N fan. The plateau in the fan static pressure rise curve that signifies stall is noticeably more prevalent than on the N fan curves. The plateau also occurs slightly earlier (for decreasing volume flow) than it does on the N fan suggesting stall will occur earlier under non-

ideal conditions. Despite this, the much steeper performance curve should offset this earlier stall.

The B fan power curve (Figure 4.20) exhibits the same increase in power with decreasing volume flow past the point of stall as the N fan, but to a much greater extent. The power curve is also not very smooth but a definite trend is present despite small deviations in the data points. The fan static efficiency curve (Figure 4.21) shows a slight dip which corresponds with the plateau in fan static pressure performance. The B fan reaches a maximum static efficiency of almost 63 % which is within 2 % of Bruneau's own results.

#### **4.4 FAN ARRAY PERFORMANCE**

As mentioned previously, the objective of the fan array testing is to repeat the experiments done by Salta & Kröger (1995) but using different fans. Therefore the testing methodology for the fan array testing is based on the same methodology followed by Salta & Kröger.

Before any testing was conducted, the perforated plate throttles were installed and individual fan performance readings were taken again. Using a trial-and-error approach, the perforated plate holes were closed using plastic plugs in order to have each individual fan perform at the design point before the fan array was tested. Care was taken to arrange the plugs in an even distribution. The final composition consisted of 15 plugs arranged as shown in Figure 4.22. Ultimately, all fans achieved the design point performance using identical throttle plug arrangements.

As with the single fan testing, all the fans were left to run for at least 10 minutes to allow all the equipment and mechanical interfaces to reach steady state conditions. After this, the rpm of each fan was checked using a hand held tachometer and the drive was adjusted to get all the fans as close to 1300 rpm as possible. Since all the fans are driven off the same controller, fans speed varied slightly from fan to fan. As with the individual tests, the fan speeds were checked and adapted before each new reading was taken to ensure that the fan speeds remain constant throughout the entire test run.

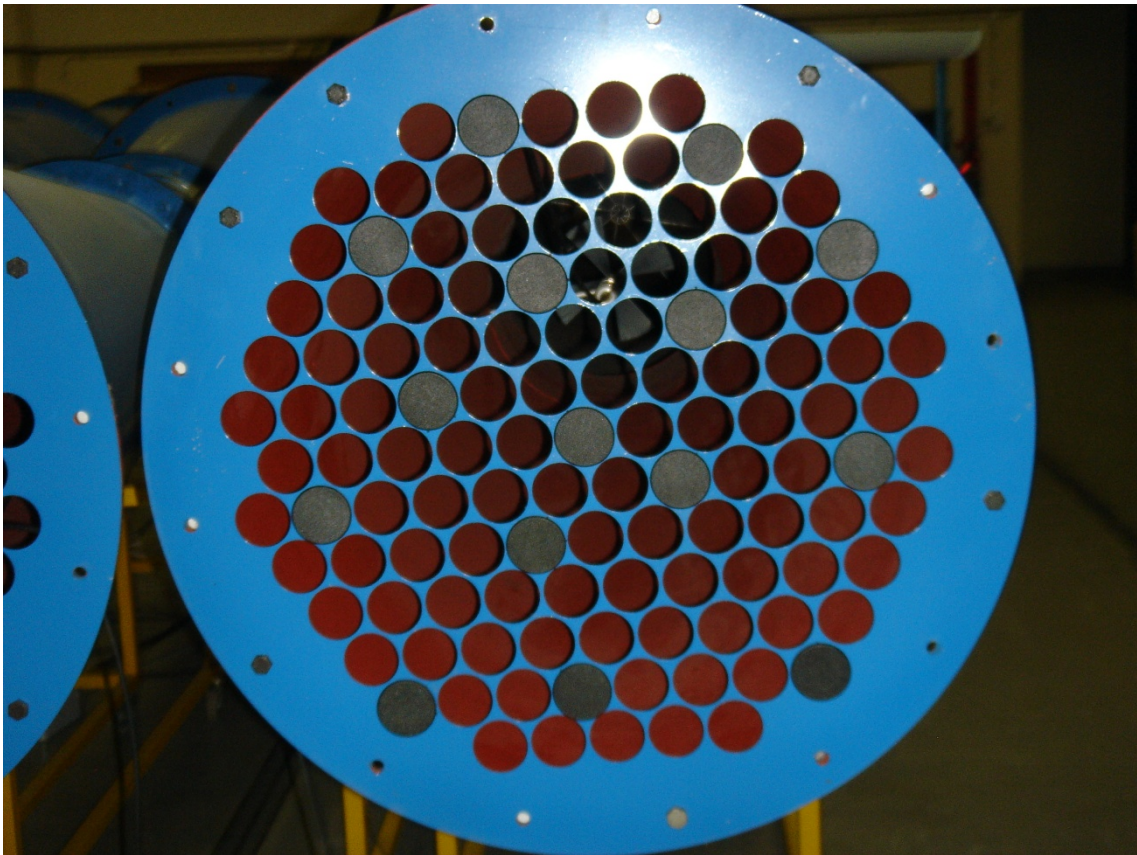


**Figure 4.22** Plug configuration in perforated plate for array testing

The first reading was taken with no 'floor', or rather, an infinitely high platform. However, an infinitely high platform is not possible so for the first no-floor reading, the platform height was equated to the distance to the wall of the laboratory. In this case this 'platform height' was 5 m and represented a platform height of eight times the fan diameter, or the equivalent of a 72 m high platform for the full-scale installation. The readings were taken for decreasing platform height according to the distances in Figure 4.8. For the last reading at minimum platform height, a chamfer, as seen in Figure 4.23, was placed in the corner where the 'floor' and the 'symmetry' plane meet. This was done as a suggestion based on previous testing on the array. The chamfer eliminates the recirculation zone in the corner in front of Fan 1 which had been found to cause cyclic fluctuations in the volume flow readings as the recirculation zone grows and is swept up into the flow.

After each complete run the system was shut down and all equipment was left to reach standstill before the zero reading was taken. The entire process was repeated at least twice for both the N-N-N and N-N-B configurations.



**Figure 4.23** Corner chamfer for 'lowest' platform height setting

The resulting data points for the N-N-N configuration are plotted against the correlation of Salta & Kröger in Figure 4.24 and clearly shows that, apart from the second last 'floor' setting, the Salta & Kröger correlation does predict the N-N-N performance relatively well (less than 3%).

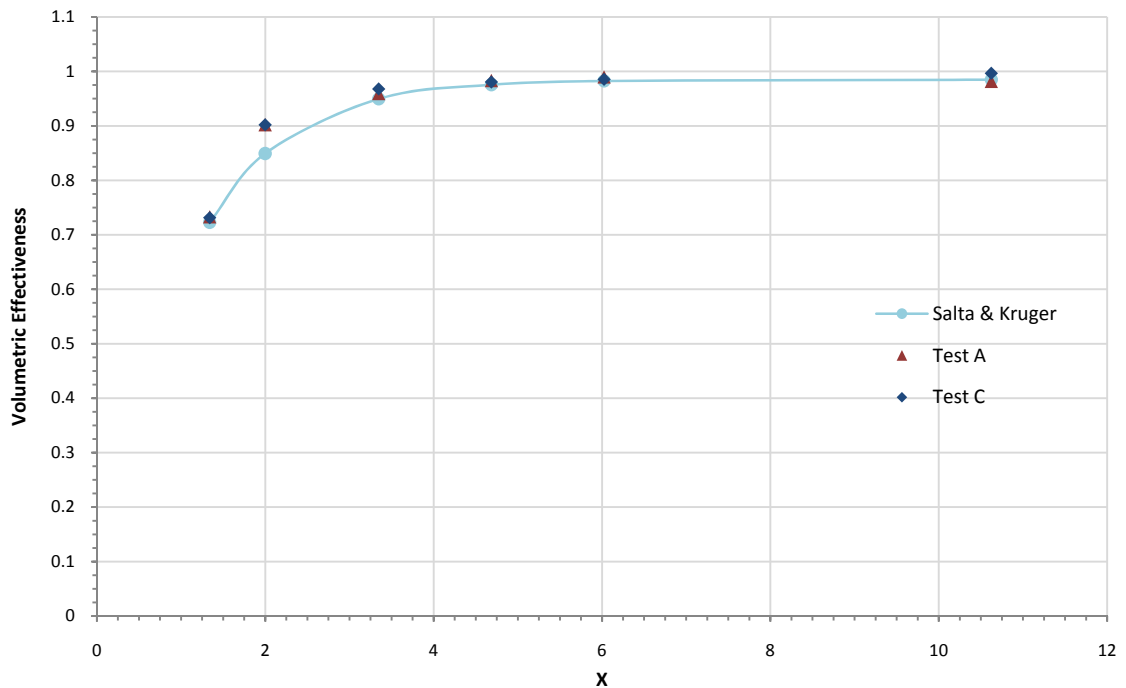


**Figure 4.24** System volumetric effectiveness for N-N-N configuration



The same comparison between the N-N-B configuration and Salta & Kröger correlation can be seen in Figure 4.25 and shows that the N-N-B system performs significantly better (6 – 8% higher) than predicted at very low ‘platform heights’, but follows the prediction very well (less than 3%) for platform heights greater than two and a half times the fan diameter ( $X \geq 3.3$ ).

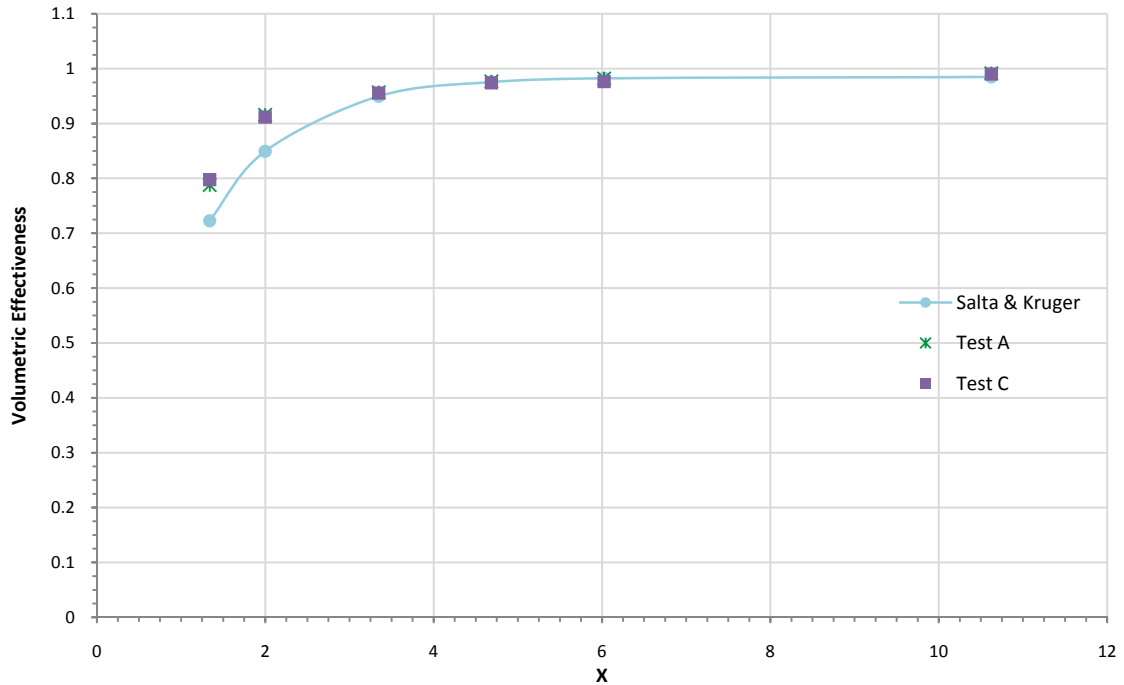


**Figure 4.25** System volumetric effectiveness for N-N-B configuration

Comparing the data sets for the N-N-N and N-N-B configurations, seen in Figure 4.26, shows that the N-N-B achieves marginally better volumetric effectiveness for a platform height of one and half times the fan diameter ( $X = 2$ ), but performs about 7.5 % better when the platform height is reduced to only one fan diameter.

Note that ‘X’ is a dimensionless relationship between platform height, fan diameter and number of fan rows and is defined as part of Equation 4.2.

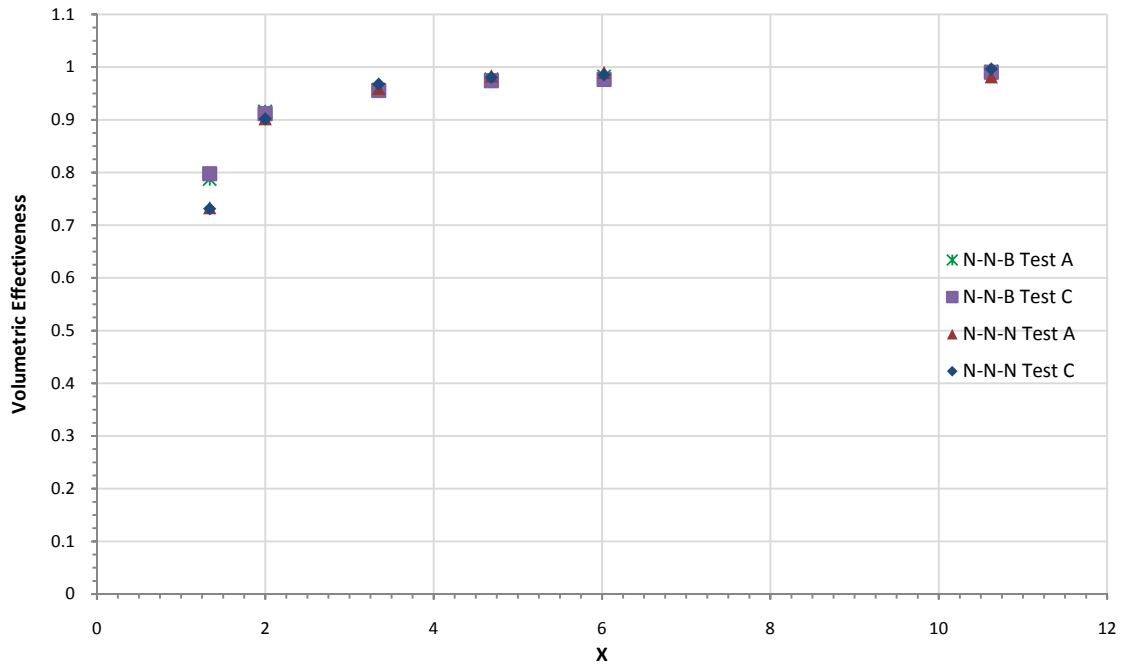


Figure 4.26 Comparative system volumetric effectiveness for N-N-N and N-N-B configuration

The only difference between the N-N-N and N-N-B configurations is the use of the B fan as an edge fan instead of the N fan. To understand the system effects better, a brief comparison of the individual edge fan performance will also be discussed.

A comparison of the edge fan volumetric effectiveness for the N fan and B fan can be seen in Figure 4.27 and reveals that the N fan performs better than the B fan for all platform heights greater than one and a half times the fan diameter. At lower platform heights, the B fan provides a significant advantage. On closer inspection of Figure 4.26 this N fan superiority at greater platform heights is noticeable, although the performance difference is reduced when combined with the volumetric effectiveness of the two inner fans.

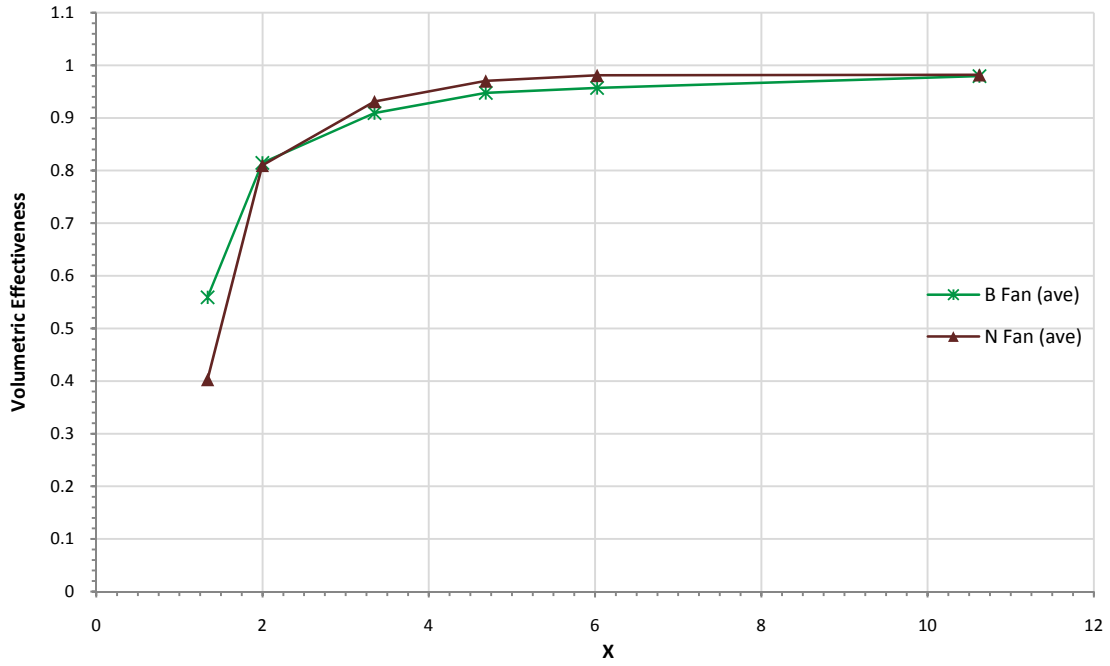


Figure 4.27 Comparative individual fan volumetric effectiveness for N fan and B fan as edge fan

It has already been established that the B fan is more efficient than the N fan for individual fan performance curves. Comparing the power consumption of the B fan and N fan as edge fans in the array, Figure 4.28, clearly shows that the B fan requires less power.

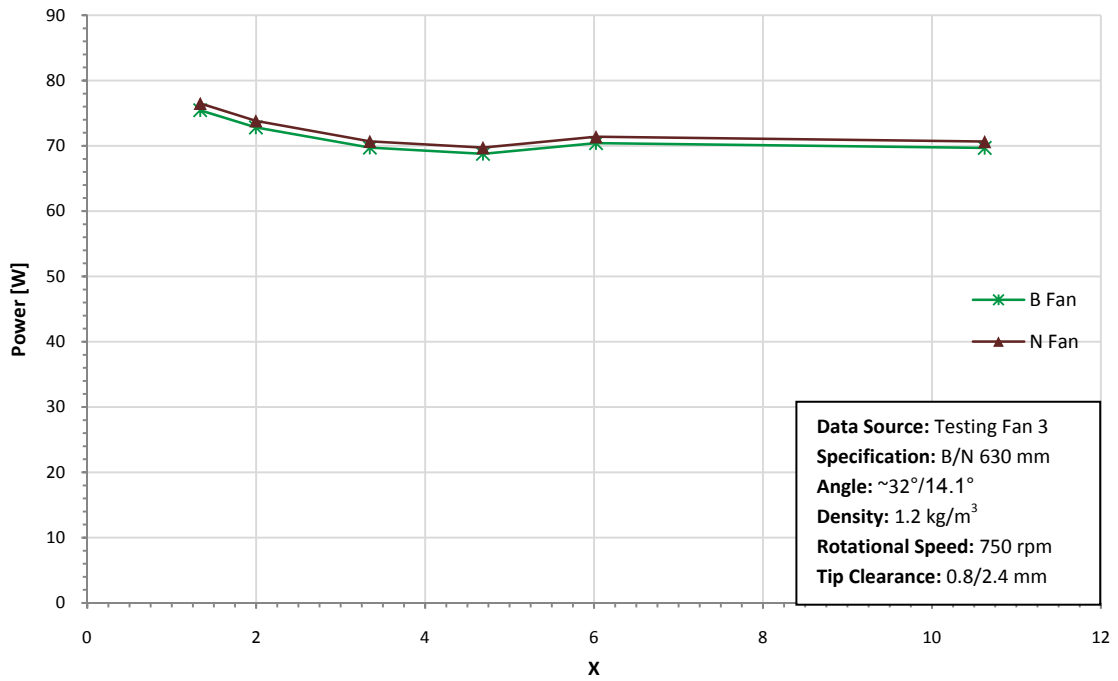


Figure 4.28 Comparative fan power curves for N fan and B fan as edge fans

The power curves for both the N fan and B fan show peculiar behaviour as the power firstly increases with decreasing platform height and then suddenly drops, after which the power required increases again. It was expected that the power consumption will remain relatively insensitive to the change in floor height since Stinnes determined that cross-flow inlet conditions had practically no influence on fan power. For the final platform position, the power requirements for both fans are about 8 % more than for no floor installed. From minimum to maximum values, the power requirements vary by almost 10 %.

#### **4.5 CONCLUSION**

The refitting of the tunnels, although time consuming, proved successful in modernising the tunnels and allowing integration of the equipment into one streamlined data logging solution. The inclusion of the torque transducer in the edge fan tunnel allowed measurements that both Visser (1990) and Salta & Kröger (1995) were unable to incorporate into their research.

The manufacturing of the N fan as a reference fan provided this investigation with a best possible reference and provided another step in the process to develop a scaled multi-fan array testing platform that would give fan developers and researchers the opportunity to get a better idea of how their respective fans will perform in a full-scale installation.

The N fan was manufactured using a manual injection moulding process that involved some degree of hand finishing. Despite this, the fans all perform almost identically and with surface finishes that far exceed the surface finish any full-scale fan might be manufactured to. This near perfect surface finish allows the customising of the surface finish to suite the needs of the experiment.

The B fan was machined from aluminium and, although there was some hand finishing involved, the B fan is well balanced and required no additional modifications. As with the N fan, the surface finish far exceeds the finishing standards for full-scale fan manufacturing, and again allows for customising of the surface finish as needed. The spherical hub and cylindrical blade roots sealed well for the range of blade angles used during the initial tests to obtain the correct blade angle.

For both the N fan and B fan, the blade angles which produced the correct performance agree well (within 1°) with the previous testing and manufacturer data. To obtain the full-scale design point, the manufacturer specified the N fan a 14° blade angle which compares favourably with the 14°-14.2° blade angles obtained for the scaled N fans. Despite having established that including the Reynolds number into the scaled fan tests has a detrimental effect on the fan performance, the correlation in blade angles between the 630 mm and the 9216 mm fan suggests that the manufacturer might have ignored said Reynolds number effects when conducting performance tests and scaling them to full-scale performance curves. The Reynolds number ranges for the scaled B fan and the 1542 mm fan with which Bruneau himself performed design evaluation tests, are much closer and good angle correlation was to be expected. The B fan blade angle of 32° (or 58° as measured by Bruneau) is very close to the 59° blade angle that Bruneau used to achieve the desired fan static pressure rise performance. Post testing measurement of the tripped N fan blade angles (trip wires removed) revealed that the required blade angle for the equivalent performance when fitting trip wires was 15.5° – 15.8°.

The differences between the N fan and B fan individual performance curves are immediately apparent. The B fan has a much steeper fan static pressure rise curve which results in a more than 40 % higher fan static pressure rise than the N fan. The B fan also exhibits stall slightly earlier than the N fan and the plateau that depicts stall is much more pronounced than for the N fan. Stall is brought on by the off-design relative inlet velocity of the air onto the blade. The angle at which the air flows onto the blade is a function of the blade rotational speed and the incoming flow, and as the fan is throttled, the incoming flow decreases. As the incoming flow velocity decreases, the effective angle of attack increases until the angle is steep enough to lead to flow separation on the upper surface of the blade, causing what is also known as stall. The earlier onset of stall may be a result of the more aggressive twist present in the B fan blade design.

The power curves for the N fan and B fan both exhibit that same behaviour. Both power curves decrease with decreasing volume flow but start to increase again after stall occurs. The decrease in power is a result of less work being done due to lower volume flow rates. The increase of power consumption may be attributed to the increased pressure induced drag due to stall. The effective angle of attack increases with decreasing through flow and as the

effective angle of attack increases, the portion of the upper surface of the blade that is in stall increases. The stall causes a low pressure zone which increases the pressure induced drag, and the larger the low pressure zone, the greater the drag. This effect appears to be more pronounced for the B fan than for the N fan. The shaped of both power curves do not compare favourably with their larger scale counterparts (see Appendix B) and may be the result of Reynolds number differences. Despite these small discrepancies, both fan static efficiency curves are close to previously tested data (Bruneau, 1994 and Venter, 1990). The maximum fan static efficiency obtained for the N fan (51.5 %) differs greatly from the fan static efficiency supplied by the manufacturer (63 %) but compares better with the maximum fan static efficiencies obtained by Venter (1990) and Bruneau (1994) – 55% and 54 % respectively. The maximum efficiency for the B fan (63 %) is only slightly greater than the maximum fan static efficiency obtained by Bruneau (1994) for the 1.542 m B fan with a sealed root and inlet nose-cone (60 %). The slightly better fan static efficiency of the 630 mm scale B fan may be attributed to the very smooth surface finish of the blades.

The first objective for the multi-fan array testing was to determine how well the system volumetric effectiveness prediction model formulated by Salta & Kröger predicts the performance of fans other than the fans used by Salta & Kruger to derive the model. The multi-fan correlation from the model performs well in predicting the performance of the N-N-N array at greater platform heights. However, the correlation by Salta & Kröger tends to overpredict the decrease in volumetric effectiveness that the system experiences due to lower platform heights. The N-N-B performs similarly to the N-N-N configuration for greater platform heights but exceeds the N-N-N configuration when the platform height decreases to extreme levels of inlet distortion. Again, although not unexpected given the mixed fan configuration, the Salta & Kröger correlation overpredicts the decrease in performance experienced by the N-N-B system. It may appear that the Salta & Kröger model is not as effective at predicting the system volumetric effectiveness when using fans other than the ones used to gather the test data on which the model is based. However, it is suggested to recreate the original Salta & Kröger experiment with the original fans to determine whether the deviation from the model is a fan property or whether it may be a result of yet undetermined factors.

Evaluating the edge fans separately reveals an interesting behaviour in performance. At greater platform heights (more than one and a half times the fan diameter), the N fan

outperforms the B fan for volumetric effectiveness. It is also noteworthy that both fans experience an immediate decrease in volumetric effectiveness when placed in the communal inlet, although this decrease is very small. However, when inlet conditions deteriorate at very low platform heights, the B fan comes into its own and, for the lowest tested platform height setting, the B fan performs significantly better than the N fan as an edge fan.

The edge fan power consumption reveals an interesting phenomenon. Both fans appear show a slight increase in power consumption as the moveable floor is inserted for the first time. Strangely, the next setting sees a drop in power consumption after which it steadily increases for decreasing platform height. This behaviour is contrary to what Stinnes (1998) found since his tests showed that the power consumption remained unaffected by changes in cross-flow inlet conditions. However, the behaviour of the N fan and B fan as edge fans can be partially explained by the work of Hotchkiss et al. (2006) who measured the blade torque across the entire diameter of the fan and for various cross-flow inlet conditions. They found that the increase in torque on one side of the fan is offset by a decrease in torque on the 180° opposite side. Conversely, it was found that for higher cross-flow inlet conditions, the averaged increase in torque on one side of the fan is slightly greater than the averaged decrease in torque on the opposite side of the fan. The investigation of Hotchkiss et al. was only done up to a cross-flow inlet angle of 45°, at which this imbalance was the greatest, but it is possible that this imbalance continues to grow as the cross-flow inlet angle increases, although without an additional investigation, it can not be said for certain.

Apart from this decrease and increase of power consumption, it was found that the B fan, as an edge fan in an array, still requires less power than the N fan.

Several observations were made during individual fan testing and multi-fan array testing. The first was that the fan speed appears to increase with decreasing volume flow rate, but only up to fan stall after which the fan speed remained relatively constant. The increase in static pressure rise with decreasing volume flow rate is not a directly proportional relationship which means that the work required by the fan decreases as well, resulting in a decrease in load on the motor and the subsequent increase in fan speed. At the time that this investigation's testing ended, a magnetic pickup had been installed onto each fan shaft which will allow a fan speed reading to be taken for each data point and decrease testing time.

The second observation was the amount of backflow around the hub of the N fan at smaller throttle openings. This was noted during the fan speed checks and could easily be visualised by holding a piece of string near the hub. The round blade roots and small hub of the N fan results in an annulus where no work is done by the fan, resulting in a low-pressure 'opening' near the hub where higher pressure flow can easily escape through. This flow is ultimately sucked back into the fan but subtracts from the flow actually exiting the tunnel.

The final observation was with regards to the torque readings on the edge fan. The torque transducer installed in the tunnel is rated at 100 Nm and far exceeds the torque seen for the testing in this investigation. This means that the torque transducer registers a mere 0.21 V for normal testing conditions, which is almost negligibly low when considered that maximum output is 5 V. Likewise, the no-load torque reading for the fan is a third of the full-load reading. The over-specified torque transducer is not designed to operate under such low-torque conditions and this leads to oscillations in the torque readings. These oscillations are then amplified by the gradient of the calibration curve. This explains why the power curves during individual fan testing and array testing are not necessarily smooth and why often several readings had to be taken before an acceptable reading was obtained (acceptable in that it follows the trend well).



## 5 CONCLUSION

The global objective for this investigation was to develop a scaled fan testing platform, or part thereof, that would accurately mimic the behaviour of fans in a full-scale installation and allow for fan testing and development on a more manageable and measureable scale. This objective was broken down into two smaller investigations.

The first investigation was to determine what, if any, effect on fan performance it would have if Reynolds number effects were incorporated into the testing. Using a powerful new transition model, the turbulence transition onset position for the full-scale fan blades were obtained using computational fluid dynamics. Using this information, it was possible to select and position two-dimensional roughness elements, trip wires in this case, that should induce transition onset on the scaled fan blades at a similar position to the transition onset position on the full scaled fans. The experimental verification showed that the presence of the trip wires caused an all-round performance decrease in the N fans, but the fan static pressure performance curve retained a shape similar to that of the non-tripped fan. The experiment was repeated using a different tunnel and fan combination (still N fan but in tunnel 3) but with an increased blade angle to obtain the same design performance point. This experiment revealed that once the correct blade angle was set, the fan static pressure rise performance curves compared very well (less than 4%). From this initial investigation it was concluded that incorporating compensation for Reynolds number effects into the scaled fan testing does not influence the fan response (curve shape and gradient) to any major extent and may, at own discretion, be ignored.

The second investigation compared the multi-fan array performance to a system volumetric effectiveness model for varying platform heights and fan rows. The effect of varying platform heights was simulated through different positions of a moveable floor while the number of simulated fan rows was kept constant at six. The use of symmetry planes meant that a six row bay can be simulated with only three fans. It was found that the prediction model over-predicts the decrease in performance at extremely low platform heights for an N-N-N configuration. This discrepancy is even greater when the B fan was installed as an edge fan. The slight increase in volumetric effectiveness achieved under adverse conditions from

installing the B fan as an edge fan proved that the B fan is indeed better suited than the N fan for highly distorted inlet conditions.

The investigations that form part of the global objective were successful in gaining experience and knowledge about how to best develop a scaled testing platform that compares well with full-scale fan behaviour. Both the Reynolds number investigation and multi-fan array investigation can be expanded in future research.

## 6 REFERENCES

British Standards Institution, 1997. BS848: 1997 *Fans for general purposes: Part 1. Performance testing using standardized airways*.

Bruneau, P.R.P., 1994. *The Design of a Single Rotor Axial Flow Fan for a Cooling Tower Application*. MScEng Thesis. University of Stellenbosch.

Colman, J., Marañón Di Leo, J., Delnero, J.S., Martínez, M., Boldes, U. & Bacchi, F., 2008. Life and Drag Coefficients Behaviour at Low Reynolds Number in an Airfoil with Gurney Flap Submitted to a Turbulent Flow: Part 1. *Latin American Applied Research*, (38), pp.195-200.

Gibbings, J.C., 1959. *On Boundary-Layer Transition Wires*. A.R.C Technical Report. London: Her Majesty's Stationary Office Aeronautical Research Council. CP-462.

Hotchkiss, P.J., Meyer, C.J. & von Backström, T.W., 2006. Numerical investigation into the effect of cross-flow on the performance of axial flow fans in forced draught air-cooled heat exchangers. *Applied Thermal Engineering*, 26, pp.200-08.

Howden, 2000. *ENF Fan Catalogue*.

Kröger, D.G., 1998. *Air-cooled Heat Exchangers and Cooling Towers*. Stellenbosch.

Langtry, R.B., Menter, F.R., Likki, S.R., Suzen, Y.B., Huang, P.G. & Völker, S., 2006. A Correlation-Based Transition Model Using Local Variables - Part 2: Test Cases and Industrial Applications. *Journal of Turbomachinery*, 128(July), pp.423-34.

McGhee, R.J., Beasley, W.D. & Somers, D.M., 1977. *Low-Speed Aerodynamic Characteristics of a 13-Percent-Thick Airfoil Section Designed for General Aviation Applications*. Hampton, Virginia: National Aeronautics and Space Administration.

Menter, F.R., Langtry, R.B., Likki, S.R., Suzen, Y.B., Huang, P.G. & Völker, S., 2006. A Correlation-Based Transition Model Using Local Variables - Part 1: Model Formulation. *Journal of Turbomachinery*, 128(July), pp.413-22.

Meyer, C.J. & Kröger, D.G., 2001. Numerical Simulation of the Flow Field in the Vicinity of an Axial Flow Fan. *International Journal for Numerical Methods in Fluids*, 36, pp.947-69.

Meyer, C.J. & Kröger, D.G., 2004. A Numerical Investigation of the Errors Associated with the Scaling of Axial Flow Fan Performance Characteristics. *R & D Journal (incorporated into The SA Mechanical Engineer)*, 20(2), pp.16-24.

Nanovea, 2009. *Topography & Roughness Testing of Sandpaper Surface*. Analytical Report. California: Micro Photonics.

Salta, C.A. & Kröger, D.G., 1995. Effect of Inlet Flow Distortions on Fan Performance in Forced Draught Air-Cooled Heat Exchangers. *Heat Recovery Systems & CHP*, 15(6), pp.555-61.

Sayers, A.T., 1990. *Hydraulic and Compressible Flow Turbomachines*. London: McGraw-Hill.

Stinnes, W., 1998. *The Performance of Axial Fans Subjected to Forced Cross-Flow at Inlet*. MScEng Thesis. University of Stellenbosch.

Tani, I. & Sato, H., 1956. Boundary-Layer Transition by Roughness Element. *Journal of the Physical Society of Japan*, 11(12), p.1284.

van der Spuy, S.J., 1997. *The Design of a Low-Noise Rotor-Only Axial Flow Fan Series*. MScEng Thesis. University of Stellenbosch.

Venter, S.J., 1990. *The Effectiveness of Axial Flow Fans in A-Frame Plenums*. PhD Thesis. University of Stellenbosch.

Visser, J.G.J., 1990. *Die Invloed van Versteurde Inlaatvloeioptrone op Aksiaalwaaiers*. MScIng Tesis. Universiteit of Stellenbosch.

White, F.M., 2006. *Viscous Fluid Flow*. Third Edition (International Edition) ed. Singapore: McGraw-Hill.

## APPENDIX A: EQUIPMENT CALIBRATION

### A.1 CALIBRATION OF REFERENCE PROPELLER ANEMOMETER

In order to ensure the accurate measurement of flow in the test setup, the propeller anemometers located in each duct need to be calibrated. To this end, a reference anemometer needs to be calibrated first.

This reference propeller anemometer is fixed in its own bellmouth and pipe-section which allows the user to eliminate potential problems that might be experienced if the anemometer required disassembly and reassembly every time it was to be moved or recalibrated, and ensure that when the anemometer is used as a reference that the anemometer functions under the same geometric constraints as when the anemometer was calibrated. Figure A.1 shows the propeller anemometer fixed in the bellmouth and pipe-section. The exact geometry of the bellmouth and pipe-section diameter is not important since the calibration was done relative to volume flow and not velocity.



**Figure A.1** Propeller anemometer in casing-bellmouth assembly

### A.1.1 Calibration Setup

The setup used to calibrate the anemometer is known as an atmospheric open-loop induced draft tunnel. A schematic of the tunnel is shown in Figure A.2. This tunnel is commonly used as a platform for testing the thermal performance of extended surfaces like fin tube heat exchangers. In this case only the air-side mass flow rate was determined.

The air flow can be determined by measuring the pressures before and across a series of nozzles. There are five sealable nozzles which, in different combinations, help maintain a measurable pressure drop across the said elliptical nozzles for a wide range of volume flow rates. The exact diameters of these elliptical nozzles are of critical importance. The equation defining the mass flow rate through a nozzle (these individual flow rates can easily be summed if a combination of nozzles were used) is given by Equation A.1. The equation takes into consideration the corrections for losses and variations due to nozzles discharge losses, gas expansion and compressibility by adding the coefficients defined by Equations A.2, A.3 and A.4. (Kröger, 1998) :

$$m = C_n \varphi_g Y A_n (2 \rho_n \Delta p_n)^{0.5} \quad (.10)$$

With

$$C_n = 0.954803 + 6.37817 \cdot 10^{-7} \text{Re}_n - 4.65394 \cdot 10^{-12} \text{Re}_n^2 + 1.33514 \cdot 10^{-17} \quad (\text{A.2a})$$

for  $30000 < \text{Re}_n < 100000$

$$C_n = 0.9758 + 1.08 \cdot 10^{-7} \text{Re}_n - 1.6 \cdot 10^{-13} \text{Re}_n^2 \quad (\text{A.2b})$$

for  $100000 < \text{Re}_n < 350000$

$$C_n = 0.994$$

for  $\text{Re}_n > 350000$

$$\varphi_g = 1 - 3 \Delta p_n / (4 p_{up} c_p / c_v) \quad (\text{A.3})$$

where  $c_p / c_v = 1.4$  ,  $p_{up}$  is the relative pressure upstream of the nozzles and  $\Delta p_n$  is the pressure drop across the nozzle

$$Y = 1 + 0.5 \left( \frac{A_n}{A_{tus}} \right)^2 + 2 \left( \frac{A_n}{A_{tus}} \right)^2 \frac{\Delta p_n}{\frac{\rho_{up} c_p}{c_v}} \quad (\text{A.4})$$

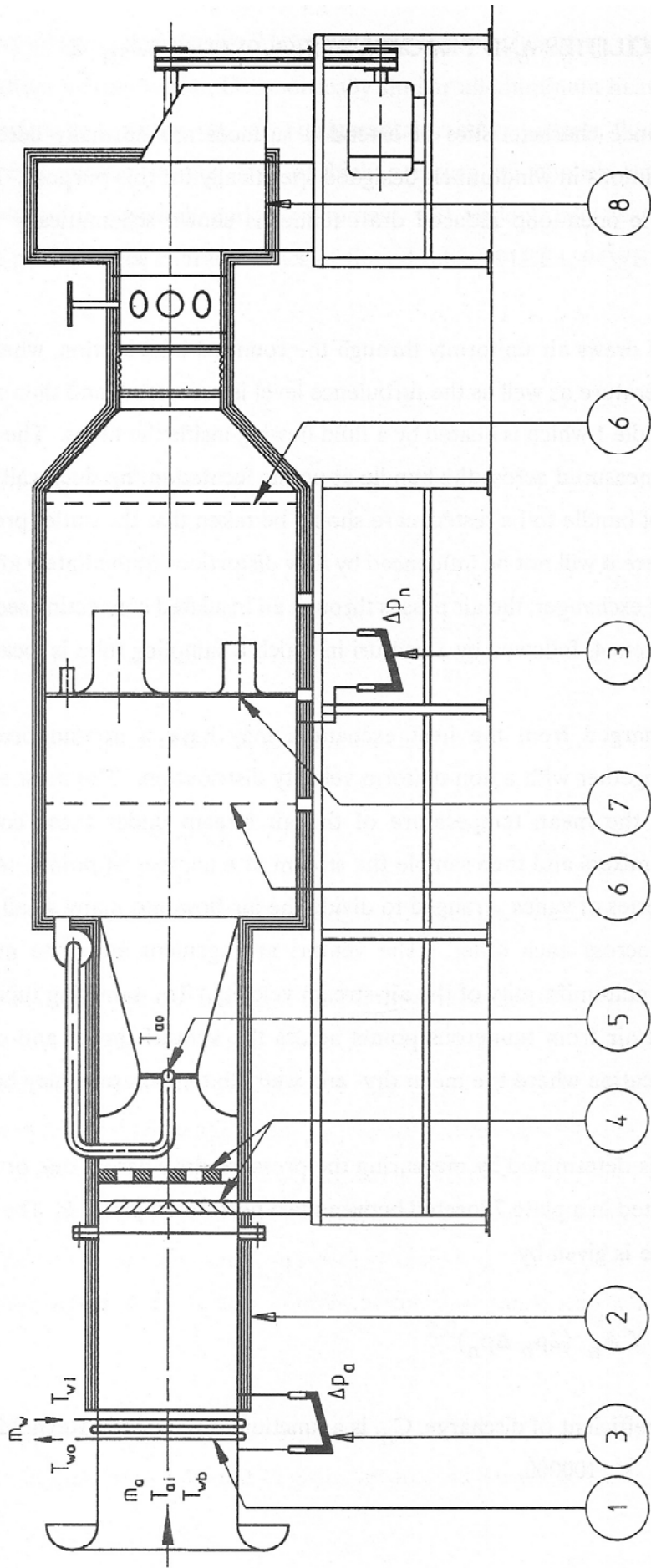


Figure A.2 Schematic of test windtunnel (Kröger, 1998)



A total of three pressure transducers were used to measure pressure variations at specific points. For  $\Delta p_n$  in the above equations, the pressure was measured as indicated at 3 (far right-hand side) in Figure A.2 using pressure transducer number two (numbering based on data logger channel order), while  $p_{up}$ , also measured at 3 in Figure A.2, was measured as relative to atmosphere (high-pressure side left open to atmosphere) using pressure transducer number one. For accuracy, pressure transducer number three was used to measure the pressure drop across the bellmouth of the anemometer housing. The pressure tap was located at a position close to 1 in Figure A.2. This pressure could then be used to more accurately determine the exact density of the air flowing through the anemometer when converting from mass flow to volume flow rate. The air temperature was measured using five type-T thermocouples that were located near the tunnel (not in the tunnel).

The voltages of all the pressure transducers, the propeller anemometer and the temperature readings from the thermocouples were collected using a Schlumberger data logger streaming data to a DX266 desktop computer running a Windows 98 operating system and also featured Microsoft Office XP.

The flow in the tunnel is induced by a radial fan (8 in Figure A.2) capable of delivering a static pressure rise of approximately 2 kPa. The rotational speed of the fan can be controlled using a drivespeed controller that can vary the frequency of the three-phase drive motor between 0 Hz and 50 Hz (capable of higher frequencies but safety precautions prohibit frequencies higher than 50 Hz) in 0.01 Hz increments.

The atmospheric pressure was obtained from a mercury barometer located in the laboratory.

Note that equations A.2a and A.2b are dependent on the Reynolds number, yet in order to determine the Reynolds number, the mass flow through the system needs to be known. This is known as a cyclic dependency and can only be solved iteratively.

## A.1.2 Pressure Transducer Calibration

The accuracy of the pressure transducer readings is of utmost importance since these pressure readings are used to determine the mass flow through the tunnel. Since the pressure transducers for the  $\Delta p_n$  and  $p_{up}$  measurements were newly purchased, the necessity to ensure proper calibration was even more important.

All three pressure transducers work by measuring the variation in capacitance caused by the displacement of a diaphragm due to relative pressure fluctuations. The output from the pressure transducers are linearized inside the pressure transducers before a current is output. A small resistor (250  $\Omega$ ) is placed between the output terminals and the voltage across the resistor is then measured and logged. The new pressure transducers allowed the zero value to be set, which was simply accomplished by opening both pressure taps to atmosphere and zeroing the reading.

The two new pressure transducers have a range of 0 – 10 kPa while pressure transducer three (used to measure the pressure drop across the inlet bellmouth,  $\Delta p_{bellmouth}$ ) has a range of 0 – 2.5 kPa.

All three pressure transducers were calibrated in the same manner. Vacuum was applied to a Betz manometer and then connected to the low-pressure side of each pressure transducer. The 'mm H<sub>2</sub>O' reading was then compared to the corresponding voltage output from the pressure transducer. After it was determined that the reading was stable (no leakages or disturbances), the vacuum was incrementally released and the voltage at each 'step' was correlated with a 'mm H<sub>2</sub>O' reading. The 'mm H<sub>2</sub>O' readings were then converted into pressure values (Pa). It was assumed that since the Betz manometers were in the lab for at least two days prior to the calibration that the water temperature was the same as that of the surrounding air. The gravitational constant used for these conversions was obtained by inserting the latitudinal coordinate of the Stellenbosch University Engineering Faculty into the WGS (World Geodetic System) 84 Ellipsoidal Gravity Formula (Wikipedia, nd). The gravity at the Stellenbosch University Engineering Faculty was found to be  $9.79643 \text{ m} / \text{s}^2$ . Figure A.3 shows the pressure transducer calibration setup.

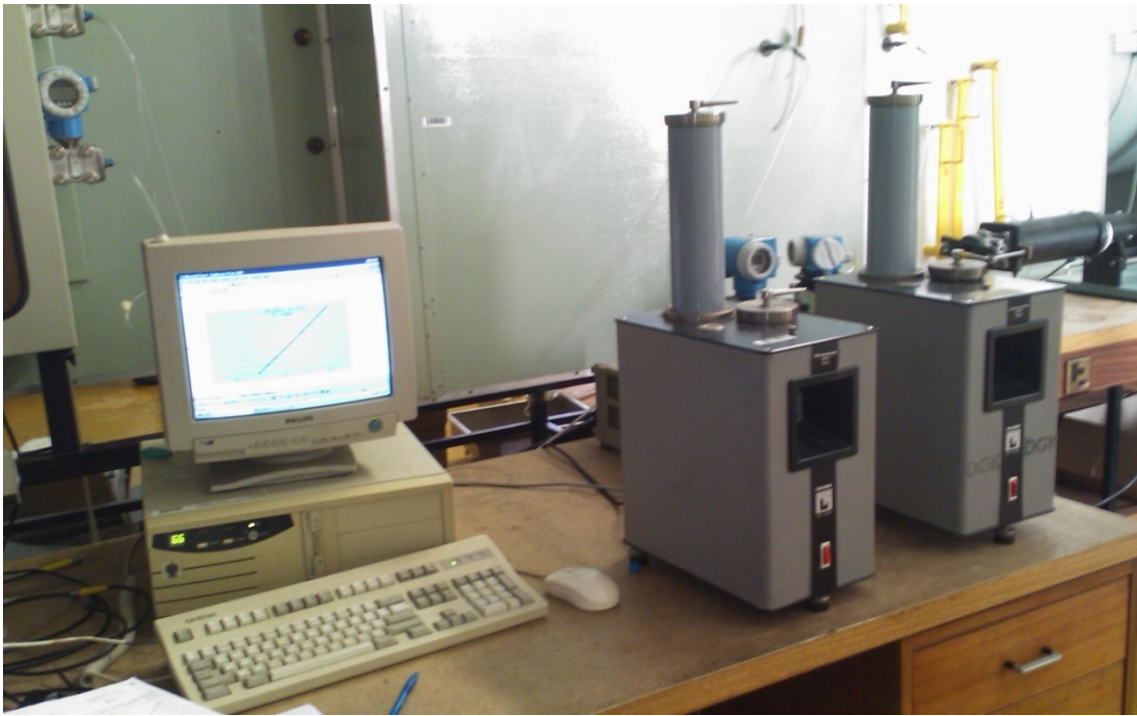


**Figure A.3** Pressure transducer calibration setup

The curves governing the output of the three pressure transducers were eventually found to be:

$$\text{Pressure Transducer 1 (measuring } \Delta p_n) = 2592.9550 \cdot \text{CH17} - 2495.2954 \quad (\text{A.5})$$

$$\text{Pressure Transducer 2 (measuring } p_{up}) = 2595.1986 \cdot \text{CH18} - 2492.6763 \quad (\text{A.6})$$

$$\text{Pressure Transducer 3 (measuring } \Delta p_{\text{bellmouth}}) = 636.9767 \cdot \text{CH19} - 635.5591 \quad (\text{A.7})$$

Where CH17, CH18 and CH19 represent the voltages measured by the data logger on those specific channels. In each occasion the curve fit resulted in a 100% data fit which agrees with the fact that the pressure transducers linearize the output internally. Also, the two new pressure transducers have very similar curve fits. The slight variations may be attributed to the resistances on the output terminals not being exactly identical (the ratings do not necessarily mean the resistor will be exact in its actual resistance).

### **A.1.3 Test Data**

Once the equipment was determined to be as accurate as possible, the calibration of the propeller anemometer could begin. To prove precision and reliability of the testing, the entire calibration process was repeated three times.

The anemometer output increases linearly as the flow rate increases and thus the ideal calibration curve would pass through zero on the vertical axis.

The test procedure was relatively simple: a nozzle or combination of nozzles (nozzle number 4 for most of the data points and combined nozzles 4 and 5 for the greatest flow rate) were opened and the flow rate was varied by adjusting the fan speed using the variable speed drive. The software used to communicate with the data logger allows the samples to be averaged over a time period (the user manually decides when the appropriate integration period has been reached). Before the data was collected, the system was allowed to run at maximum speed for about 15 minutes to allow all bearings and motors to warm up to steady temperatures. Before the data sampling was initiated, it was crucial to allow the pressures to settle after every fan speed change or nozzle selection change. Once the pressures stabilized, the averaging for the specific data point was commenced. Once the data collection was completed three times at the same operational points (nozzle and fan speed), the readings were corrected using a 'zero' reading that was taken right after the warm-up run.

The corrected data was then fed into equations A.1 to A.4 in a spreadsheet created using Microsoft Excel 2007. Using the Excel iterative solver, the cyclic referencing referred to in Section A.1 could be solved using a 0.0001 convergence criteria. It was now possible to correlate an anemometer voltage output to a mass flow value. Since fan performance curves are normally defined in terms of volume flow rate, it was desirable to convert the mass flow value into a volume flow value (at a specific density – crucial for non-dimensional fan performance scaling laws) which was easily accomplished by using the static air pressure at the anemometer and air temperature to determine the air density at the anemometer.

Figure A.4 shows the three calibration data points, an averaged data point set (all three measured data sets), and the linear trend line fitted to the averaged data point set.

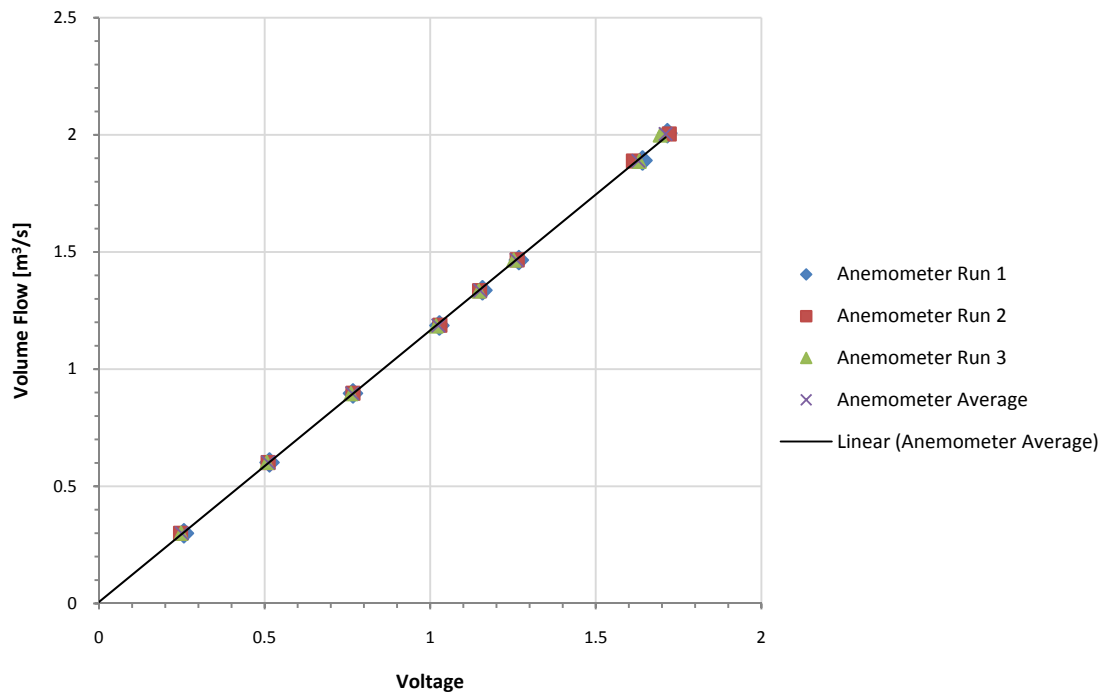


Figure A.4 Measured data point sets with linear curve fit

### A.1.4 Conclusion

The data sets in general show good repeatability. Some minor fluctuations are visible at the highest flow rates, however these variations are very small and the effect of these minor variations is even further reduced when the three data sets are averaged. These minute variations might have been caused by movement near the inlet of the tunnel, draughts in the laboratory, or flexing of tunnel walls due to the low  $p_{up}$  pressures at high flow rates.

Given the prior knowledge about the propeller anemometer, a few key operational characteristics were known and were used to judge the validity of the calibration data and curve fit. Firstly, it was known that the anemometer cannot generate a voltage output if the propeller is not turning, hence the data sets and curve fit should cross through zero on both the flow rate axis and voltage output axis. Secondly, the speed of the anemometer increases

proportionally to the increase in volume flow rate, thus the data sets should have a linear behaviour. From Figure A.4 it can be verified that both these 'requirements' were met within very tight margins. Most of the testing on the actual experiment will be done in the 1.5 – 2  $m^3 / s$  region and at 2  $m^3 / s$  the y-axis intersect represents a mere 0.3 % error. It can also be seen that a linear curve fit represents the data set to within 0.005 % (square-root of  $R^2$  where  $R^2$  is the 'squared error') margin and thus validates that the anemometer behaviour is indeed perfectly linear as expected.

Thus, from this calibration process it was determined that the output response of this propeller anemometer - as fixed in the bellmouth-pipe assembly shown in Figure A.1 - can be defined as:

$$\dot{V}_{anemo,ref} = 1.159591 \cdot V_{anemo,ref} + 0.006278 \quad (A.8)$$

Note that the since the anemometer will serve as a reference anemometer to calibrate other anemometers, the equation has been defined to output the volume flow rate using the voltage output from the anemometer so that the volume flow rate of this reference anemometer can be directly correlated with the voltage output of the anemometer which is being calibrated, or be used to calculate mass flow and calibrate according to conservation of mass principles.

## **A.2 CALIBRATION OF TUNNEL ANEMOMETERS**

The reference anemometer calibrated in Section A.1 can now be used to calibrate the individual anemometers in the test tunnels.

### **A.2.1 Calibration Setup**

The calibration of the tunnel anemometers was very simple. The reference anemometer was placed at the exit of the tunnel and firmly clamped in place to ensure no leakage occurs between the tunnel anemometer and reference anemometer. Initial runs using the fans in the tunnels indicated that the addition of the reference anemometer increased the system

resistance to such an extent that the desired volume flow rate of  $\sim 2 \text{ m}^3/\text{s}$  could not be achieved. Thus, the tunnel fan was removed and flow was sucked through the tunnel using an axial fan unit containing two counter-rotating 480 mm axial flow fans which are powered by a 3.7 kW motor each. Flow control was achieved using a throttle at the exit of the dual-fan unit.

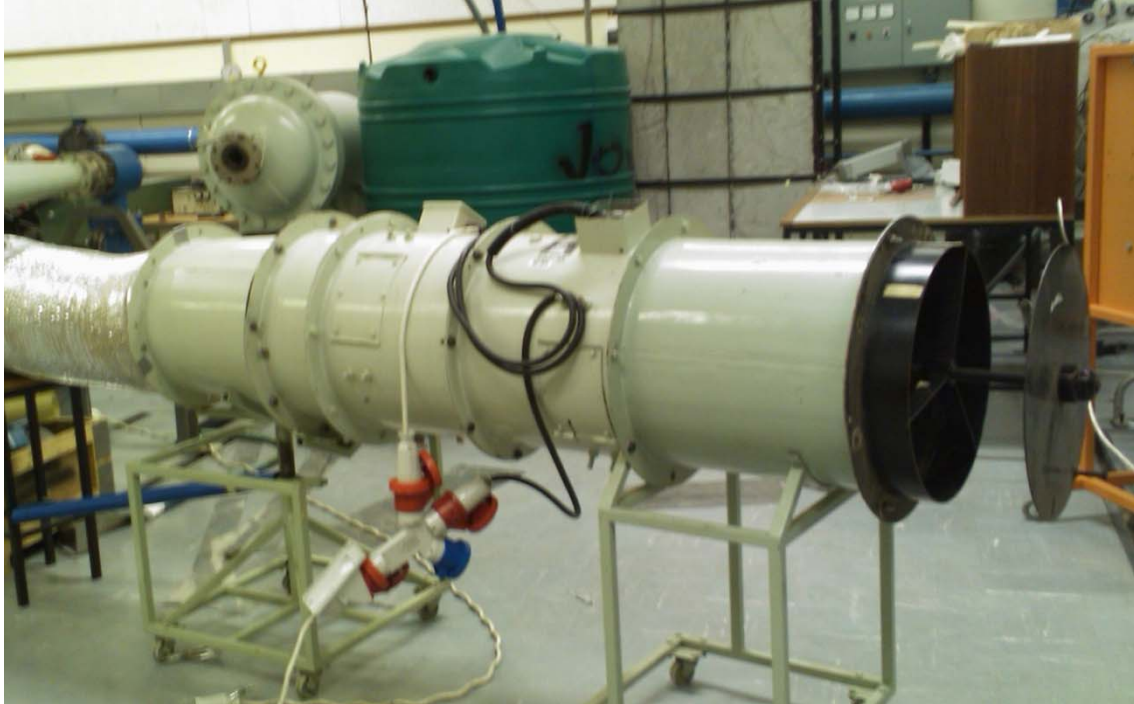


**Figure A.5** Dual-fan unit with flow control throttle

Data logging was done using a National Instruments NI-6218 DAQ unit capable of handling up to 31 analogue inputs. The voltages from the pressure transducers and anemometers were captured using a custom created LabView 8.5 interface which read the channel data from the DAQ, performed averaging, and output the averaged data for the total sampling period to a .csv file. The computer running the LabView environment was running on a Windows XP Home Edition operating system and also featured Microsoft Office 2003.

Pressure transducers measured the mean static pressure at a series of circumferential pressure tabs at both the reference and tunnel anemometers. The static pressure difference (relative to atmospheric) could then be used to determine the density at each anemometer. The volume flow calibration curve obtained for the reference anemometer in Section A.1 was simply applied to the averaged voltage output by the LabView 8.5 interface and multiplied by the local density to obtain a mass flow rate through the reference anemometer, and

subsequently the tunnel anemometer too. This calculation process was reversed at the tunnel anemometer to obtain the equivalent volume flow calibration curve.

### **A.2.2 Pressure Transducer Calibration**

Since the accuracy of the anemometer calibration depends on the accuracy of the mass flow calculations for the reference anemometer, the calibration of the pressure transducers is of critical importance. These pressure transducers will later be used to determine key fan characteristics like fan static pressure rise from which the fan static efficiency can be calculated, and the accuracy of these characteristics will also depend on the accuracy of the pressure transducer calibration.

A total of ten pressure transducers were available and connected despite only two being used for the calibration of the anemometers. Since these pressure transducers will be used for the actual testing, all ten were calibrated in one procedure in order to ensure continuity. The process followed was similar to that in Section A.1.2 and consisted of applying a vacuum to the pressure transducers using a Betz manometer and matching the output voltages from the pressure transducers to a 'mm water' reading on the Betz. The 'mm value' can be converted to a pascal reading by taking water's density and the locations gravitational acceleration into account. The pressure transducers are all identical (zero pressure output voltages differ from unit to unit but the internals for every unit are identical) and all work by measuring the variation in capacitance caused by the displacement of a diaphragm due to relative pressure fluctuations. The pressure transducer units have a range of 0 – 1000 Pa. The units are grouped in clusters of five to form two 'banks' of pressure transducers. Each bank also contains a 24V DC power supply unit which powers the five pressure transducers. The readings from the diaphragm is linearized and normalized inside the pressure transducer and output as a 0 – 10 V DC voltage (with the 'zero'-pressure voltage close to 1 V).



Using the methods described, each pressure transducer's calibrated equation was found to be:

**Bank 1:**

$$P_1 = 111.49208868 \cdot V_{p1} - 99.89660032 \quad (\text{A.9})$$

$$P_2 = 111.85292543 \cdot V_{p2} - 118.79244966 \quad (\text{A.10})$$

$$P_3 = 111.29384504 \cdot V_{p3} - 113.49867498 \quad (\text{A.11})$$

$$P_4 = 111.73403006 \cdot V_{p4} - 112.82263289 \quad (\text{A.12})$$

$$P_5 = 111.22425904 \cdot V_{p5} - 114.18282739 \quad (\text{A.13})$$

**Bank 2:**

$$P_6 = 111.37582325 \cdot V_{p6} - 109.68318050 \quad (\text{A.14})$$

$$P_7 = 111.76472298 \cdot V_{p7} - 110.02532450 \quad (\text{A.15})$$

$$P_8 = 111.41357112 \cdot V_{p8} - 111.07590214 \quad (\text{A.16})$$

$$P_9 = 110.87008968 \cdot V_{p9} - 102.02176038 \quad (\text{A.17})$$

$$P_{10} = 111.17672834 \cdot V_{p10} - 95.31593403 \quad (\text{A.18})$$

With  $V_p$  in Volts

The linear curve fits on all ten pressure transducers result in error-squared ( $R^2$ ) values of at least 0.9999 and thus agrees very well (perfect fit being  $R^2 = 1$ ) with the internal linearization of the pressure transducers. Also, all the gradients are very close (less than 1% variation) with the only significant differences being the y-offset where the y-offset represents the difference in 'zero' reading voltages as mentioned earlier.

### A.2.3 Test Data

Following the completion of the calibration of the pressure transducers, the volume flow through the reference anemometer and tunnel anemometers could be compared. As mentioned earlier, the tunnel's own fan could not provide sufficient flow and thus the dual-fan unit was used. To ensure precision and reliability each tunnel's calibration was performed twice.

Similar to the reference anemometer, the output voltage from the tunnel anemometers increase linearly with volume flow and thus for no flow, the output voltage should be zero volts.

The test procedure was relatively simple: the reference anemometer was clamped to the exit of the tunnel (as shown in Figure A.6) and connected with the dual-fan unit using a flexible pipe. Critical to this fixture was ensuring that no leakage occurred between the reference anemometer and the tunnel anemometer, and to assist the seal a self-adhesive foam lining was stuck onto the perimeter of the reference anemometer's bellmouth.

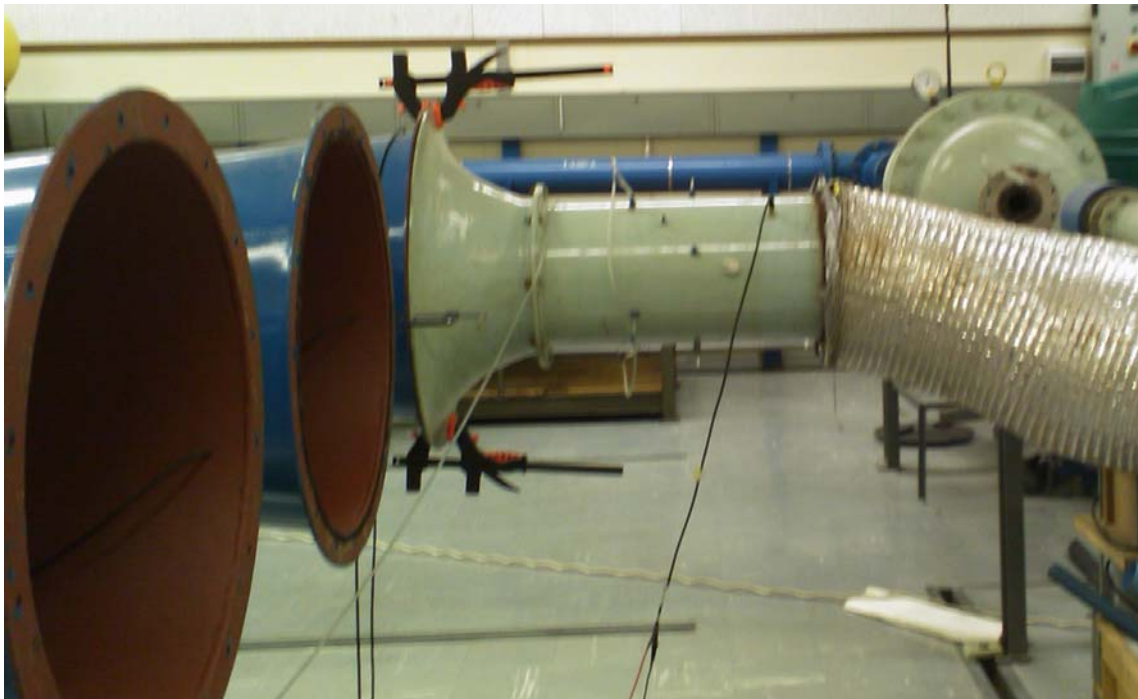


**Figure A.6** Reference anemometer clamped to tunnel outlet

The circumferential pressure taps of the reference anemometer were always connected to  $P_1$  while the circumferential pressure taps for the tunnel anemometers were always connected to  $P_2$ . For each tunnel, flow was sucked through the system for ten to 15 minutes to allow all the components to reach operating temperature. After the warm-up period, the system was shut down (wait for all fans and anemometers to come to a rest) and a 'zero' reading was taken. The system was then started up again at full throttle opening and testing commenced. Including the full throttle opening, a total of seven data points were taken at different throttle openings. The flow sensitivity to the throttle opening appeared to follow an exponential

behaviour and thus the number of turns per setting (the throttle plate moved on a threaded rod) was decreased in such a way to maintain a relatively constant decrease in flow per setting. Once a data set was complete, the system was shut down again and the 'zero' reading for the next data set was taken.

The whole process was repeated for each tunnel.

For data manipulation, Excel 2007 was used. For every voltage reading, the 'zero' reading was subtracted to obtain the true zero value. Using the curve fit obtained in Section A.1 for the reference anemometer and the densities at the anemometers obtained from the static pressure readings, the conservation of mass principle was applied to obtain a volume flow curve for each tunnel anemometer from the volume flow curve of the reference anemometer.

Figure A.7, Figure A.8 and Figure A.9 are the data set curves obtained for each run of each tunnel.

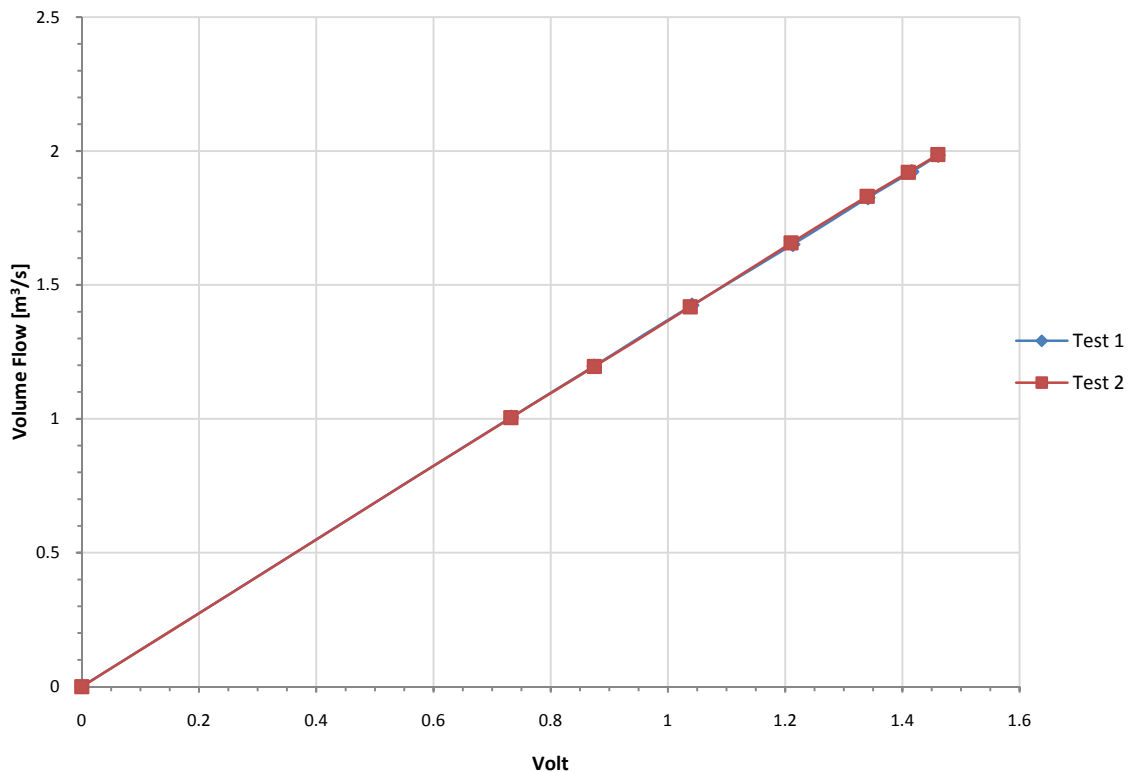
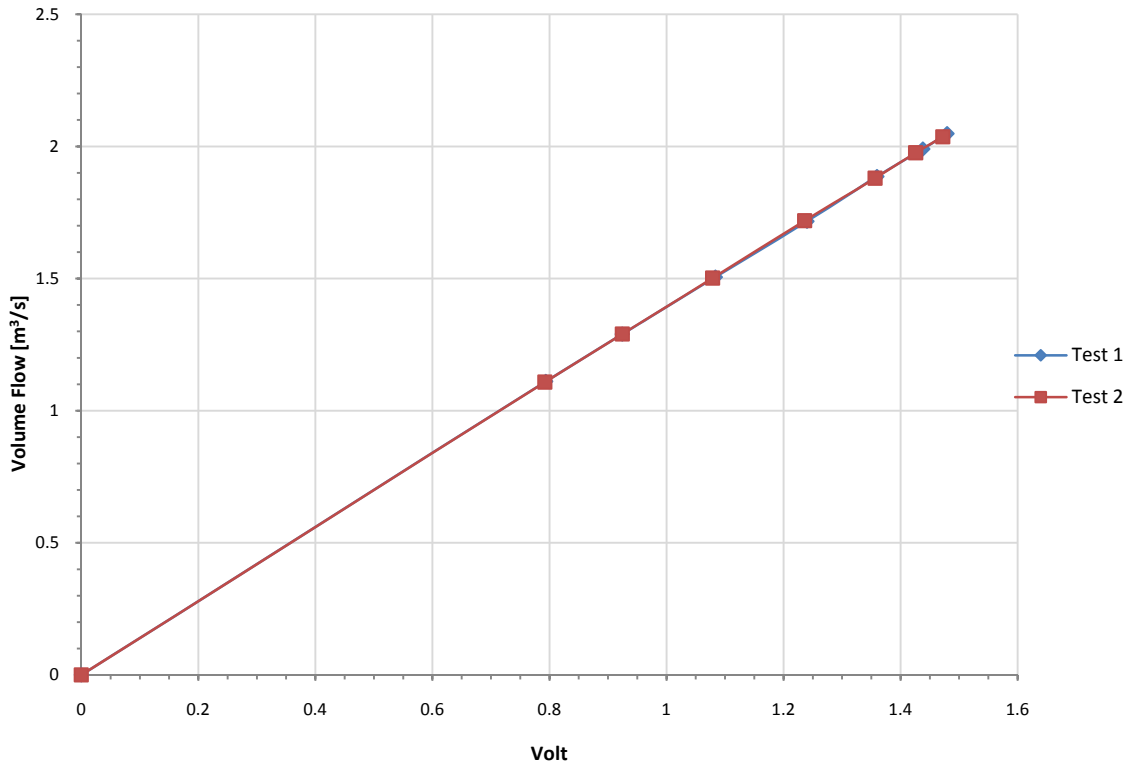
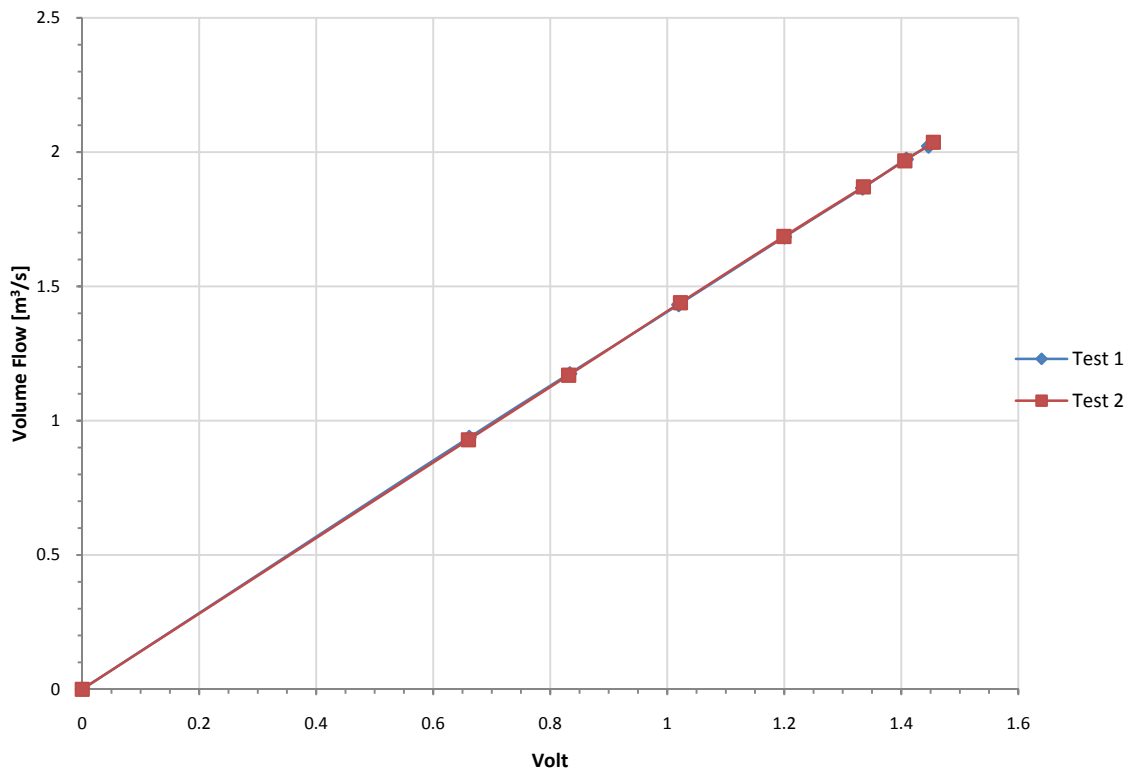


Figure A.7 Tunnel anemometer calibration curves for Tunnel 1



**Figure A.8** Tunnel anemometer calibration curves for Tunnel 2



**Figure A.9** Tunnel anemometer calibration curves for Tunnel 3

## A.2.4 Conclusion

Since the throttle positioning was a manual process, it would not be sound practise to simply average the data points for each tunnel's two data sets as there is no guarantee that the throttle positions were exactly the same (although very good repeatability was obtained). Thus, it was considered better practise to instead average the gradients and y-intercepts for each data set's linear curve fit.

**Table A.1** Anemometer calibration curves

<b>Tunnel 1</b>	$\dot{V}_{anemo1a} = 1.356935 \cdot V_{anemo1a} + 0.006088$	$\dot{V}_{anemo1} = 1.3594305 \cdot V_{anemo1} + 0.004798$ (A.19)
	$\dot{V}_{anemo1b} = 1.361926 \cdot V_{anemo1b} + 0.003508$	
<b>Tunnel 2</b>	$\dot{V}_{anemo2a} = 1.382780 \cdot V_{anemo2a} + 0.005566$	$\dot{V}_{anemo2} = 1.3831935 \cdot V_{anemo2} + 0.005684$ (A.20)
	$\dot{V}_{anemo2b} = 1.383607 \cdot V_{anemo2b} + 0.005802$	
<b>Tunnel 3</b>	$\dot{V}_{anemo3a} = 1.396888 \cdot V_{anemo3a} + 0.006457$	$\dot{V}_{anemo3} = 1.398298 \cdot V_{anemo3} + 0.005008$ (A.21)
	$\dot{V}_{anemo3b} = 1.399708 \cdot V_{anemo3b} + 0.003559$	

The data sets for each tunnel show very good repeatability despite manual throttle positioning. The curve fits all have  $R^2$  of at least 0.9999, confirming very good curve fit and prior knowledge that the anemometers have a linear behaviour. Considering the anemometers cannot generate an output while stationary, it was expected that the calibration curves would have a zero y-axis intercept. The linear curve fits came very close to zero and the average error due to the non-zero intercepts represent a mere 0.3% error when considering the offset from the gradient.

## A.3 TORQUE TRANSDUCER CALIBRATION

For this investigation, the edge fan in the experimental features a torque transducer which can be used to obtain an insight into the influence of the loading and power required by the edge fan under distorted inflow conditions.

### A.3.1 Calibration Setup

As with the calibration of the anemometers, a known load needs to be applied and then used to gauge the output of the device to the corresponding load. Thus, a known torque needs to be applied.

The simplest way to do this would be to make use of a moment arm, where the moment arm is defined as

$$M_o = F \cdot L \quad (\text{A.22})$$

where  $F$  is a known force and  $L$  is the lever distance between the applied force and axis of bending. To this end, a simple jig was constructed with mild steel and where  $L$  is known and fixed. The purpose of the jig was to allow the application of a force at a known distance using weights of known mass. Knowing what the applied mass was, and the gravitational acceleration, the applied force could be determined. Combining the known force with the known lever distance, the moment arm, or torque, could be easily determined and correlated to a voltage output from the torque transducer. In this case, the lever distance is 250 mm.

The torque transducer is placed in-line between the motor shaft and the fan shaft. The alignment of two solid shafts is notoriously difficult and even minor misalignment could damage the torque transducer. In order to assist in joining the motor shaft and the fan shaft while position the torque transducer in between, alignment couplings were used on either side of the torque transducer. These couplings are capable of handling misalignment in two planes while still being able to transmit torque.

The torque transducer features a full-bridge strain-gauge assembly which measures the strain on the circumference of the torque transducer's shaft. The readings from the strain-gauges

are communicated to the onboard amplifier and rectifier via slip-rings that allow an uninterrupted signal despite the shaft turning and the rest of transducer being stationary. As mentioned, this torque transducer features an onboard amplifier and rectifier which outputs a  $-5\text{ V}/+5\text{ V}$  signal, thus eliminating the use of often bulky spiders and amplifiers and allowing the output from the torque transducer to be directly connected to any data logger. Given how the strain-gauges operate, an excitation voltage is required. For this torque transducer, the excitation voltage can be anything from  $11.3\text{ V} - 35\text{ V}$ . In order to ensure ease-of-use and as a safety measure (connecting the excitation voltage to the output pins could have disastrous effects), a connectivity box was assembled that houses a  $12\text{ V}/300\text{ mA}$  power supply unit and features connectivity for the torque transducer cable [4-pin (2 pins excitation voltage and 2 pins output voltage) box side and 25-pin torque transducer side],  $230\text{ V}$  power connectivity (for power supply) and a coaxial output for the voltage to the data logger. Each connector can only be connected in one way.

Data logging was done using a National Instruments NI-6218 DAQ unit capable of handling up to 31 analogue inputs. The voltage from the torque transducer was captured along with the outputs from the pressure transducers and anemometers using a custom created LabView 8.5 interface which read the channel data from the DAQ, performed averaging, and output the averaged data for the total sampling period to a .csv file. The computer running the LabView environment was running on a Windows XP Home Edition operating system and also featured Microsoft Office 2003.

A laboratory scale was used to determine the mass of the tray onto which the weights will be placed, as well as the weights themselves. The scale is accurate to  $1\text{ g}$ .

### **A.3.2 Test Data**

A water level was used to bolt the jig to the fan shaft in a perfectly horizontal position as shown in Figure A.10. This was done to ensure that the applied force would act perfectly perpendicular (gravity is straight down) to the lever arm and allow the use of Equation A.23 without any compensation for angular components. The motor shaft was clamped in place using a grip wrench. Note that the jig is perfectly symmetrical and allows the moment to be

applied in either the clockwise or counter-clockwise direction. It is expected that the torque transducer will have a perfectly linear behaviour irrespective of the direction of applied torque, but this needs to be verified, hence the ability to test in both directions.

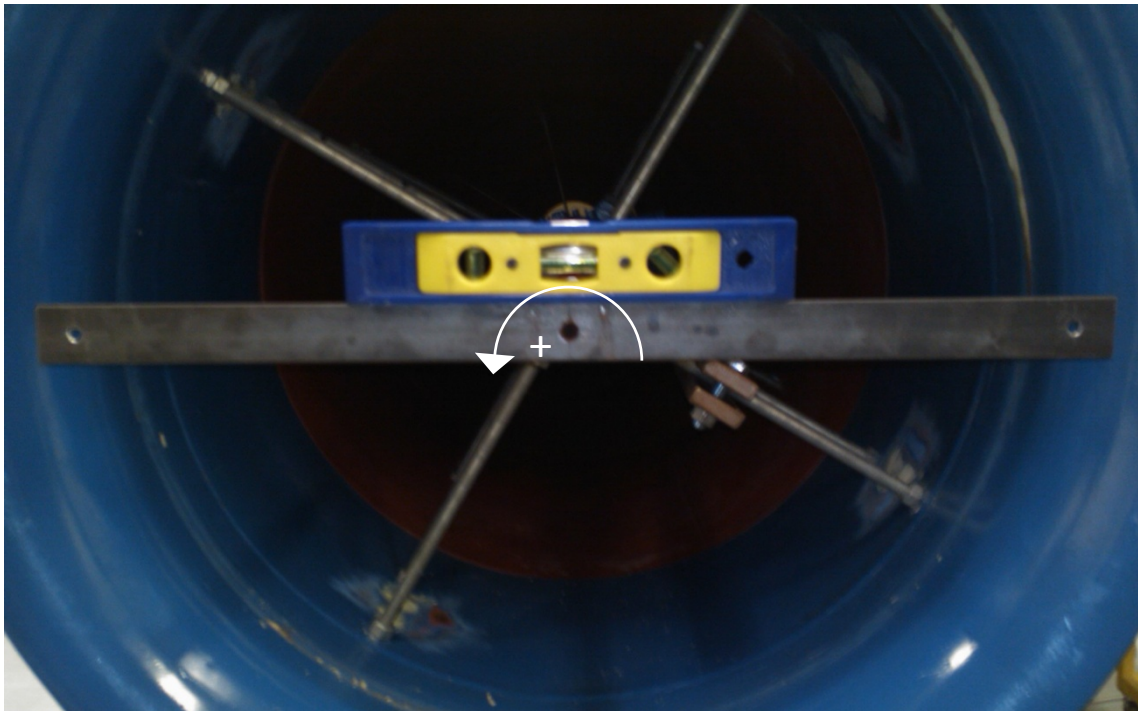


**Figure A.10** Positioning of torque transducer calibration jig

Once the jig and motor shaft was firmly secure, the tray was hung from the jig (bolted to jig at ends) and the weights were added incrementally. The rated power of the motor is 750 W and the rated speed is 1440 rpm, and using

$$P = \omega \cdot T \quad (\text{A.23})$$

it was determined that the motor needs to be able to output ~5 Nm at full load and rpm. The aim was thus to calibrate up to 5 Nm or as close as possible to 5 Nm.

It is very important to take the initial, or 'zero', reading as this reading will determine if and how large any offset might be. It was also verified that the installation of the jig onto the shaft does not influence this 'zero' reading as this would have complicated the calculations. Ideally, the 'zero' reading should be zero but as seen with the calibration of the pressure transducers, the excitation voltage and presence of electrical amplifiers and circuitry on the device itself tends to cause some minor travel from the 'ideal' scenario.



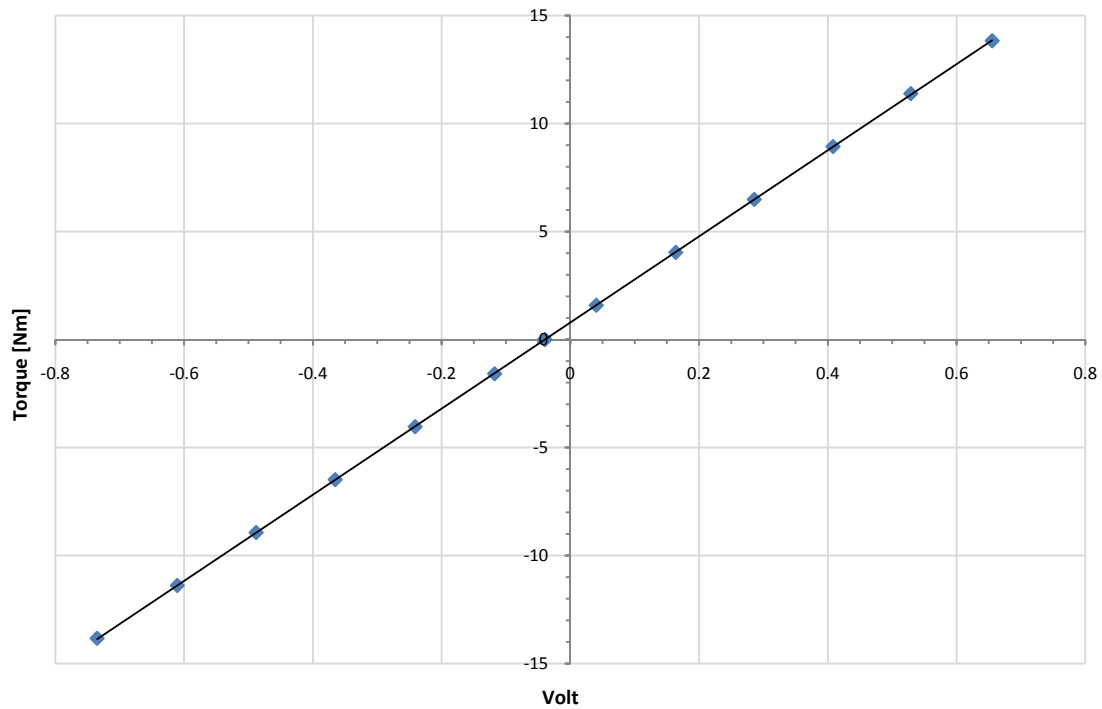


Figure A.11 Torque transducer calibration curve

Figure A.11 shows the combined calibration curves of both directions of applied moments as well as a linear curve fit through the data points.

### A.3.3 Conclusion

As seen in Figure A.11, the torque transducer has a linear and symmetric (direction of torque) response. The internal amplifier and rectifier are thus very effective at amplifying and transforming the strain-gauge output into a more measureable size.

Note that the curve does not intersect the zero of the axis and although this is not ideal, it is not entirely unexpected (as explained earlier) and appears very consistent for this setup. The linear curve fit is almost perfect and represents a less than 0.2 % error for the entire fit ( $R^2 = 0.999993$ ). The calibration was done up to and exceeding the expected torque range but was still less than 1/5<sup>th</sup> of the rated torque for the transducer ( $\sim 1 \text{ V} / 5 \text{ V FS}$ ).

Thus, for all future use of this torque transducer, the transducer's response can be defined as

$$T_{transducer} = 19.932565 \cdot V_{transducer} + 0.790974 \quad (\text{A.24})$$

## **APPENDIX B: FAN GEOMETRY AND PERFORMANCE DATA**

The two primary fans used in this thesis are referred to as the N fan and the B2 fan. These fans vary greatly in geometry, solidity and behaviour as detailed in this appendix.

### **B.1 N FAN**

The N fan is installed in large-scale cooling arrays found at power stations and other plants and is therefore the best representation of large-diameter fans in operation in South Africa at the moment. A typical installation utilizes a 9145 mm fan which operates at a rotational speed of 125 rpm and a blade angle ( $\alpha$ ) of  $14^\circ$ . The casing diameter varies depending on the type of inlet bell (rounded, cylindrical) and manufacturing accuracy but for this specific power station application with a rounded inlet casing, the nominal casing diameter is 9216 mm as opposed to the 9240 standard casing from the manufacturer. The eight fan blades per fan were manufactured from glass fibres and a polyester resin system using a wet-layup technique. The hub is a simple steel plate with 'beds' in which the root of the blades rest and are fastened to the hub using two U-bolts per blade. For the N fan, the blade angle is measured at the tip of the blade, along a tangential line between the belly of the blade and the trailing edge, relative to the plane of rotation.

#### **B.1.1 Fan Geometry**

Since the N fan is a commercial fan, not much information regarding the geometry of the fan was available as this could have compromised the manufacturer's competitiveness. However, in 1987 Stellenbosch University commissioned 'Oblivius Industrial' to measure an N fan blade. The resulting unpublished report contained a data point scatter of the cross-section of the blade at various radii. The absolute blade angle was determined along with the blade chord length and blade thickness. Figure B.1 illustrates a stacked view of a selection of the blade cross-sections to show how the blade angle varies with radius. Note that the blade angles are relative to the measurement reference axis (located at cross-section S) and are thus not at the same inclination as they would be when mounted on the fan hub. Also note that the stacked

view only contains the cross-sections of the 'working' blade and not the part of the blade that increases in cross-section from the root cross-section to where the blade begins. Figure B.2 shows how the absolute blade angle varies with radius if the blade is set to a 14° setting.

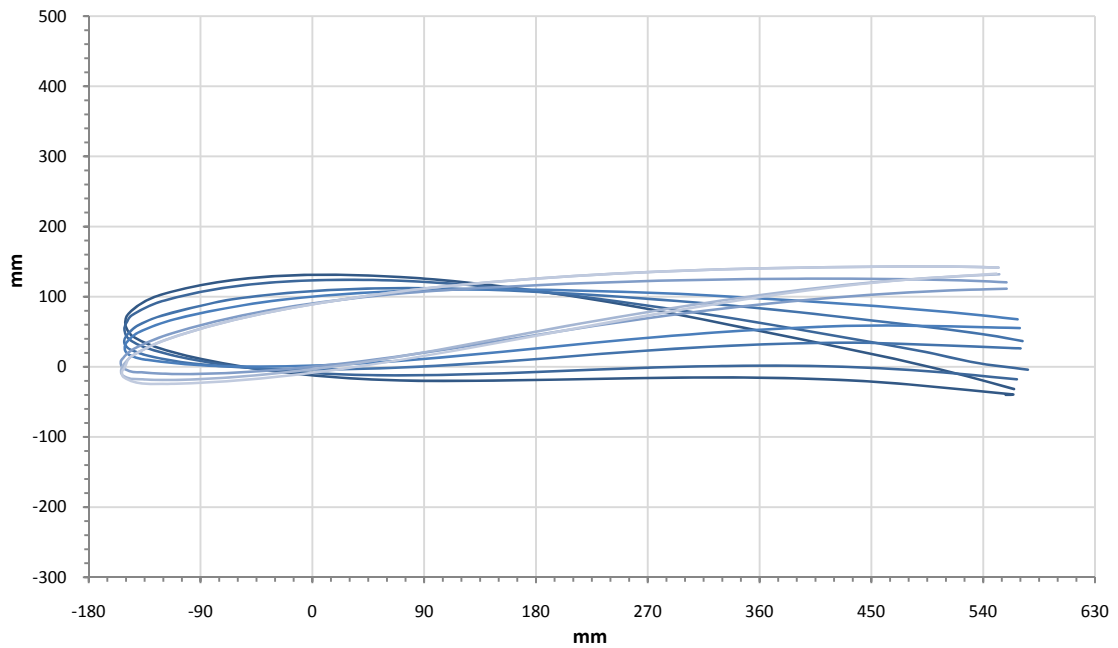


**Figure B.1** Measured cross-section scatter of 9415 mm N fan

Figure B.3 illustrates how the blade actually thins towards the tip. The blade thickness is non-dimensionalized using the chord length of the blade, thus allowing the blade thickness at a certain radius to be expressed as a percentage of the chord length. The chord length for the N fan blade can be considered constant at 721 mm (this may vary by up to 1.5 mm as a result of manufacturing accuracy).

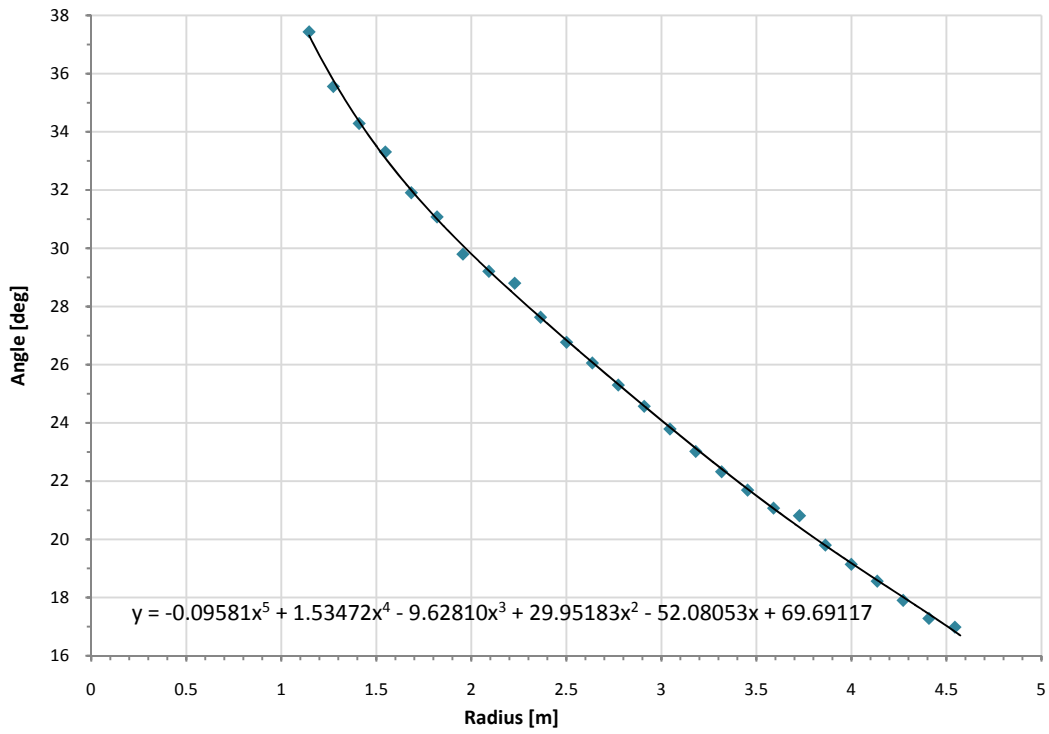


Figure B.2 Measured blade angle as function of radius

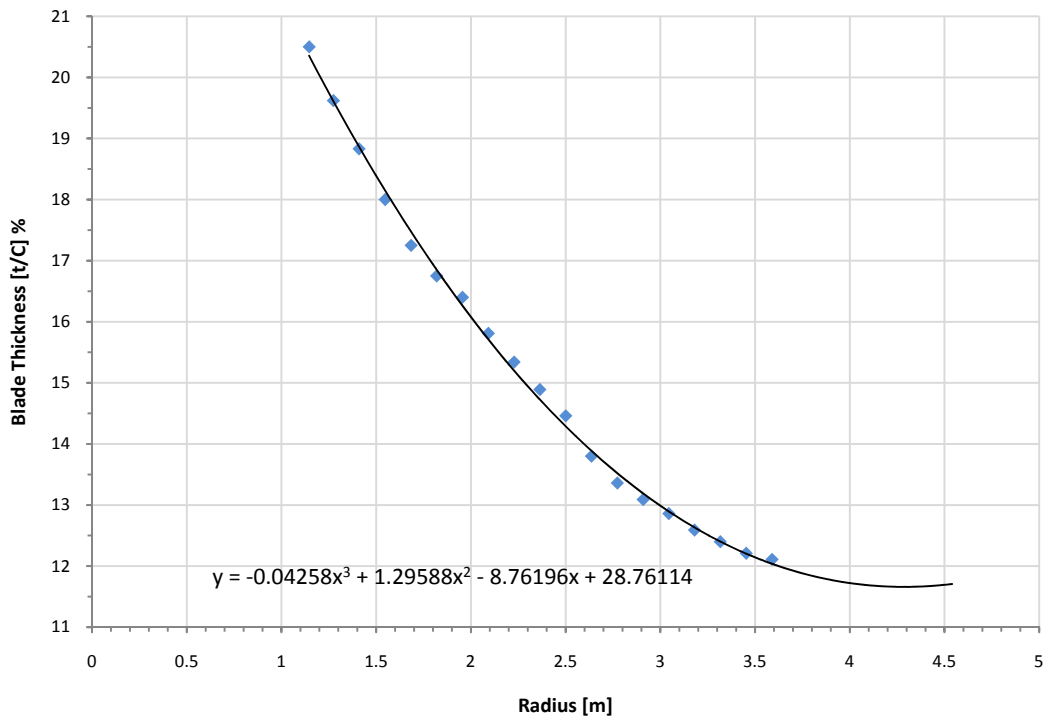
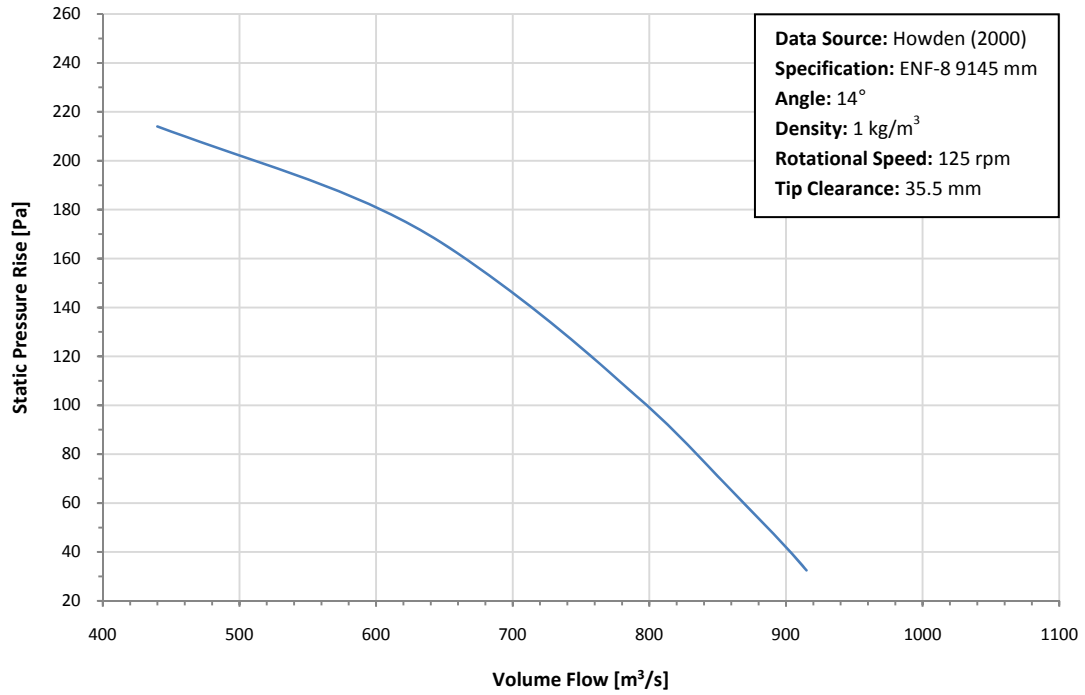


Figure B.3 Measured blade thickness as function of radius and chord length

### B.1.2 Fan Performance

Figure B.4 shows the fan static pressure rise for a 9145 mm fan rotating at 125 rpm as the volume flow through the fan varies.



**Figure B.4** N fan static pressure rise curve

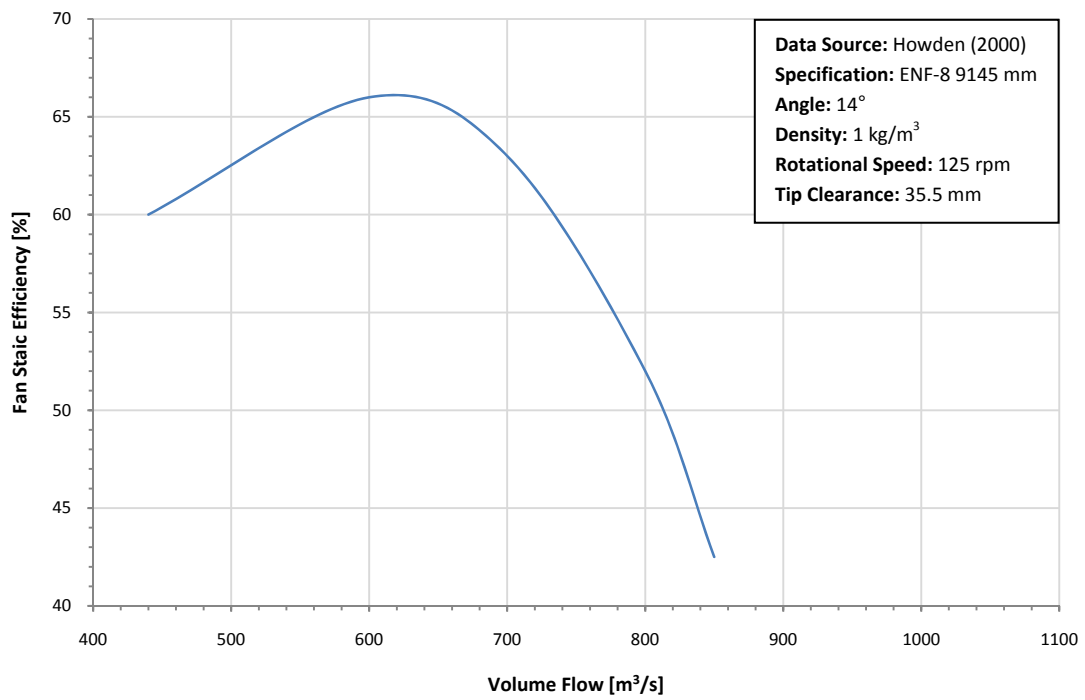
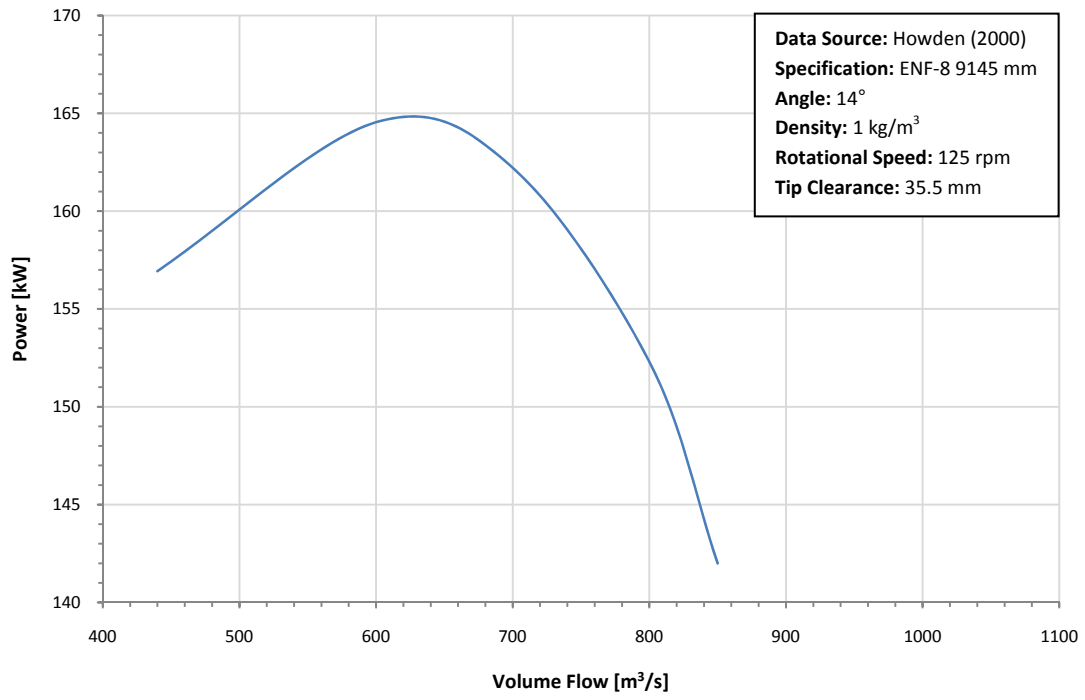


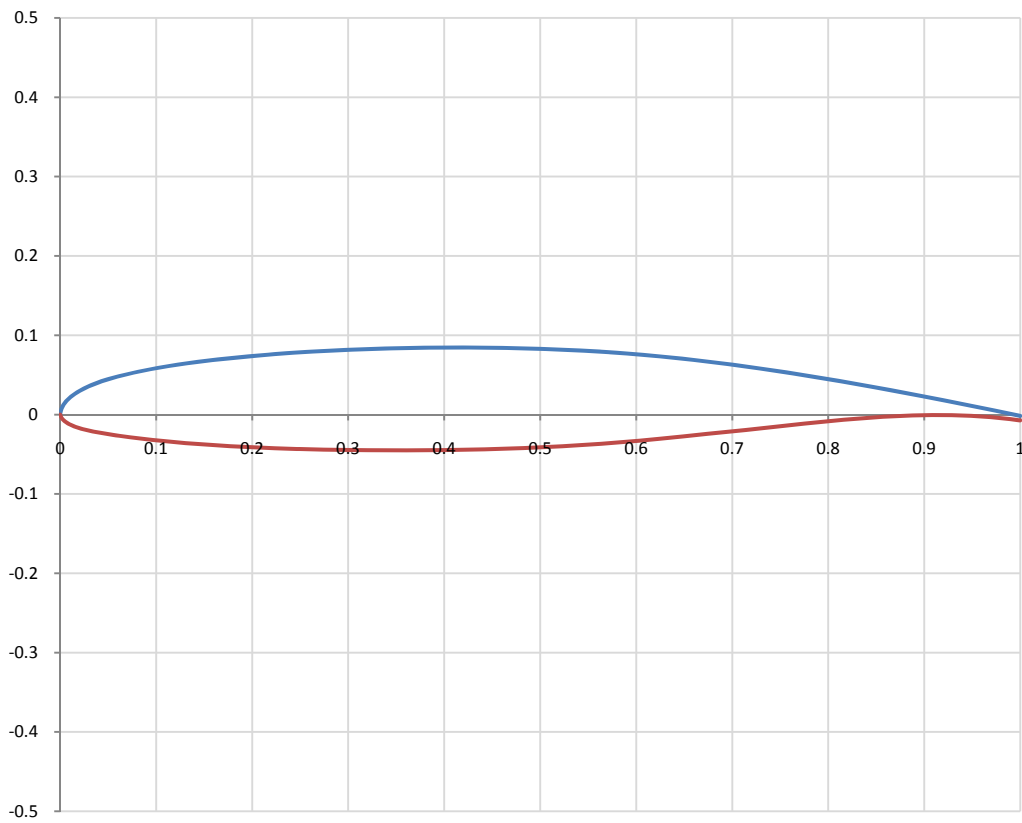
**Figure B.5** N fan static efficiency curve

## **B.2 B2 FAN**

In the work of Bruneau (1994), he designed and experimented with two fan blade designs, B1 and B2, and compared their performance (all aspects) to that of fans in use in large fan arrays at the time. The B1 blade design is based on the Clark-Y profile and the B2 blade design is based on the NASA GA(W)-2 profile. The NASA GA(W)-2 profile was selected based on its good lift/drag characteristics and promised good off-design performance (Bruneau, 1994). The B2 design was thus the design of choice for most work based on or related to Bruneau's investigation. The B2 fan was tested by Bruneau at a rotational speed of 750 rpm. He performed several tests at various blade angles, but his performance comparisons were all done at a blade angle of 31°. The blade angle of the B2 fan is measured at the hub of the blade along the chord line of the blade section relative to the plane of rotation. He also did performance comparisons (all aspects) for both the B1 and B2 fans for sealed and non-sealed roots. Some gains were seen when adopting a sealed root and thus a 'sealed root design' was also adopted for this investigation.

### **B.2.1 Fan Geometry**

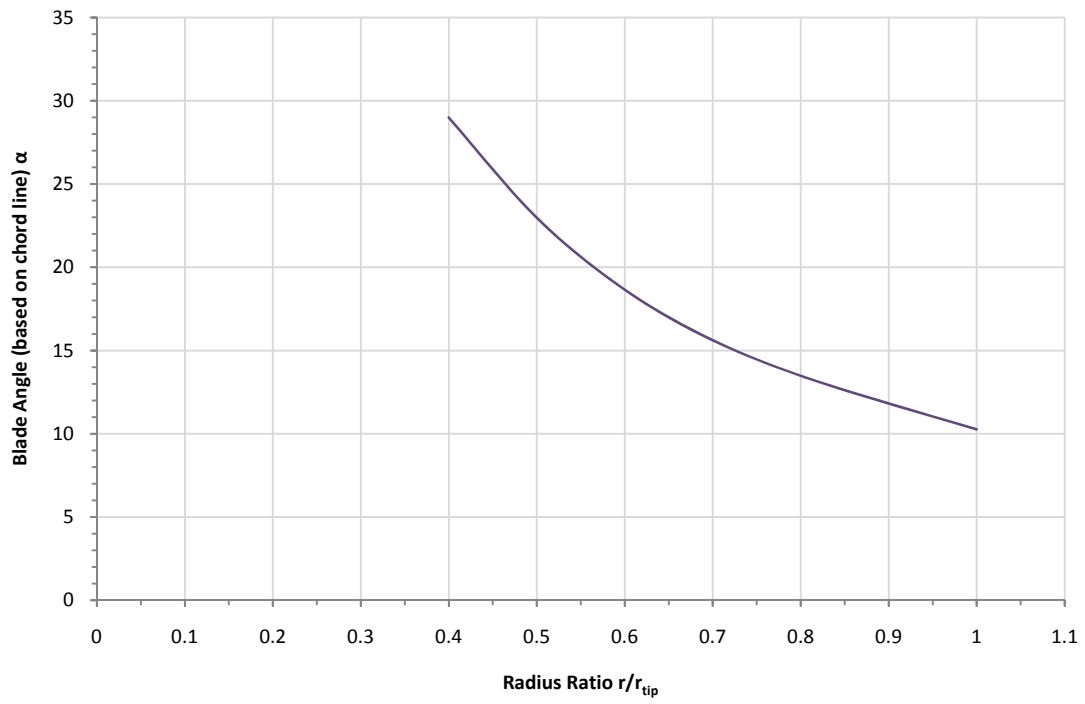
Both the B1 and B2 designs have a 13% thickness/chord ratio at the root which linearly (with radius) decreases to 9% at the tip. The 13% profile data was obtained from a NASA Technical Memorandum released for public availability in 1977 (McGhee et al., 1977) and contains a non-dimensional scatter of the upper and lower halves of the NASA profile. The 9% profile, as well as the intermediate profiles at increasing radii, was obtained by scaling the thickness of the 13% profile. The scaling was performed from each profile's camber line by first obtaining the 13% profile at the appropriate chord length (chord length also decreases linearly with radius) and then reducing the thickness from the chord length. Figure B.6 shows the non-dimensional 13% NASA GA(W)-2 profile.



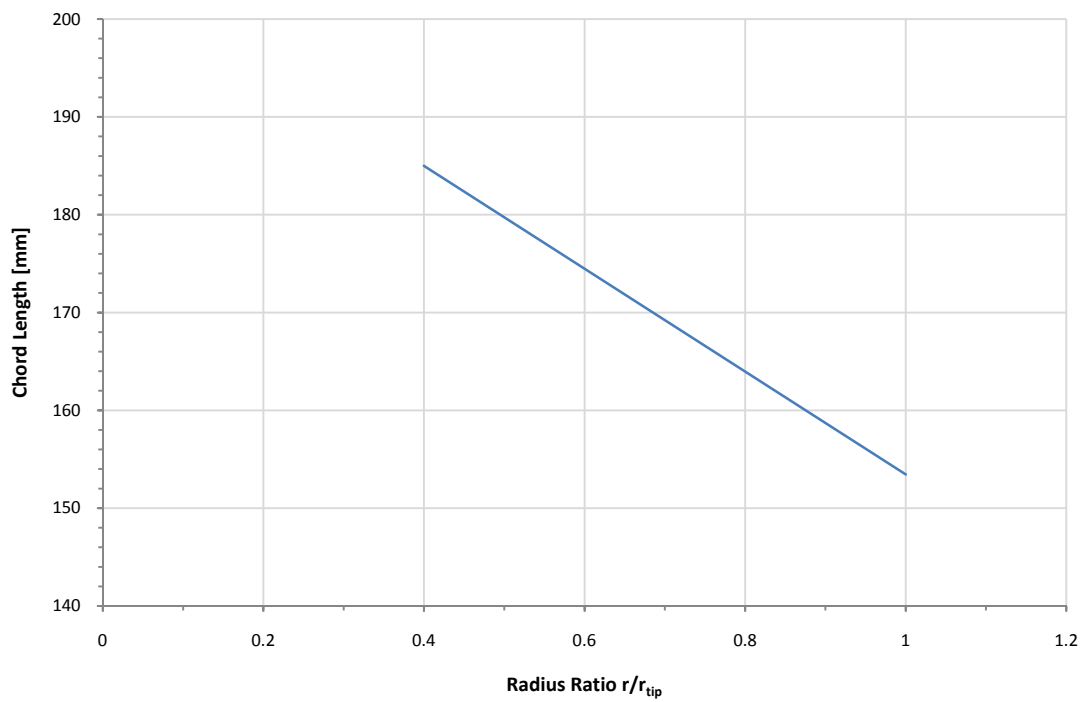
**Figure B.6** Section profile for NASA GA(W)-2 airfoil (McGhee et al., 1977)

Figure B.7 illustrates how the blade angle varies (for a blade setting angle of  $29^\circ$ ) as a function of radius ratio and the linear decreasing chord length of the B fan design can be seen in Figure B.8 (Meyer & Kröger, 2001).





**Figure B.7** Blade Angle,  $\alpha$ , as a function of  $r/r_{tip}$



**Figure B.8** Chord length as function of  $r/r_{tip}$

## B.2.2 Fan Performance

The performance (fan static, efficiency and power) curves for the B2 fan was determined by Bruneau (1994) for his 1542 mm prototype featuring a sealed root (SR) and nose cone (NC) [SR + NC = SN]. The fan curves for a variety of fan blade angles can be seen in Figure B.9, Figure B.10 and Figure B.11.

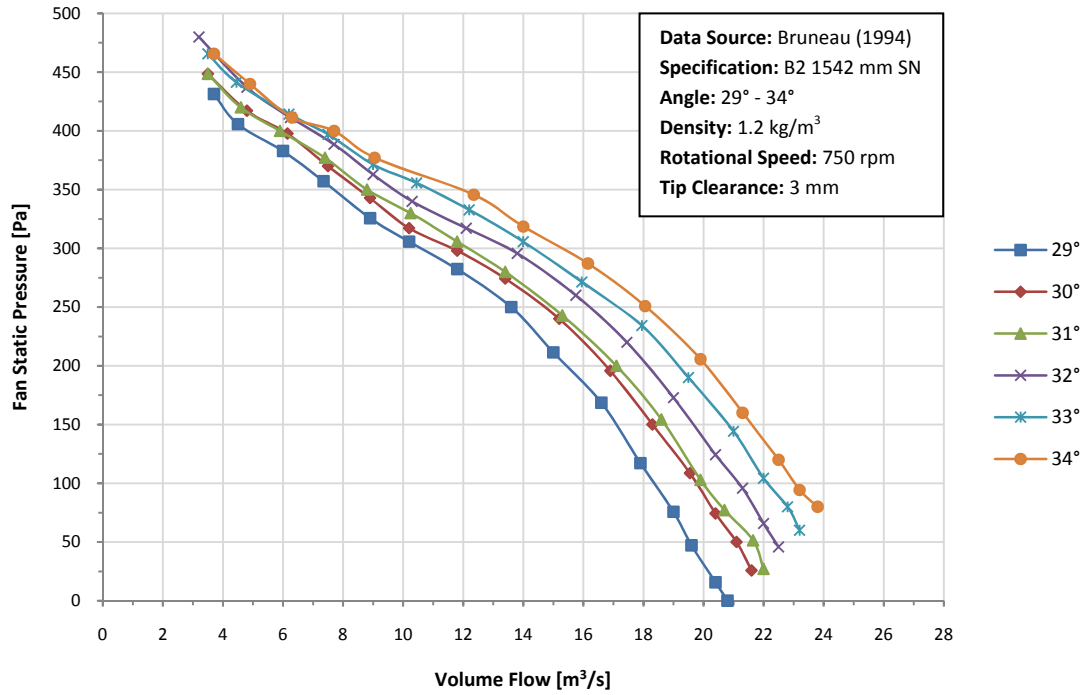


Figure B.9 B2 fan static pressure rise curve

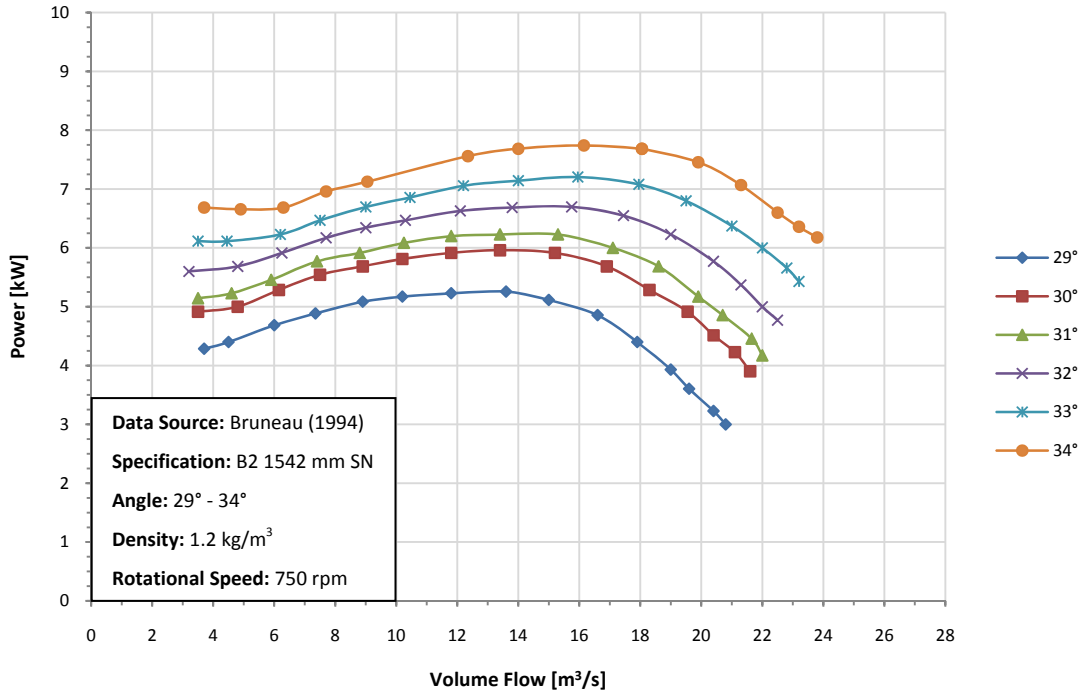


Figure B.10 B2 fan shaft power curve

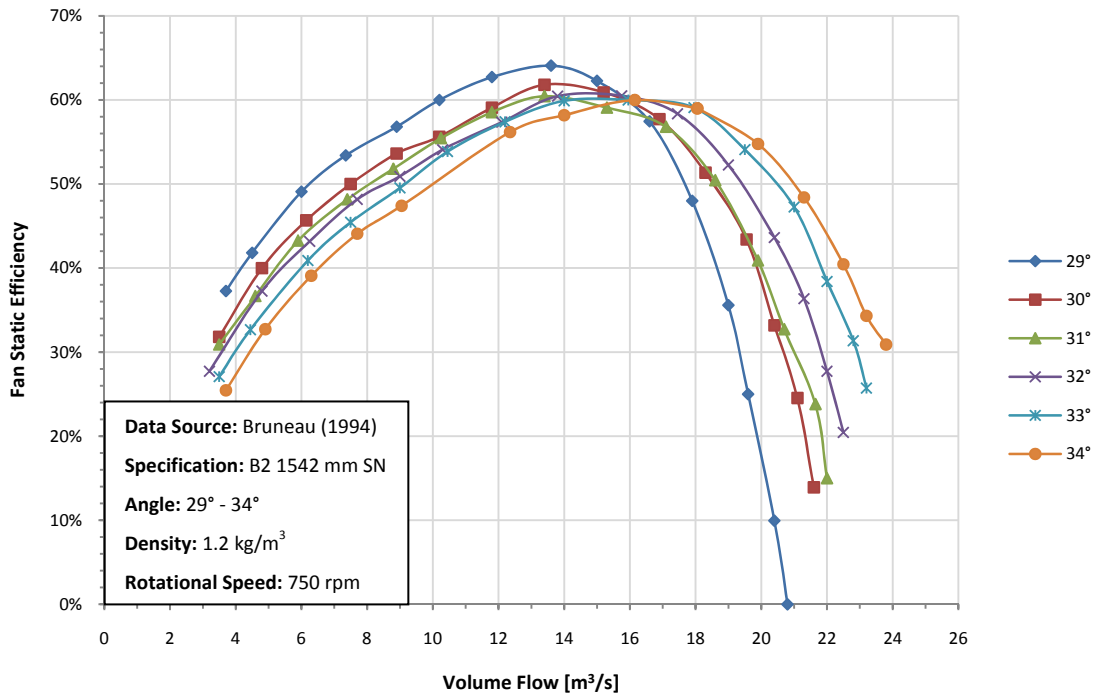


Figure B.11 B2 fan static efficiency curve

## APPENDIX C: SAMPLE CALCULATION FROM TEST DATA

A sample calculation of the first data point for measurements taken using Tunnel 3 with the B fan (Run C) fitted for determining the individual fan performance is shown below:

The calibration curve for pressure transducer 5 (in tunnel) is given by:

$$p_5 = 111.22425904 \cdot V_{p5} - 114.18282739 \quad (\text{C.1})$$

The calibration curve for pressure transducer 6 (in anemometer throat) is given by:

$$p_6 = 111.37582325 \cdot V_{p6} - 109.68318050 \quad (\text{C.2})$$

The calibration curve for anemometer 3 is given by:

$$\dot{V}_{anemo3} = 1.398298 \cdot V_{anemo3} + 0.005008 \quad (\text{C.3})$$

The calibration curve for torque transducer is given by:

$$T_{transducer} = 19.932565 \cdot V_{transducer} + 0.790974 \quad (\text{C.4})$$

The BS848 friction loss equation for one diameter of straight duct is given by:

$$\Lambda = 0.005 + 0.42(\text{Re}_{D4})^{-0.3} \quad (\text{C.5})$$

The BS848 conventional loss coefficient for the flow straightener is given by:

$$\zeta_S = 0.95(\text{Re}_{D4})^{-0.12} \quad (\text{C.6})$$

The total BS848 total loss coefficient:

$$\begin{aligned} (\zeta_{2-4})_4 &= 3\Lambda + 0.95 \\ &= 0.015 + 1.26(\text{Re}_{D4})^{-0.3} + 0.95(\text{Re}_{D4})^{-0.12} \end{aligned} \quad (\text{C.7})$$

The ideal gas density can be calculated by:

$$\rho = \frac{P_x}{RT} \quad (\text{C.8})$$

The data measured during testing:

$$V_{p5} = 1.82055 \text{ (zero: 0.96382 and 0.96526)}$$

$$V_{p6} = 4.50777 \text{ (zero: 3.09173 and 3.09178)}$$

$$V_{anemo3} = 1.3716$$

$$V_{transducer,load} = -0.18231 \text{ (zero: } -0.0392 \text{ and } -0.03959)$$

$$V_{transducer,no-load} = -0.05933 \text{ and } -0.06241 \text{ (zero: } -0.04137 \text{ and } -0.04089)$$

$$T_{atm} = 21.5 \text{ }^\circ\text{C}$$

$$p_{atm} = 100620 \text{ Pa}$$

Using Equation C.1, the relative pressure inside the tunnel at plane 4 can be determined as:

$$\begin{aligned} p_5 &= (111.22425904 \cdot 1.82055 - 114.18282739) - (111.22425904 \cdot \frac{0.96526 + 0.96382}{2} - 114.18282739) \\ &= 95.20907798 \text{ Pa} \end{aligned}$$

Using Equation C.2, the relative pressure in the throat at the anemometer can be determined as:

$$\begin{aligned} p_6 &= (111.37582325 \cdot 1.82055 - 109.68318050) - (111.37582325 \cdot \frac{3.09173 + 3.09178}{2} - 109.68318050) \\ &= 157.7098364 \text{ Pa} \end{aligned}$$

Using Equation C.3, the volume flow at the anemometer is given by:

$$\begin{aligned} \dot{V}_{anemo3} &= 1.398298 \cdot 1.3716 + 0.005008 \\ &= 1.917905537 \frac{m^3}{s} \end{aligned}$$

Using Equation C.8, the density of air at the anemometer can be determined by:

$$\begin{aligned} \rho_{anemo3} &= (p_{atm} - p_6) / 287.08 / (273.15 + 21.5) \\ &= 1.18766427 \frac{kg}{m^3} \end{aligned}$$

The mass flow through the tunnel can now be determined as:

$$\begin{aligned} \dot{m}_3 &= \dot{V}_{anemo3} \cdot \rho_{anemo3} \\ &= 2.277827879 \frac{kg}{s} \end{aligned}$$

Using Equation C.8, the density of air in the tunnel can be determined by:

$$\begin{aligned} \rho_{tunnel3} &= (p_{atm} + p_5) / 287.08 / (273.15 + 21.5) \\ &= 1.190654275 \frac{kg}{m^3} \end{aligned}$$

Through conservation of mass, the volume flow in the tunnel is found to be:

$$\begin{aligned} \dot{V}_{tunnel3} &= \dot{m}_3 / \rho_{tunnel3} \\ &= 1.913089238 \frac{m^3}{s} \end{aligned}$$

The Reynolds number of the flow at plane 4 is found to be:

$$\begin{aligned} Re_{D4} &= \frac{VD}{15} \cdot 10^6 = \frac{4\dot{V}_{tunnel3}}{15D\pi} \cdot 10^6 \quad (\text{kinematic viscosity approximation as per BS848}) \\ &= 257758.8222 \end{aligned}$$

The total pressure loss between plane 2 and plane 4 according to Equation C.7 was found as:

$$\begin{aligned} (\zeta_{2-4})_4 &= 0.015 + 1.26(257758.8222)^{-0.3} + 0.95(257758.8222)^{-0.12} \\ &= 5.784811324 \text{ Pa} \end{aligned}$$

The static pressure rise across the fan can now be found to be:

$$\begin{aligned} \Delta p_{static} &= p_5 + (\zeta_{2-4})_4 \\ &= 100.9938893 \text{ Pa} \end{aligned}$$

**Standardize the static pressure rise and volume flow to 750 rpm and  $1.2 \frac{\text{kg}}{\text{m}^3}$  air density :**

The new volume flow rate for 750 rpm is:

$$\begin{aligned} \dot{V}_{3,750/1.2} &= \dot{V}_{tunnel/3} \cdot \frac{750}{1301} \quad (\text{the fan diameter remains unchanged}) \\ &= 1.102856978 \frac{\text{m}^3}{\text{s}} \end{aligned}$$

From Equation C.8, the density of the atmosphere during the testing can be found to be:

$$\begin{aligned} \rho_{atm} &= \frac{p_{atm}}{R(T_{atm} + 273.15)} \\ &= 1.189528714 \frac{\text{kg}}{\text{m}^3} \end{aligned}$$

Finally, the fan static pressure rise for the new conditions is found to be:

$$\begin{aligned} \Delta p_{static,750/1.2} &= \Delta p_{static} / \rho_{atm} \cdot 1.2 \cdot (750 / 1301)^2 \\ &= 33.85862731 \text{ Pa} \end{aligned}$$

#### **Fan Power Calculation :**

The torque as measured during testing can be calculated from Equation C.4 as:

$$\begin{aligned} T_{load} &= (19.932565 \cdot -0.18231 + 0.790974) - (19.932565 \cdot \frac{-0.0392 - 0.03959}{2} + 0.790974) \\ &= -2.84866253 \text{ Nm} \end{aligned}$$

The no-load torque, measured separately from testing, can also be found using Equation C.4:

$$\begin{aligned} T_{no-load} &= (19.932565 \cdot \frac{-0.05933 - 0.06241}{2} + 0.790974) - (19.932565 \cdot \frac{-0.04089 - 0.04137}{2} + 0.790974) \\ &= -0.39346883 \text{ Nm} \end{aligned}$$

The shaft torque as a result of the work done by the fan can now be found as:

$$\begin{aligned} T_{shaft} &= T_{load} - T_{no-load} \\ &= -2.45519369 \text{ Nm (negative torque merely indicates direction)} \end{aligned}$$

The power required by the fan can be found by  $\omega T$  to be:

$$\begin{aligned} P_{shaft} &= T_{shaft} \cdot \frac{1301 \cdot 2\pi}{60} \\ &= 334.4965744 \text{ W} \end{aligned}$$

**Standardize fan power to 750 rpm and  $1.2 \frac{\text{kg}}{\text{m}^3}$  air density :**

The power required by the fan for the new conditions can be found as:

$$\begin{aligned} P_{shaft,750/1.2} &= P_{shaft} \cdot \left(\frac{750}{1301}\right)^3 \text{ (diameter remains unchanged)} \\ &= 64.08310923 \text{ W} \end{aligned}$$

The fan static efficiency is a measure of work done to power required and is given by:

$$\begin{aligned} \eta &= \frac{\Delta p_{static,750/1.2} \cdot \dot{V}_{3,750/1.2}}{P_{shaft,750/1.2}} \\ &= 0.582149088 = 58.2149088 \% \end{aligned}$$